HETEROGENEOUS NUCLEATION OF IRON OXIDES (γ-Fe_2O_3) IN COLLOIDAL SYSTEMS

Darinka Primc

Doctoral Dissertation
Jožef Stefan International Postgraduate School
Ljubljana, Slovenia, April, 2013

Evaluation Board:

Prof. Dr. Darko Makovec, Chairman, Jožef Stefan Institute, Ljubljana

Prof. Dr. Mihael Drofenik, Member, Faculty for Chemistry and Chemical technology University of Maribor, Maribor

Asst. Prof. dr. Goran Dražić, Member, Jožef Stefan Institute, Ljubljana

MEDNARODNA PODIPLOMSKA ŠOLA JOŽEFA STEFANA
JOŽEF STEFAN INTERNATIONAL POSTGRADUATE SCHOOL

Darinka Primc

HETEROGENEOUS NUCLEATION OF IRON OXIDES (γ-Fe_2O_3) IN COLLOIDAL SYSTEMS

Doctoral Dissertation

HETEROGENA NUKLEACIJA ŽELEZOVEGA OKSIDA (γ-Fe_2O_3) V KOLOIDNIH SISTEMIH

Doktorska disertacija

Supervisor: Asst. prof. dr. Darja Lisjak

Ljubljana, Slovenia, April 2013

Index

Abstract ..... Error! Bookmark not defined. **X**

Povzetek ..... Error! Bookmark not defined. **I**

Abbreviations ..... Error! Bookmark not defined.

1 Introduction **17**
1.1 Magnetism 17
1.1.1 Magnetic ordering in particles of ferro- and ferrimagnetic materials 19
1.2 Crystal structure of ferrites 25
1.2.1 Hexagonal structure 25
1.2.2 Cubic ferrite structure 27
1.3 Synthesis of spinel nanoparticles 29
1.3.1 Nucleation 30
1.3.1.1 Homogeneous nucleation 30
1.3.1.2 Heterogeneous nucleation 31
1.3.1.3 Growth 32
1.4 Colloidal suspensions 32
1.4.1 Interaction between colloidal particles 33
1.4.2 Magnetic interactions 36

2 Aims and Hypothesis **37**

3 Materials and Methods **39**
3.1 Materials 39
3.2 Synthesis Methods 39
3.2.1 Synthesis of the spinel with homogeneous nucleation 39
3.2.2 Synthesis of the spinel with heterogeneous nucleation 40
3.2.2.1 Synthesis of core nanoparticles 40
3.2.2.2 Synthesis of nanocomposite particles 41
3.3 Characterization techniques 41
3.3.1 XRD powder diffraction 41
3.3.2 Electro-kinetic measurements 42
3.3.3 Transmission electron microscopy 42
3.3.4 Vibrating sample magnetometer 42
3.3.5 Thermo-gravimetric method 42
3.3.6 Infrared spectroscopy 43
3.3.7 UV-Vis Spectroscopy 43

4 Results **45**
4.1 Synthesis of the spinel with homogeneous nucleation 46

4.1.1 Controlled release of iron ions from Fe^{3+}-urea complex 46
4.1.2 Controlled release of hydroxyl ions 49
4.2 Core nanoparticles 56
4.2.1 Silica (SiO_2) core nanoparticles 56
4.2.2 Ba hexaferrite (BaM) core nanoparticles 57
4.3 Synthesis of the spinel with heterogeneous nucleation 60
4.3.1 S@SiO_2 nanocomposite particles 61
4.3.2 Reaction mechanism 62
4.3.3 S@BaM nanocomposites particles 72
4.3.3.1 Effect of core nanoparticles structure 72
4.3.3.2 Effect of the core nanoparticles size and morphology 76
4.4 Magnetic properties 83

5 Discussion 89

6 Conclusions 103

7 Acknowledgements 107

8 References 109

Original scientific article 125
Published scientific conference contributions 125
Published scientific conference contribution abstract 125
Work report 126

Abstract

Presented work is a study of magnetic iron oxide (referred to as spinel) coating synthesis. The coatings were synthesized on the surfaces of selected core nanoparticles with heterogeneous nucleation during the co-precipitation of the Fe^{3+}/Fe^{2+} ions. The work is divided into three parts. The first part comprise the synthesis of spinel nanoparticles with coprecipitation of Fe^{2+}/Fe^{3+} ions under condition involving low supersaturation of nucleating species. The second part was aimed to coat spinel on the surfaces of different core nanoparticles involving heterogeneous nucleation, thus the spinel synthesis was done in the colloidal suspensions of the core nanoparticles. The third part of the thesis involves the study of the effect of the core nanoparticles size, size distribution, morphology, and crystal structure on the synthesis of spinel coatings. Here, the magnetic properties of synthesized nanocomposite particles were also evaluated.

First, the synthesis of the spinel nanoparticles under condition of low supersaturation was studied since such conditions favours heterogeneous nucleation when spinel is synthesized in the presence of core nanoparticles. The slow supersaturation was achieved with slow and homogeneous release of the reactants; the Fe^{3+} ions and hydroxyl ions. The highly reactive Fe^{3+} ions were immobilized into an urea-complex while hydroxyl ions needed for homogeneous precipitation of the Fe^{2+} ions were achieved with the addition of solid $Mg(OH)_2$. The spinel synthesis proceeded at temperature of 60 °C where thermal decomposition of Fe^{3+}- urea complex resulted in gradual release of Fe^{3+} ions that formed γ-FeOOH with thermal hydrolysis. The addition of $Mg(OH)_2$ resulted in precipitation of the Fe^{2+} ions that after reacting with γ-FeOOH formed spinel. Here, the extend of thermal hydrolysis needed to be closely controlled since the γ-FeOOH phase required for final spinel formation formed only in a narrow time interval.

Second, the method described above was used to coat the spinel onto the surfaces of amorphous silica core nanoparticles. The analysis revealed that the spinel phase formed on the surfaces of the core nanoparticles with heterogeneous nucleation. As the result of the thermal hydrolysis of the Fe^{3+} ions, γ-FeOOH phase in the form of 3 nm nanoparticles nucleated as the initial phase. After the $Mg(OH)_2$ additions the precipitated Fe^{2+} ions reacted with the γ-FeOOH phase on the silica surfaces resulting in the complete transformation into spinel. The formed spinel coating consisted of discrete, randomly-oriented spinel nanoparticles, approximately 7 nm in size.

To evaluate the effect of core nanoparticle properties on the spinel coating synthesis, the synthesis was done also in the suspension of crystalline platelet Ba-hexaferrite nanoparticles of different size and morphology. Here, the uniform and homogeneous spinel layer was obtained on the surface of hexaferrite basal planes. Due to the structural similarities between hexaferrite (HF) and spinel (S), the spinel layer grew epitaxially forming coherent interface with $(0001)_{HF} \parallel (111)_S$. The spinel layer formed only on the basal planes, while the formation of spinel on the side faces of the hexaferrite nanoparticles was never observed due to lattice mismatch between the two phases along $[0001]_{HF}$.

The magnetic measurement of nanocomposite particles where hard-magnetic core nanoparticles were coated with soft-magnetic spinel shell revealed the increase in remanence (28.2 Am^2/kg) and in saturation magnetization (56 Am^2/kg) due to the

presence of the soft-magnetic spinel phase while coercivity only slightly decreed since the easy-axis magnetization of both phases is oriented in the same direction. The comparison of the hysteresis for magnetically oriented assemblies of the nanocomposite particles and the untreated Ba-hexaferrite core nanoparticles revealed the significant increase in the energy product for over 50 %.

Povzetek

V svojem delu sem se ukvarjala s sintezo magnetnih plasti magnetnega železovega oksida (kasneje v tekstu spinel) na površinah izbranih jedrnih nanodelcev. Delo je razdeljeno na tri dele. Prvi del zajema študijo sinteze spinelnih nanodelcev z metodo soobarjanja železovih Fe^{2+}/Fe^{3+} ionov z izbranimi pogoji majhnega prenasičenja. Drugi del zajema sintezo spinelnih plasti na površini koloidnih jedrnih delcev. Sinteza spinelnih plasti je potekala v suspenziji jedrnih delcev in z reakcijskimi pogoji, ki favorizirajo heterogeno nukleacijo produkta. V tretjem delu sem preučevala vpliv jedrnih koloidnih nanodelcev na sam potek sinteze spinelnih plasti. Tako sem sintezo spinelnih plasti izvajala v koloidnih suspenzijah jedrnih nanodelcev različnih velikosti, oblike in kristalne strukture. Nanokompozitnim produktom, kjer sem kot jedrne delce uporabila Ba heksaferitne nanodelce sem ovrednotila tudi magnetne lastnosti.

V prvem delu sem preučevala sintezo spinela pod pogoji majhnega prenasičenja, saj bi se pod temi pogoji nastajajoče faze nukleirale heterogeno na površini jedrnih koloidnih delcev, če bi sinteza potekala v koloidni suspenziji. Majhno prenasičenja je bilo doseženo z počasnim in homogenim sprašanjem reaktantov; Fe^{3+} ionov in hidroksilnih ionov. Reaktivnost Fe^{3+} ionov sem zmanjšala s tvorbo kompleksa z ureo, medtem ko sem homogeno obarjanje Fe^{2+} ionov dosegla dodatkom $Mg(OH)_2$. Sinteza spinela je potekala pri temperaturi 60 °C. Pri teh pogojih pride do počasnega razpada Fe^{3+}-urea kompleksa, kar omogoči počasno sproščanje Fe^{3+} ionov, ki s termično hidrolizo tvorijo γ-FeOOH fazo. Dodatek $Mg(OH)_2$ povzroči obarjanje Fe^{2+} ionov, ki po reakciji z γ-FeOOH fazo tvorijo spinel. Proces tvorbe γ-FeOOH faze, ki nastane s procesom termične hidrolize je potrebno natančno kontrolirati, saj se γ-FeOOH faza tvori le v ozkem časovnem intervalu.

V nadaljevanju sem z namenom doseči sintezo spinelnih plasti s heterogeno nukleacijo zgoraj opisano sintezo spinela preizkusila v stabilnih koloidnih suspenzijah nanodelcev amorfnega silicijevega oksida. Analize pokažejo, da se pri pogojih majhnega prenasičenja spinelna faza tvori na površini nanodelcev silicijevega oksida s heterogeno nukleacijo. S termično hidrolizo Fe^{3+} ioni tvorijo γ-FeOOH fazo, ki se v obliki 3 nm delcev nukleira na površini jedrnih nanodelcev. Po dodatku $Mg(OH)_2$ pride do obarjanja Fe^{2+} ionov, ki ob reakciji z nastalo γ-FeOOH fazo tvorijo spinel. Spinelne plasti, ki se tvorijo na površini silicijevega oksida so v obliki diskretnih, naključno orientiranih 7 nm nanodelcev.

Da bi preučila vpliv lastnosti jedrnih nanodelcev na potek tvorbe spinelnih plasti sem sintezo spinela izvedla v suspenzijah različno velikih kristaliničnih nanodelcev Ba heksaferita. Tu je prišlo do tvorbe homogenih plasti spinela na bazalnih ravninah heksaferita. Zaradi delne sorodnosti v strukturah tvori spinelna (S) plast koherentno mejo $(0001)_{HF} \| (111)_S$ in raste epitaksialno na površini heksaferita (HF). Do tvorbe spinelnih plasti pride samo na bazalnih ravninah heksaferita, medtem ko na stranskih površinah, tvorba spinela ni opažena zaradi neujemanja v strukturah obeh faz.

Magnetne meritve nanokompozitnih delcev, kjer sem trdo-magnetno heksaferitno jedro prevlekla z mehko-magnetno spinelno fazo pokažejo znatno povečanje nasičene magnetizacije (56 Am^2/kg) in remanence (28.2 Am^2/kg) na račun prisotne mehko-magnetne spinelne faze. Ker sta osi magnetne lahke-orientacije obeh faz usmerjeni v isto smer pride le do majhnega zmanjšanja polja koercitivnosti. Primerjava magnetnih histerez magnetno usmerjenih nanokompotiznih delcev in samih jedrnih delcev pokaže znatno

povečanje energijskega produkta za preko 50%.

Abbreviations

ϕ = angle between spin vectors
J = exchange integral
$S_{1,2}$ = spin vectors
A = exchange constant
K = anisotropy constant
μ_0 = vacuum permeability
M_s = saturation magnetization
Θ = angle formed between magnetization and anisotropy axis
V = sample volume
K = anisotropy constant
τ = relaxation time
τ_0 = pre-exponential factor (10^{-10} – 10^{-12} s)
k_u = effective anisotropy constant
C_L = precursor concentration
C_S = solubility of the solid phase
Ω = molecular volume
γ = surface tension
B = kinetic constant,
γ_{cf} = specific interfacial free energy between
$\Delta\rho$ = density differences between particles and dispersing medium
V = particles volume
A = effective Hamaker constant
R = centre-to-centre separation distance ($R = D+2a$)
h = surface-surface separation between the particles,
a = particles radius
κ = Debye-Hückel reciprocal length
n_∞ = bulk density of ions
R = distance between two particles centres
$m0$ = magnetic moment
$\mu0$ = permeability of vacuum.

1 Introduction

Nanotechnology is a broad and interdisciplinary research field that has been growing exponentially in past decades and it shows a great potential for various applications. The vast interest in nanostructured materials mainly arises from the fact that these structures possess new distinct physical and magnetic properties that differ from the one of bulk counterparts. These unique properties mainly originate from their peculiarities originating from their small size, high surface to volume ratio and large proportion of surface atoms compared to bulk materials [1].

Particularly nanoparticles based on magnetic iron oxides have been studied to be applied in a certain application in technology and recently also in modern medical applications. However, to meet the high standards required for their applications seldom single phase nanoparticles alone cannot display the desired properties. A promising approach is to synthesize multiphase core-shell nanostructures where the synergy of magnetically different phases would give rise to their enhanced magnetic properties.

Thus introductory chapters are dedicated to provide the reader with certain basic of the origin of the magnetism in materials together with the detailed explanations of their crystal structure. The synthesis techniques, reported in the literature together with the benefits and restrictions related to their use are also addressed.

1.1 Magnetism

The magnetic response of the material strongly depends on the structure of constituting atoms and their arrangement. Magnetism in magnetic atoms originates from the spin moment of the electron and orbital angular moment. The net magnetic moment of atom is a vector sum of all electronic moments and thus relies on their orientation. For the atoms of pair-electron occupied orbital shell the complete cancellation of magnetic moments is present. On the contrary, for atoms or ions with unpaired-valent electrons the resulted net magnetic moment defines such atoms as magnetic. The net moment for magnetic atom depends on the number of the unpaired electron in d and f orbitals and from gyromagnetic ratio (the ratio between spin and angular moment) [1,2].

When a material is placed in the external magnetic field the individual atomic moments in the material contribute to its overall response. The material is classified as diamagnetic when consisting of atoms with paired valent electrons. Such materials display week net magnetization acting in reverse to the external fields (Figure 1a). The behavior is described with low negative susceptibility χ. Constituting atoms of paramagnetic materials have unpaired valent electrons and display week magnetic response in the direction of the applied field (Figure 1b).

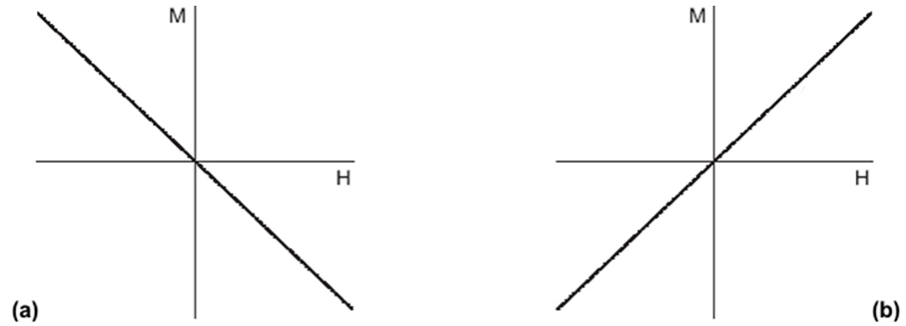

Figure 1: *The response of diamagnetic (a) and paramagnetic (b) materials when exposed to the external magnetic field [3].*

Special classes of materials are ferromagnetic materials. Here the magnetic moments of atoms exhibit certain long-range order due to the mutual interactions. Magnetic moments of neighboring atoms are either parallel or antiparallel aligned (Figure 2). The parallel alignment of the magnetic moments leads to the strong response (high positive susceptibility and permeability), when material is exposed to the field.

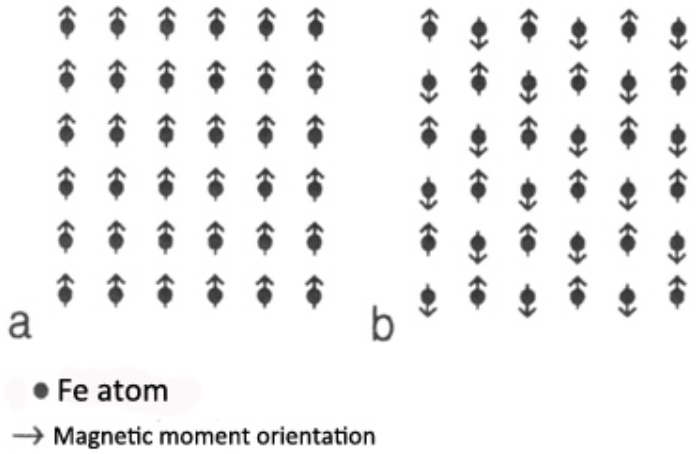

Figure 2: *Schematic illustration of the ferromagnetic (a) and antiferromagnetic ordering (b)* [2].

The material is magnetically subdivided into small regions, also known as magnetic domains. Here, the orientation of magnetic moments is determined by the direction of the spin and orbit on which it moves. The interaction that occurs between electron spins is called the exchange interaction. The exchange interactions for example between spins in adjacent atom can be described in term of the exchange energy:

$$E_{ex} = -2JS_1S_2 \cos\phi \tag{1}$$

ϕ angle between spin vectors
$S_{1,2}$ spin vectors
J exchange integral.

For positive J, the exchange energy will be lower for parallel oriented spins and highest for anti-parallel ordering. On contrary, the exchange energy will be lower for antiparallel ordering when $J > 0$. Ferromagnetism is present when alignment for spin moments of adjacent atom is parallel. On contrary, the antiparallel alignment is found in antiferromagnetic materials [4].

Special class of magnetic materials is oxide ferrimagnetic materials. Here, like in antiferromagnetic substances the material consists of at least two sublattices where the negative exchange energy of the spins J favours the antiparallel spin alignment. In these substances the magnetic metal ions are separated with negative charged anions. Thus instead of direct exchange-coupling between metal ions, present in the ferromagnetic materials, the metal ions are coupled through the oxygen ions with so called super exchange interactions. The magnetic moments are antiparallel aligned in two different sublattices, whereas their alignment is parallel within one sublattice (Figure 3). The magnetic moment of one sublattice can prevail in respect to another, that result in the net magnetic moment [1].

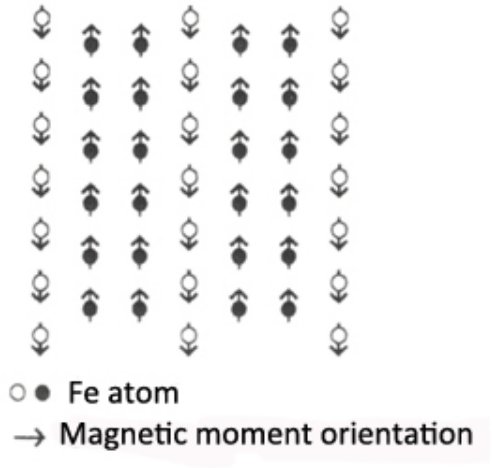

Figure 3: *Schemtic illustration of the ferrimagnetic spin orientation [1].*

1.1.1 Magnetic ordering in particles of ferro- and ferrimagnetic materials

The ferro- and ferrimagnetic materials display hysteresis when they are exposed to the external magnetic field, which can be explained in terms of their magnetic domain structure. As I mentioned before the magnetic moments in the materials are arranged into the magnetic domains. Domains are characterized with the parallel alignment of the magnetic moment and are separated by the domain walls. Here the differences in the direction of the magnetic moments between individual domains result in the spontaneous magnetization of the ferro- and ferrimagnetic materials.

By applying small external magnetic field, the domains walls can be moved across the materials. Increased field results in the alignment of the magnetic moments within

domain walls in the direction of the field. At a fully saturated state (*Ms*) all the magnetic moments are parallel aligned in the direction of the field within one domain. When the external magnetic field drops to zero, the irreversibility of the domain wall motion occurs, resulting in the retained partial alignment of the magnetic moments. Due to the partial magnetic relaxation the remanent magnetization (*Mr*, Figure 4) measured at zero field is smaller than the saturated magnetization. In reversed external filed –H the magnetization can be reduced to zero. The filed required to obtain zero magnetization is referred as coercive field (*Hc*, Figure 4). The shape of the hysteresis loop in ferrimagnetic materials significantly depends on the exchange interaction and the anisotropy energy. The interplay between two parameters defines the domain wall thickness and thus the magnetic behaviour [1].

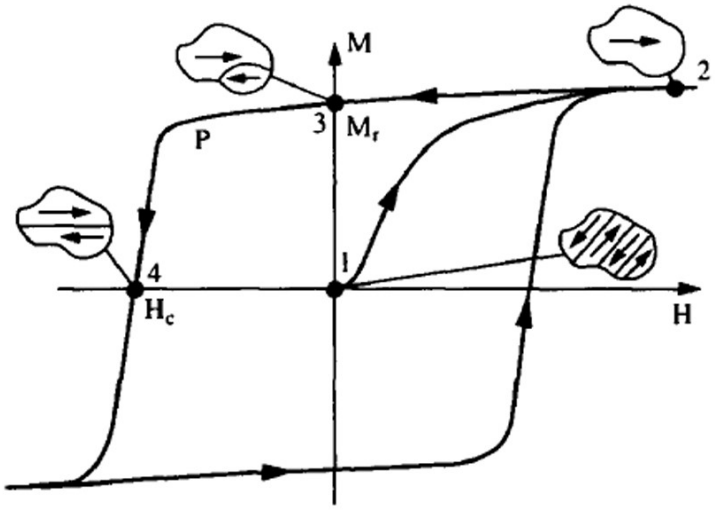

Figure 4: *Schematic illustration of the hysteresis loop for the magnetic materials with multi-domain structure [5].*

According to the shape of the hysteresis loops the magnetic materials are classified as hard and soft magnetic materials. Here the easy direction or the direction of the spontaneous magnetization is typically aligned along preferred crystallographic direction as a result of the magneto-crystalline anisotropy. The materials are classified as soft magnetic when relatively low external fields are required for their saturation. Typically such materials exhibit low coercive field. On the contrary, hard magnetic materials exhibit large coercivity, and high magnetic field needs to be applied to achieve their saturation (Figure 5). The difference in the coercivity is related to the magnitude of the magneto-crystalline anisotropy.

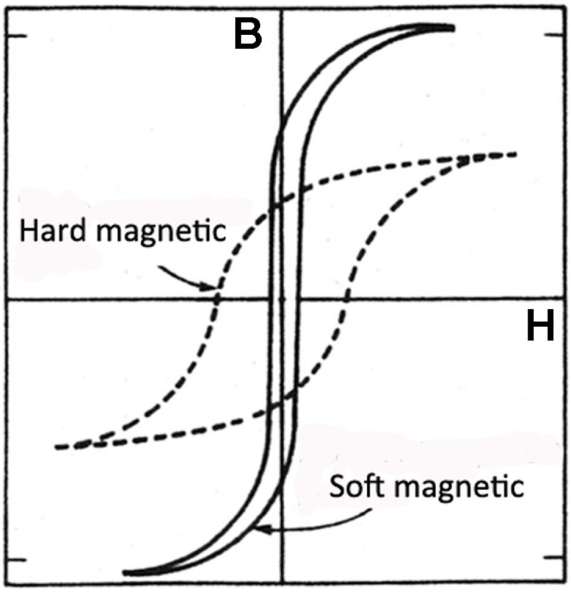

Figure 5: *Schematic illustration of the hysteresis loop typical of hard and soft magnetic materials [3].*

Ferrimagentic materials based on iron oxide are according to crystal structure classified in two groups. First are cubic ferrites with general formula $MO{\cdot}Fe_2O_3$, where M represents divalent metal ions like Mn, Ni, Co or Mg. All cubic spinels are soft magnetic with magneto-crystalline anisotropy in the range of ~ 10^3 J/m^3, with the exception of Co ferrite which exhibit hard magnetic properties. Another type of ferrimagnetic materials are so called hexaferrites that crystallize in a hexagonal close packed system. The most important in this group are Ba and Sr hexaferrites ($MFe_{12}O_{19}$, M= Ba, Sr). Hexaferrite are hard-magnetic materials with large magneto-crystalline anisotropy in order of ~ 10^6 J/m^3 [4].

My work comprises the synthesis of complex iron oxide nano-architectures based on two types of ferrimagnetic materials: hexagonal Ba hexaferrite with magnetoplumbite structure ($BaFe_{12}O_{19}$) and cubic spinel ferrites: magnetite (Fe_3O_4) and maghemite (γ-Fe_2O_3). Such advanced nano-architecture are interesting due to their magnetic properties, in large extend originating from the differences in their structure and extrinsic properties related to the particles size and morphology. However, before the crystal structures of hexaferrite and spinel ferrite are examined, let us first revise the scale reduction influence on the magnetic properties of ferrite materials.

As the size of particles of ferrimagnetic materials is reduced, the particles can no longer gain a favorable energy configuration by breaking down into the domains. For a given size of particles system then adopts single-domain configuration, when no external field is applied (Figure 6). The particles can also be considered as uniformly magnetized through the volume and therefore represented as one super-spin. The particles exhibit single-domain state when the energy required for the formation of domain wall excides the reduction of the electrostatic energy. Despite several disagreements related to the definition of critical size of multi-domain-single-domain transition in approximation the critical radius can be expressed with the following equation:

$$r_c \approx 9\sqrt{\frac{AK}{\mu_0 M_S^2}} \tag{2}$$

A exchange constant
K anisotropy constant
μ_0 vacuum permeability
M_S saturation magnetization

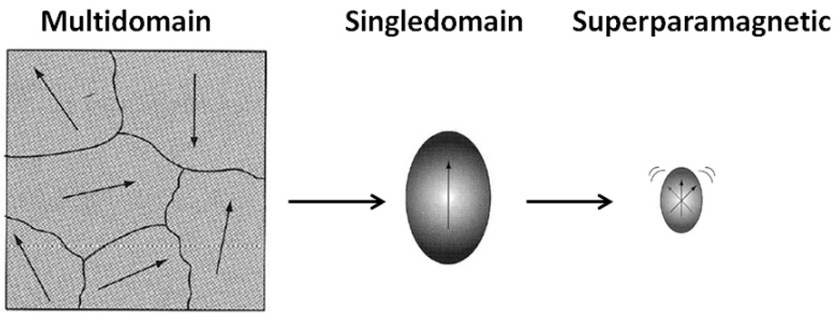

Figure 6: *Magnetic behavior derived from the scale reduction of the magnetic nanoparticles [6].*

In single domain particles, the energy tends to keep the magnetization in the preferred crystallographic direction. This is easy direction or easy axis. The easy axis dictates the direction of spontaneous magnetization in the absence of the magnetic field and it is mainly determined by intrinsic materials properties. For spinel maghemite and magnetite it is aligned along the [111] direction of cubic structure, i.e. along body diagonal. For the hexagonal structure the easy axis is in the [0001] direction, i.e. along c-dimension of hexaferrite unit cell [4].
Magnetization direction (*Ms*) is defined by interplay between applied field (*H*) and anisotropy axis in a way forming angle φ with respect to anisotropy axis (Figure 7). The following relation describes the equation [1]:

$$E(\theta) = KV\sin^2\theta - HM_s(\cos\theta\cos\varphi + \sin\theta\sin\varphi\cos\psi) \tag{3}$$

Θ angle formed between magnetization and anisotropy axis
V sample volume
K anisotropy constant

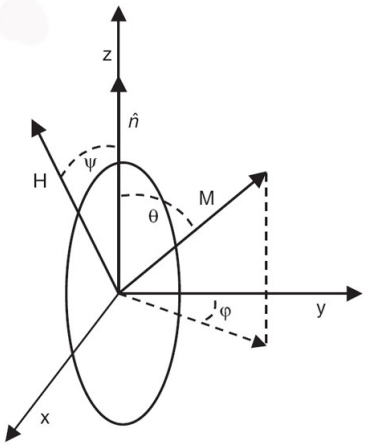

Figure 7: *Axis system defined for uniaxial nanoparticles [1].*

Magnetization reversal in single-domain particle proceeds with coherent or incoherent rotation. The first theory was developed by Stoner-Wohlfarth by assumption that the particles does not interact between each other. The magnetization reversal can proceed also through the incoherent spin motion. Here the magnetization reversal proceeds through the energy barrier created by magnetic anisotropy [1].

With further reduction of the particle size the superparamagnetism occurs. This phenomenon is observed when ferrimagnetic particles size is reduced below level at which thermal energy prevail the anisotropy energy (Figure 6). Anisotropy energy is defined as $K \cdot V$, where V represents the particles vthe olume and K stands for the effective anisotropy constant and. The $K \cdot V$ product presents the energy barrier ΔE that is comparable to the thermal energy $k_B \cdot T$ when the particles size decreased below critical value.
When in superparamagnetic state the magnetic moment of the particle as a whole relaxes in response to the thermal energy, while individual atomic moments maintain their ordered state relatively to each other.
Such relaxation of magnetic moment is referred as the Nell relaxation. The characteristic time of Nell relaxation depends on particles size and increases with increasing volume [6].

$$\tau = \tau_0 \exp\frac{\Delta E}{k_b T} = \tau_0 \frac{k_u V}{k_b T} \tag{4}$$

τ relaxation time
τ_0 pre-exponential factor (10^{-10} – 10^{-12} s)
k_u effective anisotropy constant

This results in sigmoid but not hysteresis *MH* curve shown in Figure 8. The superparamagnetism is a phenomenon where ferrimagnetic materials behave as diamagnetic below the Currie temperature. As in paramagnetic materials the superparamagnetic materials also display a large increase in the magnetization when exposed to the magnetic field, while it drops to zero when the field is switch off. However, the magnetic moment in superparamagnetic materials is several orders higher. The magnetization curve of superparamagnetic materials is defined with the Langevin

function [1, 5]:

$$M = M_S L(x),\ \ L(x) = \coth(x) - \frac{1}{x},\ \ \ x = \frac{M_S V H}{kT}$$

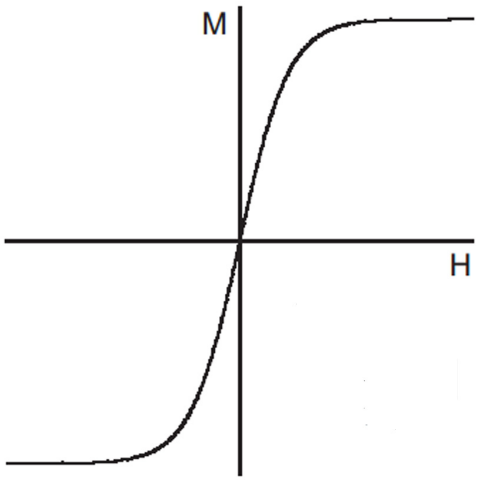

Figure 8: *The MH curve of superparamagnetic nanoparticles*.

The superparamagnetic particles show zero coercivity and remanence. Figure 9 shows the coercivity in dependence of the particles size. In general the decrease in the particles size first results in the increase of the coercivity that reaches its maximum when the particles are in single domain state. With decreasing of the particles size the energy of the domain wall formation excides the reduction of magneto-static energy thus at the particles size of D_s, single domain state is favorable. When particles size is equal or smaller than D_s, the magnetization reversal no longer proceeds with the domain wall motion. Magnetization reversal that instead proceeds with simultaneous rotation of all the spins in the particles requires large external field. With further decrease in the size the energy barrier required for spin rotation decreases due to the thermal effect. Consequently the magnetic field required to obtain zero magnetization decrease. The coercivity is zero when particles size is below critical value D_P when they exhibit superparamagnetic state. Spinel iron oxides become superparamagnetic at the size below 20 nm, while Ba hexaferrite due to its large magneto-crystalline anisotropy and typically anisotropic particles shape exhibit superparamagnetic behavior below 10 nm [1].

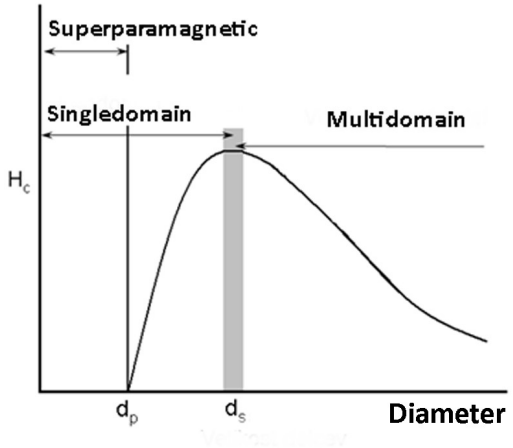

Figure 9: *The coercivity in dependence of the particles size [1].*

1.2 Crystal structure of ferrites

1.2.1 Hexagonal structure

Ba hexaferrite with chemical formula $BaFe_{12}O_{19}$ is structurally similar to the structure of the mineral magnetoplumbite. The hexagonal unit cell consists of 10 oxygen layers with cell parameter a = 0.555 nm and c = 2.32 nm. Here Ba and O ions (both nonmagnetic) are arranged in hexagonal close packed system while Fe ions are positioned on the interstitial sites. The hexagonal unit cell is subdivided into alternating hexagonal R block connected to the spinel S block (Figure 10). The hexagonal R blocks $(BaFe^{3+}{}_6O^{2-}{}_{11})^{2-}$) are composed of three layer of oxygen where the middle also contains the Ba ion. The spinel S block $(Fe^{3+}{}_6O^{2-}{}_8)^{2+}$) is built up of a two oxygen layers and by oriented in [111] direction of cubic spinel structure exhibits structural match with hexagonal structure in [0001] direction. In S block the oxygen ions form a close packed system while two Fe ions are distributed over tetrahedral and four over octahedral sites [4, 7].

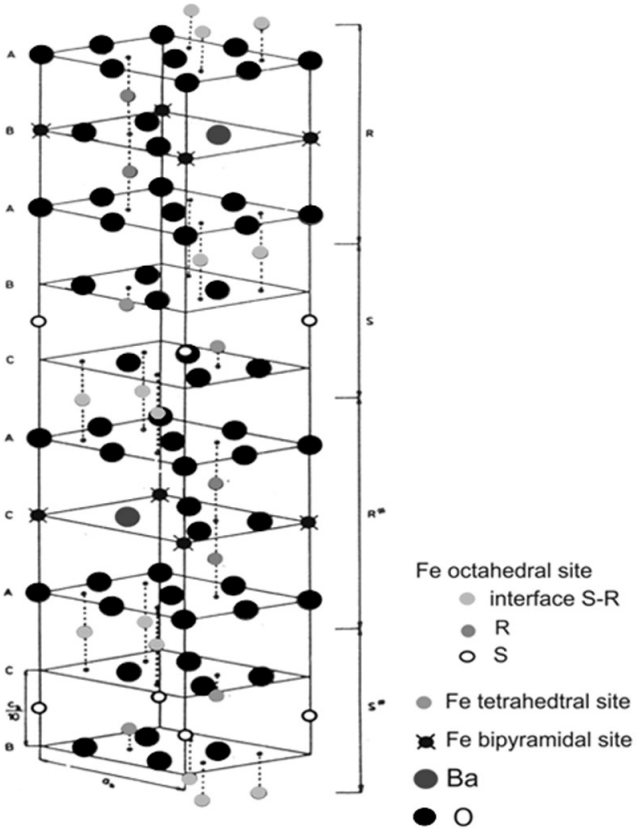

Figure 10: *Crystal structure of Ba hexaferrite*

The R block consists of three layers where, where the outer one consists of purely oxygen and the middle one contain the Ba ion. Here the cubic sequence of layer is no longer possible due to the effort of minimizing the Coulomb energy, which results in the redistribution Fe ions. Consequently, the structure becomes hexagonal, where Ba and O ions form hexagonal close packed system, and Fe ions occupy three types of sites (Figure 10). In first, (octahedral sites) Fe ions occupy octahedra shared by common faces (octahedral sites). Here, mutual distances are lower than on the octahedral sites in spinel block which results in a higher Coulomb contribution of Fe. Second type of sites are five-fold coordinates sites where, formed by the face shared tetrahedral. The Fe ions in these sites either oscillate or they are distributed between two sites. Third type of sites occurs at the interface between the adjacent R-S blocks. The energy of these sites however differs from similar sites in S block due to the difference of nearest neighbours [4, 7].

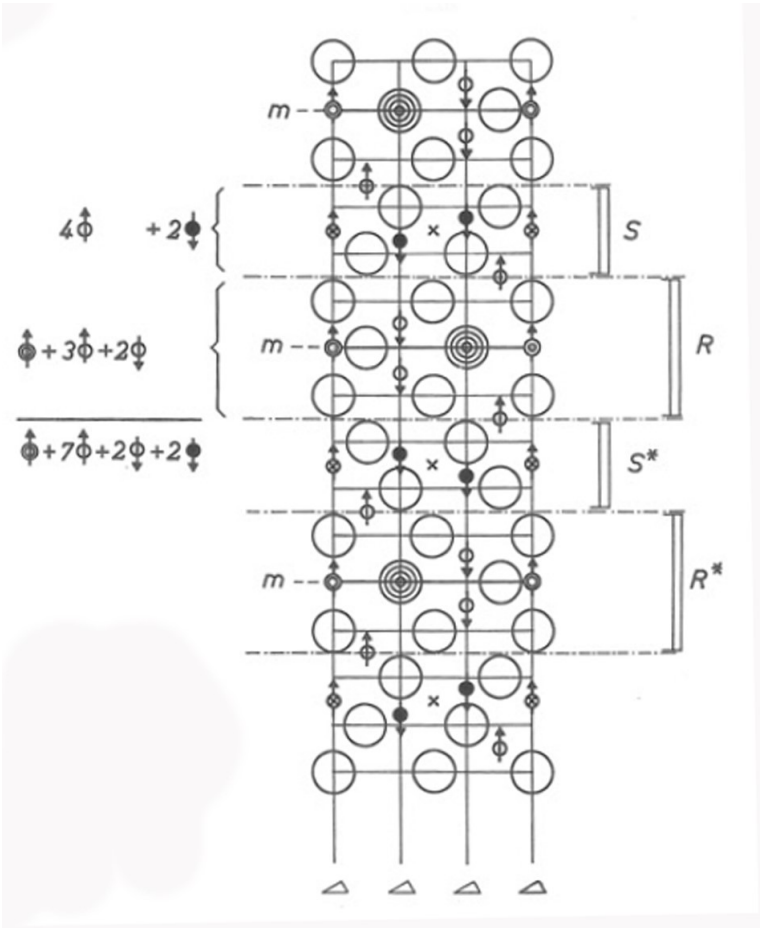

Figure 11: *Cross section view of Ba hexaferrite structure [7].*

The Ba hexaferrite, due to the presence of large Ba ions, exhibits the perturbation in the lattice due to the size differences, which results in hexaferrite magneto-crystalline anisotropy. The Ba hexaferrite has a preferred axis of the magnetization along the c-axis. Thus the magnetic properties are different when measured in the direction of the alignment with field parallel with c-axis or (material saturates at lower applied field and the *Hc* is larger) compared to if a field is oriented perpendicular [8].
The magnetism in the Ba hexaferrite originates from Fe ions distributed over different sites as seen in Figure 11. The Ba hexaferrite structure is subdivided into the magnetic sublattices. Due to the numerical differences of the up- and down- oriented magnetic moments, Ba hexaferrite exhibit net magnetic moment. The net value for Ba hexaferrite yields 20 μ_B, which attributes to its high saturation magnetization of 72 $Am^2\ kg^{-1}$ and high Currie temperature [8].

1.2.2 Cubic ferrite structure

Cubic ferrites have general formula of $MOFe_2O_3$, where M stand for two-valent cations: Mn, Fe, Co, Ni, Mg [4]. They are referred to as *ferrospinels* since their structure is closely related to the mineral spinel $MgAl_2O_4$. In my work I have studied the synthesis of cubic spinel with formula $((Fe^{3+})[Fe^{3+}_{5/3}\ V_{1/3}\ ]O_4$, where round and square brackets represent tetrahedral and octahedral sites, respectively, and V vacancies. The spinel unit cell with cubic symmetry contains 8 molecules of MFe_2O_4 (Figure 12). Larger oxygen

atoms form a face centred cubic cell, where smaller Fe atoms occupy the interstitial sites. In this cubic close-paced structure, two types of the interstitial sites are present: tetrahedral A sites (surrounded by 4 oxygen atoms) and octahedral or B sites (surrounded by 6 oxygen atoms). The interstitial sites in cubic spinel are only partially occupied. Here only one-eighth of A sites and one-half of B sites are occupied by metal cations. According to the occupancy of the interstitial sites the cubic ferrites are structurally distinguished as normal or the inverse spinels. In normal spinel M^{2+} ions occupy A sites where Fe^{3+} ions occupy B sites. In the inverse spinel all divalent ions are on B sites while trivalent ions are equally divided into B and A sites.

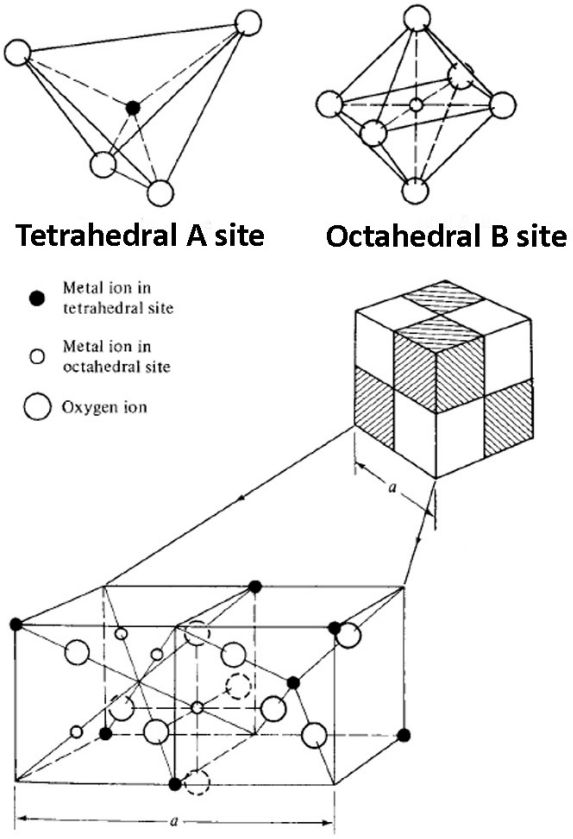

Figure 12: *Structure of cubic ferrite* [1].

The distribution of metal ions over octahedral and tetrahedral sites depends on nature of cation (valency, size), temperature and on the synthesis protocol. The predominant exchange energy in cubic spinel structure is negative, thus the sublattices are antiferromagnetically coupled. The metal ions occupying tetrahedral A or octahedral B sites interact via oxygen ions with super-exchange interactions. The strength of the exchange interaction depends on the distance between metal ions and the angle of M-O-M. The magnitude of the exchange interaction decrees in order: A-O-B > B-O-B > A-O-A. The largest magnitude of the exchange interaction indicates the antiparallel orientation of A and B sublattices. Consequently, the resultant magnetization is the difference between magnetization of total octahedral and tetrahedral lattices. The magnetic response of the cubic spinel ferrites thus significantly depends on the type and the distribution of metal cations through the interstitial sites [4].

Further the magnetic properties of cubic ferrite apart from crystal structure depend also on other parameters. The effect of particles was introduced in chapter 1.2.2. Apart

from particles size, the magnetic properties are significantly defined also with the size distribution and particles morphology. Especially when particles size is in the nano-range and below 10 nm, the surface effect related to the particles small size and consequent incomplete coordination of surface atoms becomes predominant [1]. Thus to obtain nanoparticles with desired magnetic properties, special attention needs to be given to their controlled synthesis.

My work comprises the study of the controlled synthesis of spinel iron oxide (Fe_3O_4 magnetite and γ-Fe_2O_3 maghemite) on the surface of colloidal core nanoparticles following heterogeneous root. Thus, in the following chapters, I will present the synthesis of spinel iron oxides, following different nucleation roots.

1.3 Synthesis of spinel nanoparticles

For the synthesis of the spinel iron oxides: Fe_3O_4 magnetite and γ-Fe_2O_3 maghemite (later referred to as spinel), numerous wet-chemical methods have been developed like microemulsions [9], sonochemical reaction [10], hydrothermal synthesis [11-12], thermal hydrolysis of precursors [13-15] and flow-injection synthesis [16]. The first challenge arising in all methods consists of defining experimental conditions leading to the desired particles size distribution. To meet the requirement for their application for example in medical fields, typically high monodispersity of the synthesized nanoparticles is required. The second critical point is to select the reproducible method that could be industrialized. Thus synthesis procedure involving complex synthesis and purification protocols like ultracentrifugation [17] or magnetic filtration [18] needs to be omitted.

Thermal decomposition of the metal-organic precursors (Fe-acetylacetonalte [13-14] Fe-pentacarbonyl, [15]) enables the synthesis of relatively narrow size distribution in the size-region between 4-16 nm [11]. However, the synthesis typically proceeds in organic solvents at elevated temperature (300 °C) [14]. Hydrothermal synthesis enables the spinel iron oxides synthesis with relatively narrow particles size. Here the control of the reaction parameters (time and temperature) together with the control of the concentration and ratio of reactants enabled the synthesis of nanoparticles between 10 to few tens of nm. The hydrothermal synthesis, however, proceeds at elevated temperature and pressure, thus special equipment is required. Good particle size control can be achieved also with the synthesis in microemulsions [19]. The synthesis typically precedes water-oil emulsions. The surfactant-stabilized nano-droplets act as a confined space that limits the particles growth. However, restrictions of methods are related to the low concentration of reactant in relation to high volume of the reaction mixture. Further the surfaces of the synthesized nanoparticles are grafted with surfactant, thus additional purifications steps are required.

The synthesis of spinel iron oxides proceeds also with the co-precipitation [20-24]. The method that otherwise enables only moderate control of the particles size and their distribution is, however, widely used due to its simplicity. Here the synthesis precedes in aqueous solution under mild reaction conditions. No special equipment is required since it proceeds under mild reaction condition (room temperature) and in atmospheric pressure. Further, the restriction related to the concentration of the reactant that is typical for the synthesis in microemulsions is not present. The spinel synthesis proceeds during the co-precipitation of Fe^{2+}/Fe^{3+} ions with the addition of hydroxide. The first stage involve the formation of Fe^{3+} hydroxide/oxide hydroxide that after addition of base that

initiates the precipitation of Fe^{2+} results in the formation of the iron oxide. The co-precipitation method enables the synthesis of the spinel nanoparticles of the size of approximately 12 nm [25]. Typically, the particle size increases with ageing of the reaction mixture. However, the spinel iron oxide (maghemite) is characterized with low solubility in alkaline medium, thus the increase in the particles size is negligible. It is however known that aging of the reaction mixture at pH 3 has an important effect on the final particles size [26, 27]. Here, aging of the Fe^{2+}/Fe^{3+} solution for over 30 min resulted in the increase in the final particles size. The size and also shape of the nanoparticles can otherwise be tailored relatively successfully by manipulating pH, ionic strength, temperature, and type of iron salts used. An important parameter is also Fe^{2+}/Fe^{3+} ratio. Spinel is synthesized only when the ratio Fe^{2+}/Fe^{3+} is 0.2 or more. When the ration is below 0.2, goethite phase (α-FeOOH) was formed instead [20, 21].

One of the main advantages of the spinel synthesis using the co-precipitation method is related to the large amount of particles that can be synthesized. However, the control of the particles size and their size distribution is limited since only kinetics factor are controlling the growth of the nanoparticles. After critical supersaturation is reached, a short burst of nucleation occurs, followed by slow growth of the nuclei by the diffusion of the solutes to the surface of the nanoparticles. For better understanding lets more deeply revise the kinetic stages involved during the solid state formation together with some thermodynamics considerations.

In the co-precipitation process the formation of solid phase (hydroxide, oxide hydroxide) is a result of the chemical reaction. The size of the formed solid particles yields in between few nanometers to micrometers. Particles size and morphology varies in the dependence of the synthesis conditions. To understand how small particles can form, and how the experimental conditions influence their characteristics it is necessary to review the kinetics aspects of the condensation mechanisms. The nucleation and condensation mechanism is rather complicated, however it can be subdivided into four major steps.

1.3.1 Nucleation

1.3.1.1 Homogeneous nucleation

Nucleation corresponds to the first step of the solid formation during the precipitation process. The precipitation of metal ions usually results in the hydroxide formation. Creation of nuclei proceeds with the condensation of the zero-charge precursor $[M(OH)_z(OH_2)_{n-z}]$. For the nuclei to be formed the concentration of the precursors must excides C_{min}. Typically the process is very fast and the nuclei form throughout the reaction volume. The condensation rate significantly depends on the precursors concentration that form in the presence of the hydroxyl ions. High hydroxyl ions concentration can be achieved with the addition of the base or during decomposition of thermally unstable molecules like urea [25, 26].

The driving force for the precipitation is the supersaturation S that can be that represents the relationship between the precursor concentration in the solution and solubility of the solid phase. The supersaturation is expressed with the following equation:

$$S = \frac{C_L}{C_S}$$

C_L precursor concentration
C_S solubility of the solid phase

The supersaturation rate significantly defines the size of critical nuclei formed. First nuclei start to form after the concentration of precursor exceeds its solubility that corresponds to area II in Figure 13. The probability of these nuclei to dissolve is higher than that to grow, thus these meta-stable nuclei are referred as embryos. The critical size of the stable nuclei is defined at maximum value of the free enthalpy of nucleation that decreases with increasing supersaturation and increasing surface tension [25, 27]:

$$\Delta G = -nkT \ln S + n^{2/3}(36\pi\Omega^2)^{1/3}\gamma \quad (5)$$

Ω molecular volume
γ surface tension

Beyond the critical concentration C_{min} the formed nuclei are stable (area III in Figure 13). Here the nucleation rate rapidly increases. The nucleation proceeds until the rate of precursor formation is higher than the rate of the condensation. When the precursor concentration drops below critical concentration the nucleation stops. Once the precursor concentration again reaches critical value, the formation of new nuclei is no longer possible.

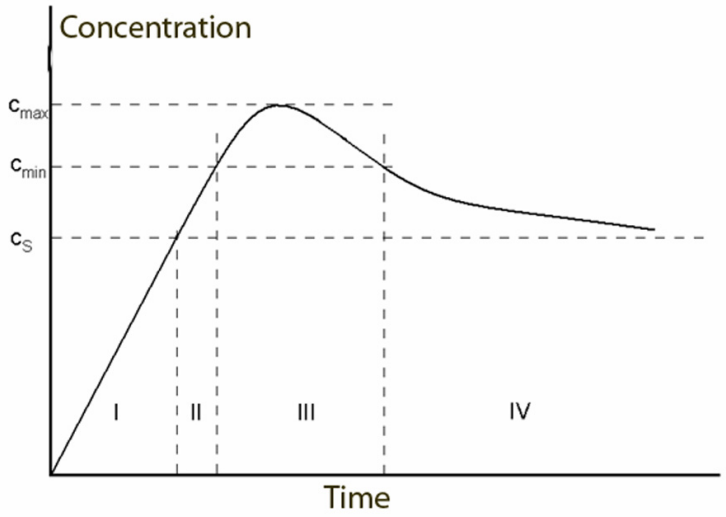

Figure 13: *Concentration of soluble precursors of solid phase during precipitation [18].*

1.3.1.2 Heterogeneous nucleation

The nucleation rate can also be influenced by the presence of the solid crystals in the system. The occurrence of these solid crystals in the system by lowering the nucleation barrier gives rise to the increase in the nucleation rate. The activation energy for the formation is lowered due to the differences in the surface energy γ that is lower for the

solid-solid than for the liquid-solid. Hence the nucleation on the surface of foreign bodies occurs more easily. The nucleation rate is given by:

$$J = B\exp\left\{-f\frac{16\pi}{3}\frac{\Omega^2\,\gamma_{cf}^3}{(KT)^3\left[\ln\left(1+S^2\right)\right]}\right\} \tag{6}$$

B kinetic constant,
γ_{cf} specific interfacial free energy between

Here the parameter f describes the influence of the foreign particles on the nucleation barrier. On the basis of equation (6), the heterogeneous nucleation seems kinetically always favorable meaning that at low supersaturation the heterogeneous nucleation will dominate while higher supersaturation favours the homogeneous one.

However, additional factors related to the size, crystal structure and morphology of foreign particles need to be considered, since their presence can lead to more than one nucleation processes in the same system and different rates of supersaturation.
It is known that when foreign particles have good structural match with the nucleating phase then at conditions favouring low supersaturation the epitaxial growth of the nuclei will be obtained. Heterogeneous nucleation also allows the coatings of different oxides [25, 27].

1.3.1.3 Growth

Once the concentration of precursor drops below critical concentration the nucleation stops and when it again increases close to C_{min}, the nucleation rate is very low. Instead the precursor preferentially condenses on the existing nuclei following the same chemical mechanism as during the nucleation. This results in the nuclei growth (area IV, Figure 13). The final particles size depends on the number of formed particles and the on the amount of matter available during the synthesis, whereas the width of the particles size distribution is related to the mechanism of the nuclei growth.

1.4 Colloidal suspensions

Colloids are characterized as a systems consisting of two separate phases. Typically small solid particles are dispersed in the carrier liquid. The size of dispersed particles yields between 1 nm to 1μm. The colloidal stability of dispersed particles is influenced by the different forces acting on the particles. Particles tend to sediment due to the effect of the gravitational forces. The energy of the gravitational forces depends on the particles' size and on the density differences ($\Delta\rho$) between particles and dispersing medium. In general then smaller the particles size and the smaller the differences in densities results in the smallest the strength of the gravitational field [6].

For the particles smaller than 1 μm the effect of thermal energy becomes important. The particles sedimentation is hindered due to the thermal agitation resulting from Brownian motion. Thermal energy depends on the type of material and on the temperature. The colloidal stability of the particles in the gravitational field is thus determined with the interplay between gravitational and thermal energy expressed with the following relation:

$$\frac{\text{gravitational energy}}{\text{thermal energy}} = \frac{\Delta\rho g L V}{kT}$$

$\Delta\rho$ density differences between particles and dispersing medium
V particles volume

Due to the Brownian motion the particles interact between each other. Due to the small size, the particles shows large tendency toward agglomeration, that is even more pronounced when their size is reduced in the range of few to few-tens of manometer. Particle forming agglomerates due to increased size tends to sediment in gravitation field. Apart from the forces acting on the particles also interaction between the particles also has an important effect on the particles colloidal stability [6].

In general, forces between magnetic metal oxide nanoparticles in liquids are attractive and repulsive. The attractive forces are van der Waals and magnetic dipole-dipole forces. The repulsion between particles is established by repulsive electrostatic forces and steric forces, which are present when particles' surface is covered with some organic or inorganic molecules [29].

1.4.1 Interaction between colloidal particles

When two particles in colloidal suspension approach, the attractive van der Waals forces acting between them result in their attraction. Oppositely acting forces, causing the repulsion between colloidal particles are referred as electrostatic forces. The repulsive electrostatic forces originate from particles surface charge. The oxide particles, when dispersed for example in water develop surface charge. The surface charge originates from surface -OH groups ionization or chemisorptions of water molecules [25]. The ionization of surface groups strongly depends on the pH of medium. The charge of surface groups can be either negative (O^-), zero or positive (OH_2^+) and gives the surface a basic, acidic or neutral character. The charge surface groups develop strong interaction with surrounding medium, causing its structural rearrangement in a way that oppositely charged ions form electrical double layer with the particles surfaces (Figure 14). The thickness of double layer strongly depends on the polarity of the surface and the pH and ionic strength of the surrounding medium.

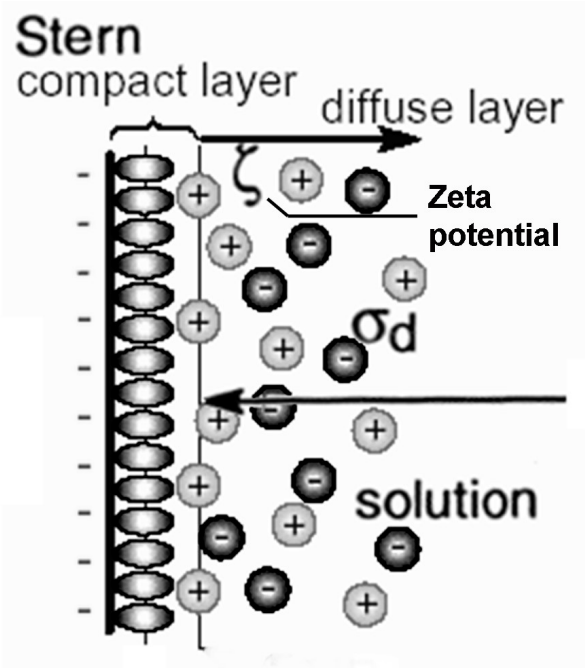

Figure 14: *Schematic illustration of the structure of the electric double layer* [25].

The stability of the dispersed particles toward aggregation and flocculation is described by the DLVO (Derjaguin, Landau, Vervey, Overbeek) theory. The theory considers the effect of attractive and repulsive forces and allows the estimation of the energy barrier to avoid particles contact.

Total interaction energy is the sum of the repulsion and the attractive energy $V_T = V_A+V_R$. The DLVO theory is valid in several cases, but when the particles are too close together the theory cannot describe interactions between particles. The theory combines the forces of two kinds:

(i) Attractive forces (London van der Waals forces), which are always present and are a function of the materials involve.

(ii) Repulsive forces caused by the interaction between electrical double layers and controlled by the physicochemical parameters of the system.

The Van der Waals forces are resulting as a consequence of fluctuations in the dipolar interactions at the molecular level. For two identical spherical particles with radius a, with surface separated by the distance D, the potential energy V_A is expressed withthe following equation. [25]

$$V_A = -\frac{A}{6}\left(\frac{2a^2}{R^2-4a^2}+\frac{2a^2}{R^2}+\ln\frac{R^2-4a^2}{R^2}\right) \tag{7}$$

A effective Hamaker constant

R center-to-center separation distance ($R = D+2a$)

The electrostatic repulsion occurs when two-like charged particles approach each other. More precisely the repulsion is a result of the overlap of the particles electrical double layers. In the diluted system the electrostatic interactions of only two particles can

be considered and expressed with following equation [25].

$$V_R = \frac{128\pi a_1 a_2 n_\infty kT}{(a_1 + a_2)\kappa^2}\gamma_1\gamma_2 \exp(-\kappa h) \tag{8}$$

h surface-surface separation between the particles,
a particles radius
κ Debye-Hückel reciprocal length
n_∞ bulk density of ions

$$\gamma = \tanh(\frac{ze\psi}{4kT})$$

The strength of the electric repulsion strongly depends on the pH and the ionic strength of the media. In general, in the system consisting of particles with higher charged surfaces in the diluted electrolytes strong repulsive forces will develope between approaching particles. Conversely, in the system of weakly charged surfaces in solution with high ionic strength the total interaction energy will be close to van der Waals energy, that will result in the flocculation of the particles (Figure 15). For highly charged surface however in the presence of a concentrated electrolyte, the total energy exhibits a small minimum (secondary minimum) prior to the barrier (Figure 15) [25].

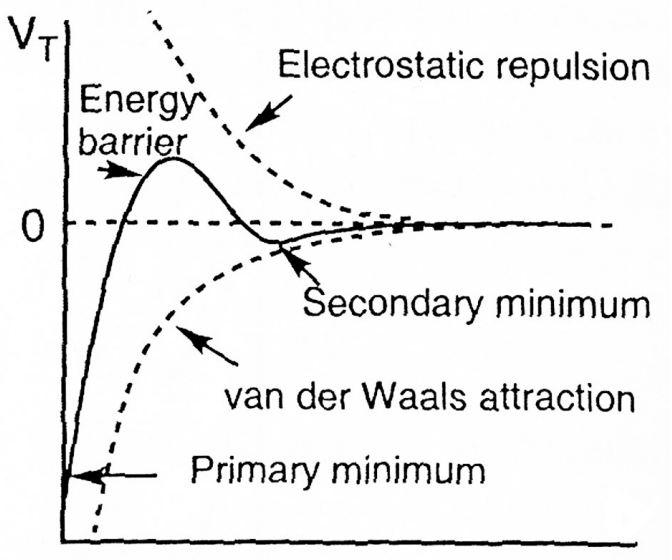

Figure 15: *Interaction energy V_T as a function of distance between particles [25].*

The combination of two opposite potentials (van der Waals attraction potential and electric repulsion potential) as a function of distance between spherical particles is shown in Figure 15. Both van der Waals attraction potential and electrostatic repulsion potential reduce to zero at distances far from solid surfaces. The maximum of the total energy also known as the energy or repulsion barrier occurs when the particles are further apart and the electrostatic potential dominate the attractive potential. When the energy barrier is greater than ~ 5 k_BT, the collision of two particles, produced by Brownian motion, will not overcome the barrier and the agglomeration will not occur [25]. The secondary minimum is present only when the concentration of counter-ions is high enough. This happens, for example when particles surface has a large surface charge density. If

secondary minimum is established, the particles associated with each other, which is known as flocculation. [5,6]

1.4.2 Magnetic interactions

Ferri/ferromagnetic metal oxide nanoparticles have large tendency for agglomeration due to magnetic dipole-dipole interactions. The dipole-dipole energy, E_{dd} of the two neighbouring particles is expressed by

$$E_{dd} = -\frac{\mu_0 m_0^2}{4\pi R^3} \tag{9}$$

R distance between two particles centres
m_0 magnetic moment
μ_0 permeability of vacuum.

However the dipole-dipole interactions become negligible when the size of the particles is reduced below the critical diameter (usually around 10-20 nm) and the particles are in or close to superparamagnetic state. When particles are in such state, their magnetic moments are free to flocculate in the response in the thermal energy, so there is no net magnetization, in the absence of the external field. Between superparamagentic particles, there is no magnetic interaction that would cause their agglomeration.
Hence, due to the high active surface the particles have a still large tendency for agglomeration, so attractive van der Waals forces have to be suppressed by applying various protective agents onto the particles' surface [31].

Since the nanoparticles colloidal stability is a crucial requirement for almost any applications, it is necessary to apply protection strategies to achieve colloidal stability of the "naked" magnetic particles. These strategies comprise grafting of or coating with organic species, including surfactants or polymers, or coating with inorganic layer, such as silica or carbon [32]. It is noteworthy that in many cases the protecting shells not only stabilize the nanoparticles, but can also be used for further functionalization, for instance with another nanoparticle or various ligands, depending on the desired applications.
Stable suspensions of superparamagnetic nanoparticles, usually called ferrofluids, have found many applications in technology [33] and more recently especially in biomedicine [34]. Frequently, stable suspensions are also a prerequisite for the preparation of some magnetic materials, such as magnetic nanocomposites and magnetic coatings.

2 Aims and Hypothesis

The knowledge related to the preparation of magnetic coatings of iron oxides on the surface of the colloidal core nanoparticles of different functionalities carries significant importance since it enables the preparation of different multifunctional core-shell nanocomposite particles. Magnetic iron oxides have already been found as promising materials for the various applications in technology and in modern medical applications. The synergy of different functionalities in the core-shell nanocomposite particles, i.e, magnetic-magnetic, magnetic-photocatalytic, magnetic-ferroelectric, etc., would even enhance the possibilities for these nanocomposites to be applied. Despite very large importance, data in the literature comprise only limited reports on the iron-oxide coating that are characterized with complicated synthesis procedures that often enable only poor control of the synthesis of the coating.

The objective of my work was to develop a method enabling the controlled synthesis of uniform layers of magnetic iron oxide (further referred to as spinel) on the surfaces of the core nanoparticles involving heterogeneous nucleation. For the spinel coating synthesis I have selected co-precipitation of Fe^{2+}/Fe^{3+} ions from the aqueous solution. The co-precipitation is a simple and at the same efficient method that enables synthesis of spinel nanoparticles. The spinel nanoparticles are usually synthesized using co-precipitation of Fe^{2+}/Fe^{3+} ions initiated by the addition of hydroxide. First, the Fe^{3+} ions precipitate at pH of 2.8, while higher pH around 6.2 is required for Fe^{2+} precipitation. Such ordinary synthesis procedure, however, involves high supersaturation of the nucleating species which results in homogeneous nucleation and is not appropriate for coating.

I assumed that the heterogeneous nucleation of nucleating species would occur when reaction conditions involving low supersaturation will be achieved. I predicted that this would be achieved with slow and homogeneous release of reactants through the reaction mixture. Thus, the first part of my thesis was aimed to evaluate (i) whether the spinel iron oxide can be synthesized as single product under conditions involving low supersaturation and (ii) wether low supersaturation of the nucleating species will result in their heterogeneous nucleation on the core surfaces while their subsequent transformation will result in the spinel coating.

The objective of the second part of the thesis was to evaluate the effect of the core nanoparticles size, size distribution, morphology and finally their crystal structure on the course of the spinel coating synthesis. Thus, the spinel coating was done on surfaces of the amorphous silica and the crystalline Ba-hexaferrite core nanoparticles of different sizes. The objective of the third part was aimed to evaluate the magnetic properties of synthesized nanocomposites consisting of the hard-magnetic hexaferrite coated with soft magnetic spinel.

3 Materials and Methods

3.1 Materials

For the synthesis described in my thesis, I have used the following chemical reagents:

- Iron (III) nitrate hepta hydrate, Alfa Aesar
- Iron (II) chloride, Alfa Aesar
- Magnesium Hydroxide, Alfa Aesar
- Sodium hydroxide, 98%, Alfa Aesar
- Urea, Alfa Aesar
- Barium nitrate, Alfa Aesar
- Nitric (V) acid, Alfa Aesar
- Silica nanoparticles, Carbosil MP, SupelCo
- Citric acid, 99+% Alfa Aesar
- *N,N*-Dimethylformamide, ACS, 99+% Alfa Aesar
- 1,2-Dichlorobenzene, Alfa Aesar
- *n*-Hexane, Alfa Aesar
- Ethanol, 99.5, Carlo Erba
- Acetone p.A., 99.5% AppliChem
- Oleic acid, Alfa Aesar
- (3-aminopropyl)-3etoxy silane, 98%, Alfa Aesar

3.2 Synthesis Methods

3.2.1 Synthesis of the spinel with homogeneous nucleation

The spinel synthesis proceeds with coprecipitation of Fe^{2+}/Fe^{3+} ions with addition of precipitating agent. Fe^{3+} ions were first coordinating with urea according to the procedure described in the literature [35]. Here $Fe(NO_3)_3$ $9H_2O$ (n = 0.012 mol) were dissolved in the ethanol (V = 250 mL). Second, urea (n = 0.1 mol) dissolved in 100 mL of ethanol was admixed into Fe^{3+} ions solution forming green precipitate of $[Fe((CO(NH_2)_2)_6)](NO_3)_3$ complex (later referred to as Fe^{3+}-urea). After mixing at room temperature for 2 hours, the precipitates were collected and washed with ethanol and dried for subsequent reactions.

The spinel synthesis proceeded in a three-necked flask equipped with pH meter, thermocouple and condenser. First, Fe precursors (Fe^{3+}-urea (n = 0.12 mmol) and $FeCl_2$ (n= 0.06 mmol)) were dissolved in argon bubbling distilled water (50 ml) heated to final temperature (50, 60 or 70 °C). The solution of Fe precursors then remained at final temperature for the selected time interval (t_1 = 0, 10 or 60 min). After elapsing t_1 the precipitating agent $Mg(OH)_2$, (n = 0.024 mmol) or urea ($CO(NH_2)_2$, excess) was admixed into the Fe-precursors solution. The addition of precipitating agent resulted in the increase

in hydroxide ions in the reaction solution that resulted in the precipitation of Fe^{2+} ions. To avoid oxidation of the Fe^{2+} and formation of secondary phases that can be formed with different precipitating agents, the reaction mixture was continuously bubbled with argon during the course of reaction. The change in pH of the reaction mixture during the reaction was measured with pH-meter. Only after the reaction mixture remained at final pH for approximately 2 hours, the reaction was stopped. The reaction mixture was cooled down during argon bubbling, when finally the synthesized nanoparticles were recovered after several washings with distilled water and dried for the analysis.

3.2.2 Synthesis of the spinel with heterogeneous nucleation

To achieve the coating of the spinel on the surface of selected colloidal nanoparticle (later referred to as core nanoparticles), the synthesis proceeded in stable aqueous suspension of the core-nanoparticles. The spinel synthesis proceeded in the suspension of amorphous silica core nanoparticles or in the suspension of Ba-hexaferrite core nanoparticles.

3.2.2.1 Synthesis of core nanoparticles

Stable suspension of the amorphous silica-core nanoparticles was prepared by suspending commercially available silica nanoparticles (average diameter of globular particles = 25 nm) (n = 0.8 mmol) in 50 ml of distilled water. Suspending silica-core nanoparticles during ultrasound yielded a stable aqueous suspension due to high negative zeta potential.

Stable aqueous suspension of the silica core nanoparticles with positive surface charge was prepared by grafting silica surfaces with hydrolyzed aminopropyl silane [36]. Aminopropy silane (APS, n = 0.1 mmol) was first dissolved in ethanol (EtOH, V= 10 ml) and second during vigorous stirring added into the aqueous suspension of silica core nanoparticles (n = 0.8 mmol, V = 50 ml). The pH of the suspension was adjusted to 10.5 with diluted ammonia solution. The suspension was then heated to 60 °C for 6 hours.
After reaction was completed, the silica-core nanoparticles were washed with water and acetone to remove unadsorbed APS. APS-grafted silica-core nanoparticles were dispersed in water, where protonated APS amino groups enabled high positive surface charge.

Another type of core nanoparticles was Ba hexaferrites. To obtain the different particles size and morphology the Ba hexaferrites core nanoparticles were synthesized with hydrothermal synthesis [37].

In brief, the solution of metal ions (n(Ba) = 4.16, n(Fe) = 20.8 mmol) was precipitated with the addition of a large excess of NaOH (n = 1.07 mol) giving rise to the precipitation of the hydroxide precursors. The suspension of the precursors was then sealed in an autoclave vessel and heated to the desired temperatures (150-270 °C). After the reaction was completed the products were washed with diluted nitric acid (to dissolve Ba rich phases that formed because of the excess of Ba) and distilled water. After re-suspending the Ba-hexaferrite nanoparticles in water at pH = 4.7, high positive ζ- potential enabled their colloidal stability.

Ba-hexaferrite nanoparticles were also synthesized also in the presence of oleic acid. Here oleic acid (n = 0.01 mol) was slowly added into the suspension of the Fe precursors prior to the hydrothermal synthesis. During the synthesis the oleic acid adsorbed on the surfaces of nanoparticles and thus blocked their exaggerated growth. After the synthesis hydrophobic Ba hexaferrite-nanoparticles were precipitated with nitric acid and washed several times with acetone. The oleic acid, adsorbed on nanoparticles' surfaces, enabled their colloidal stability in hexane, thus a relatively concentrated stable suspension was

prepared. To ensure their colloidal stability in water, the oleic acid was exchanged with the citric acid in a ligand-exchange reaction [36]. In brief, the oleic acid coated Ba hexaferrite core nanoparticles (m = 1 g) were suspended in 1,2-dichlorobenzene and *N*,*N*-dimethylformamide (50:50, total volume 15 mL). In the second step, the citric acid (n = 0.002 mol) was added into the suspension followed by heating to 100 °C for 24 hours. After the reaction was completed the Ba-hexaferrite core nanoparticles were precipitated with addition of diethyl ether, washed with acetone and re-suspended in water. The adsorbed citric acid, enabled high negative zeta potential and thus colloidal stability of the Ba-hexaferrite core nanoparticles in water.

3.2.2.2 Synthesis of nanocomposite particles

To achieve spinel coating on the selected core nanoparticles (silica or Ba-hexaferrite core nanoparticles), spinel synthesis proceeded in stable aqueous suspension of the core nanoparticles. Fe^{3+}-urea complex (n = 0.12 mmol) and $FeCl_2$ (n= 0.06 mmol)) were dissolved into argon bubbling aqueous suspension of amorphous silica-core nanoparticles (n= 0.8 mol, V = 50 ml) heated to the temperature of 60 °C. The amount of silica core-nanoparticles was estimated in a way to obtain desired surface area of 5.45 x 10^{18} nm^2, that for 25 nm particles yielded 0.8 mol. If all the formed spinel would coated onto the core nanoparticles, the concentration of Fe precursor would results in 3 nm thick shell.

After elapsing t_1, the $Mg(OH)_2$ was added into the reaction mixture, giving rise to the precipitation of Fe^{2+}. Only after the reaction mixture remained at final pH for approximately 2 hours the reaction was cooled down during argon bubbling, when finally the synthesized S@SiO_2 nanocomposite products were recovered after several washing with distilled water and dried for the analysis.

To obtain further insights into the mechanism of spinel formation, small volumes (approximately 5 ml) of intermediate products (of final product S@SiO_2) were sampled also during the early stages of the reaction and analyzed with transmission electron microscopy. Typically, the reaction mixture was sampled 2 times. First after it maintained at final temperature for selected time interval (t_1 = 0, 10 or 60 min) (Stage1) and after the addition of $Mg(OH)_2$ caused precipitation of Fe^{2+} resulting in the spinel formation (Stage 2).The sampled volumes were centrifuged immediately after the sampling to separate the formed precipitates from the precursors solution. Subsequently the precipitates were washed with water.

The synthesis of spinel proceeds also in the stable colloidal suspension of Ba-hexaferrite core nanoparticles. Here the synthesis of S@BaM nanocomposites proceeds under the same reaction conditions as in the synthesis of the S@SiO_2 products. Depending on the Ba hexaferrite core nanoparticles size, the concentration of the hexaferrite-core nanoparticles suspension was determined to obtain the same surface area (5.45 x 10^{18} nm^2) as in the synthesis of S@SiO_2 nanocomposites.

3.3 Characterization techniques

3.3.1 X-ray powder diffraction

The phase compositions of the product nanoparticles synthesized homogeneously in the solution were analyzed with XRD. The XRD patterns were recorded using the PANalytical X' Pert PR diffractometer. For a product consisting of cubic spinel phase the particle size was evaluated from the broadening of line-width using Software Diffrac TOPAS^{TM}.

3.3.2 Electro-kinetic measurements

ζ-potential of suspended Ba hexaferrite and silica core nanoparticle were evaluated with electro-kinetic measurements. The measurements were done using ζ--meter ZetaPALS Brookhaven Instruments Corporation.

3.3.3 Transmission electron microscopy

The structural analysis product nanoparticles were characterized with TEM equipped with EDXS. For the TEM analysis, the nanocomposite particles were suspended in ethanol and deposited on copper-grid-supported perforated electron-transparent carbon foil. TEM specimens for core (BaM, SiO_2) nanoparticles were prepared by drying the stable suspension on grid-support. The HREM images of core and nanocomposite particles were recorded using the JEM-2010F TEM microscope operated at 200 keV.

The quantification of the recorded EDXS spectra of the S@BaM nanocomposite was done using Oxford ISIS software. The spectrum taken at large well crystalline Ba hexaferrite nanoparticles [37] was taken as a standard during the quantification of spectra collected at S@BaM nanocomposite particles. The relative error estimated for Fe/Ba ratio was less than ± 5% [38]. To evaluate the homogeneity in terms of the chemical composition of the S@BaM nanocomposite particles, the systematic EDXS analysis were performed. First, to evaluate the relative error of the method 6 spectra were recorded over single nanoparticles. Second, the spectra recorded from different regions of the specimen were compared. The estimated error yields 15% for Ba and less than 3% for Fe.

3.3.4 Vibrating sample magnetometer

The magnetic response (MH hysteresis) of the synthesized S@BaM nanocomposite particles and untreated BaM-core nanoparticles was evaluated using the vibrating sample magnetometer (VSM) Lake Shore 7307 VSM. The maximum field applied was in the range 1T and -1T.

Magnetic response was also evaluated for the homogeneous mixture of BaM_{100} core nanoparticles and superparamagnetic spinel iron oxide (γ-Fe_2O_3, denotes as S). Here to minimize the inter-particles interaction both BaM_{100} and spinel nanoparticle were first coated with oleic acid and second, in low concentrations homogeneously dispersed in wax.

Magnetic hystereses were measured also for the magnetically oriented assemblies of the S@BaM_{100} nanocomposite and BaM_{100} core nanoparticles. First nanoparticles of S@BaM_{100} and BaM_{100} nanoparticles were hydrophobized and dispersed in liquid wax. The particles were magnetically oriented in a homogeneous field of 1T. Solid assembly was obtained by cooling in the field. The magnetic hystereses were measured parallel and perpendicular to the samples' magnetic easy axis.

3.3.5 Thermo-gravimetric method

Thermogravimetric analysis was used to the determine concentration of the Ba hexaferrite nanoparticles in stable aqueous suspensions used in spinel synthesis.

3.3.6 Infrared spectroscopy

The formation of the $[Fe((CO(NH_2)_2)_6)](NO_3)_3$ was confirmed with Attenuate Total Reflection Infrared Spectroscopy (ATR). The ATR spectra were recorded on a Bruker Vector 22**.**

3.3.7 UV-Vis Spectroscopy

Thermal decomposition of the $[Fe((CO(NH_2)_2)_6)](NO_3)_3$ complex was analyzed using the UV-Vis *in-situ* spectroscopy. Diluted solution of $[Fe((CO(NH_2)_2)_6)](NO_3)_3$ complex was sealed in a cuvette and heated with the rate of 1°C/min from 20–80 °C. During the heating the UV-Vis spectra were recorded at selected temperatures.

4 Results

The aim of this thesis was to synthesize uniform layers of magnetic iron oxide (later in the text referred to as spinel) on the surfaces of selected colloidal core nanoparticles thus preparing core-shell nanocomposite particles.

Magnetic iron-oxide magnetite or maghemite nanoparticles are usually synthesized using simple co-precipitation from the aqueous solution of mix valent Fe^{2+}/Fe^{3+} ions with addition of hydroxide. The method involves the high supersaturation leading to homogeneous nucleation of the nanoparticles in the solution. First, the precipitation of Fe^{3+} ions proceeds at the pH of 2.8, while the higher pH value of 6.2 is required for Fe^{2+} precipitation. Precipitated Fe^{3+} hydroxide immediately transforms into Fe oxide-hydroxide (FeOOH), which at pH above approximately 8 further transforms into iron oxide. Experimental conditions used define the modification of FeOOH phase. In the presence of Fe^{2+} γ-FeOOH modification transforms into magnetic iron oxide with spinel structure, magnetite (Fe_3O_4). In the ambient air the magnetite nanoparticles oxidizes into maghemite (γ-Fe_2O_3). If thermodynamically-stable α-FeOOH is formed during precipitation, it can further transform only to nonmagnetic hematite (α- Fe_2O_3) [40,41].

Morphology of the product particles and the type of nucleation (homogeneous/heterogeneous) both depend on the supersaturation of the product caused by chemical reactions. I assumed that in chain of subsequent reactions leading to the spinel formation, the precipitation of the first phase formed (further in the text named initial product), decisively defines the morphology of the nanoparticles of the final spinel product. I also assumed that the final spinel product will remain as the coating on the core nanoparticles if the initial product will be heterogeneously nucleated. During the Fe^{3+}/Fe^{2+} precipitation $Fe(OH)_3$ or one of several modifications of FeOOH appears as the initial product. To synthesize the spinel, the conditions have to favor formation of γ-FeOOH. Formation of α-FeOOH will not result in further formation of spinel. However, even γ-FeOOH will only transform into the spinel when Fe^{2+} ions are precipitated at higher pH. Generally, the γ-FeOOH forms at lower pH and only under specific conditions transforms into thermodynamically-stable oxide-hydroxide α-FeOOH. Transformation of γ-FeOOH requires presence of Fe^{2+} and increased pH over 6.2. In defining the conditions favoring transformation of γ-FeOOH-to-spinel, problems may arise due to the large difference in pH of Fe^{3+} (pH=2.8) and Fe^{2+} (pH~6.2) precipitation. In synthesis of the spinel nanoparticles with homogeneous nucleation, the transformation of the γ-FeOOH to α-FeOOH is suppressed by very fast increase in pH with sudden addition of hydroxide.

To coat spinel on the surfaces of the core nanoparticles with heterogeneous nucleation of the initial product of the precipitation of Fe^{3+}/Fe^{2+} ions, the supersaturation of the initial product should be closely controlled. The supersaturation must be below the level required for the homogeneous nucleation, however, high enough for heterogeneous nucleation to proceeds. The supersaturation is defined by the kinetics of the chemical reactions of the initial product formation and on the concentrations of the reactants, i. e, Fe^{3+}/Fe^{2+} ions and hydroxyl ions. Ionic chemical reactions in water are generally very fast and therefore difficult to be controlled. In approximation we can say that because of the very fast reaction the supersaturation only depends on the concentration of the reactants. However, it is very difficult to maintain homogeneous concentration of the reactants

throughout the whole volume of the reaction vessel. The actual concentration of the reactants critically depends on the mixing. To keep the supersaturation low enough to avoid the homogeneous nucleation, the concentration of the reactants should be low. However, under such conditions, it is impossible to prevent γ-FeOOH to at least partially transform into α-FeOOH. The solution can be in immobilizing the Fe^{3+} into the complex, which only decomposes at the conditions close to those needed for the Fe^{2+} precipitation. At the same time, the problem with non-homogeneities caused by non-ideal mixing of the reactants can be diminished, since the Fe^{3+} is released from the complex homogeneously throughout the whole volume of the vessel. Moreover, the supersaturation can be controlled with the kinetics of Fe^{3+}-complex decomposition. I tested different organic ligands (citrate, oxalate, urea) for the synthesis of Fe^{3+}-complexes and studied their thermal decomposition. Finally, I choose the Fe^{3+}-urea complex ($[Fe((CO(NH_2)_2)_6)](NO_3)_3$).

Apart from the control of the Fe^{3+} release, the release of the hydroxyl ions can also be controlled to improve homogeneity of the reaction mixture and to maintain the desired level of the supersaturation. Here, I tested several precipitating agents including $Mg(OH)_2$ and urea. The $Mg(OH)_2$ solid is admixed into the solution of the Fe-precursors, the mixture of Fe^{3+}-urea complex and Fe^{2+} ions and by its dissolution the hydroxyl ions are released homogeneously throughout the whole volume while their concentration can be controlled by temperature. Also urea ($CO(NH_2)_2$) can be used to homogeneously increase the pH of the solution. Urea is dissolved in the solution of the Fe-precursors and the hydroxyl ions are released by its thermal decomposition.

The main hypothesis of the thesis states that the spinel iron oxide can be coated onto the core nanoparticles by heterogeneous nucleation during co-precipitation of Fe^{3+}/Fe^{2+} from the aqueous solution. The heterogeneous nucleation can be achieved when the supersaturation of the initial product is closely controlled by assuring homogeneity and the appropriate concentration of the reactants throughout the reaction mixture. That can be achieved using:

1. Controlled release of the Fe^{3+} from the Fe^{3+}-urea complex
2. Controlled release of the hydroxyl ions from appropriate precipitating agent.

The following chapter describes the study of the experimental conditions leading to formation of single-phase spinel under conditions defined by above stated hypothesis. In next chapter the coating of the spinel layers onto the silica and the hexaferrite core nanoparticles are described.

4.1 Synthesis of the spinel with homogeneous nucleation

As I argued above, low supersaturation is required for the heterogeneous nucleation. First study involves set of experiments of the spinel synthesis under conditions set to control the supersaturation in the range, where heterogeneous nucleation is expected.

4.1.1 Controlled release of iron ions from Fe^{3+}-urea complex

One way to control the supersaturation and also to achieve the simulations precipitation of

Fe^{3+} and Fe^{2+} ions is the use of the coordinating reagent forming water-soluble complex with Fe^{3+}. The immobilization of free Fe^{3+} ions into the complex postpones its precipitation to higher pH, where Fe^{2+} precipitates. The decomposition of the complex can be triggered by increased temperature. The decomposition of the Fe^{3+}-urea complex ($[Fe((CO(NH_2)_2)_6)](NO_3)_3$) was studied under conditions that were later used in the coating of the core particles with the spinel. During coating, the solution of the Fe^{3+}-urea complex and the Fe^{2+} ions (Fe precursors) with low pH of 2.2 was heated and only after certain time at the temperature the hydroxide was added.

The complex of Fe ions and urea was synthesized with the addition of urea into the ethanol solution of Fe^{3+} nitrate. The formed $[Fe((CO(NH_2)_2)_6)](NO_3)_3$ complex was analyzed with ATR-IR spectroscopy. The spectra of pure urea shown on Figure 16 reveals, apart from characteristic bands of an amino group $\nu(NH_2)$ at 3437 and 3338 cm^{-1}, also two peaks at 1673 cm^{-1} and 1430 cm^{-1} that are ascribed to stretching vibrations of CO and CN bonds, respectively. The stretching vibrations of these characteristic groups typically shifts toward lower frequencies for CO vibration and higher frequencies in CN vibrations if there is a coordination through the oxygen atom of the carbonyl group. Such shift is observed in the IR spectra of the Fe^{3+}-urea complex (Figure 16b) where ν(CO) and ν(CN) results in 1626 and 1508 cm^{-1} thus confirming the formation of the $[Fe((CO(NH_2)_2)_6)](NO_3)_3$.

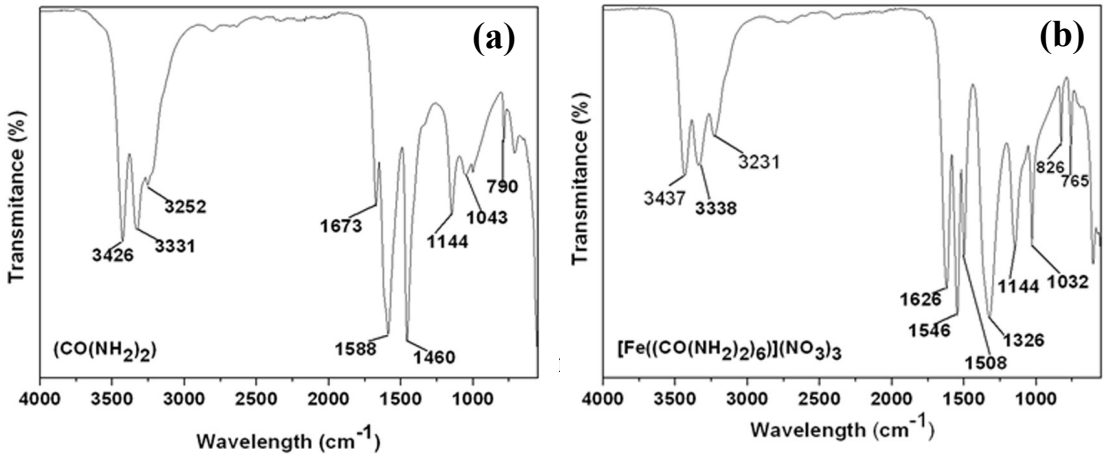

Figure 16: *ATR-IR spectra of urea (a) and Fe^{3+}-urea complex (b).*

The stability of the Fe^{3+}-urea complex was tested at different pH values. Dissolving the Fe-urea complex in water resulted in the yellow solution with pH of 2.2. The Fe^{3+}-urea solution remained as clear solution even when pH was raised to the value well above the 2.8, required for the precipitation of Fe^{3+} ions. Only when the Fe-urea solution at pH around 10 was heated to the temperatures above 45 °C, the rapid precipitation of Fe^{3+} occurred due to the complex decomposition.

Heating of the Fe^{3+}-urea solution in the acidic medium of pH 2.2 resulted in change of the solution color from yellow to dark orange when temperatures approach 48 °C, indicating that the Fe^{3+} most likely released from the Fe^{3+}-urea complex and maintained in the solution in the form of hexaaqua ions ($[Fe(H_2O)_6]^{3+}$) [2]. Since urea starts to decompose only after the temperatures above 65 °C, the Fe^{3+} ions obviously released due to the complex decomposition while the urea molecules remained intact.

The temperature dependence of the Fe-urea complex was additionally studied with UV-Vis *in-situ* measurements. UV-Vis spectra of the Fe^{3+}-urea complex recorded at 20 °C (Figure 17) reveals a strong absorption band at 389 nm originating from Fe^{3+}-Fe^{3+}

ligand field and Fe^{3+}-Fe^{3+}pair transitions [2], while UV-Vis spectra of pure urea show weak absorption band slightly below 200 nm [42].

Additionally, UV-Vis *in-situ* heating measurements were done where acidic solution of the Fe^{3+}-urea complex was hated from temperature of 20 to 80 °C with the rate of 1K/min, while the UV-Vis spectra were recorded in the temperature intervals of 1 K. The selected representative UV-Vis spectra, recorded at the different temperatures are plotted in the graph in Figure 17.

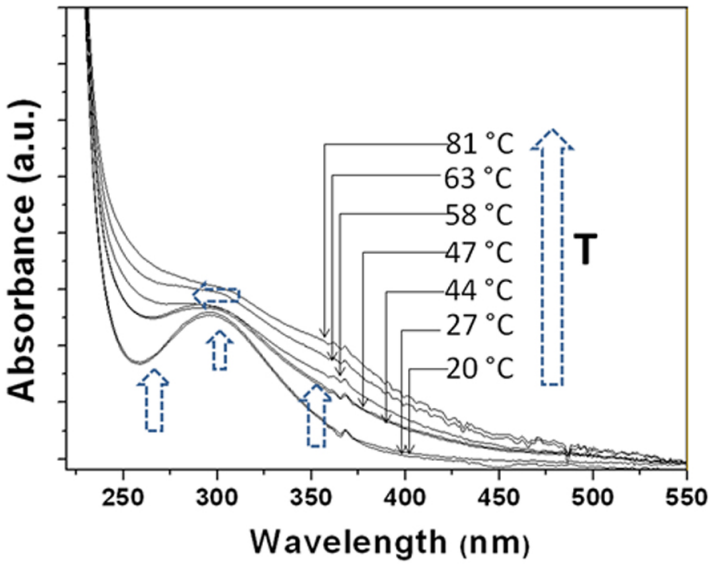

Figure 17: *UV-Vis In-situ measurements of Fe^{3-}-urea complex at increasing temperatures.*

The spectra recorded between 20 and 40 ° C showed no changes in UV-Vis absorption. However, when the temperature approached 44–47°C, strong increase of the absorption bands at 260 and around 350 nm was observed while only slight increase in the absorption around 300 nm is detected. As the temperature further increases from 60 °C to 80 °C the recorded UV-Vis spectra reveals further increase in the absorption bands at 260, 300 and 350 nm. The appearance of the additional absorption bands in the range around 250 and 350 nm and slight increase at 300 nm at temperatures up to 60 °C is consistent with the formation of the γ-FeOOH phase, where the typically absorption band for the Fe^{3+}-Fe^{3+} ligand field and the Fe^{3+}-Fe^{3+} pair transitions are observed at 329, 304 and 359 nm [2]. At further increase of the temperature the absorption bands at 300 and 350 nm increased in enhanced manner in comparison to the absorption maximum at 260 nm, which indicates that α-FeOOH phase is formed in parallel with the γ-FeOOH. The Fe^{3+}-Fe^{3+} ligand field and the Fe^{3+}-Fe^{3+} pair transitions for the α-FeOOH phase are typically detected at 285 and 364 nm [2].

These results indicates that the dissolved Fe^{3+}-urea complex slowly decomposes after heating above the temperature of approximately 50 °C enabling the desired slow release of the Fe^{3+} ions. The released Fe^{3+} ions react with water into hexaaqua ions which immediately thermally hydrolyses to form different Fe hydroxide or oxide-hydroxide phases [2]. First, the formation of γ-FeOOH is detected, whereas at the higher temperatures and/or after longer times the parallel formation of the α-FeOOH phase is observed. The observed sequence of formation of the both phases is related to the size of

the initially-formed particles, which depends on the concentration of Fe^{3+} ions released from the complex. According to the literature [43,44], the γ-FeOOH phase is more stable at smaller nanoparticles below approximately 5 nm, whereas the α-FeOOH phase becomes thermodynamically stable when the nanoparticles grow above this value [43,44].

The γ-FeOOH phase formed with the thermal hydrolysis of the Fe^{3+} ions released from the Fe^{3+}-urea complex will form spinel when it will react with precipitated Fe^{2+} ions. The complex is stable also at high pH values needed for Fe^{2+} precipitation. To obtain the spinel, the Fe^{2+} ions must precipitate with an optimal rate, just high enough to simultaneously react with the γ-FeOOH phase, preventing its transformation to unvented α-FeOOH. To achieve optimal rate of Fe^{2+} ions precipitation, the appropriate precipitation agent have to be applied.

4.1.2 Controlled release of hydroxyl ions

To achieve optimal precipitation of Fe^{2+} ions, hydroxyl ions need to be released homogeneously through the solution of the Fe precursors and in a controlled manner. That is difficult to achieve with addition of hydroxide solution. I have tested urea and $Mg(OH)_2$ as the precipitating agents, which enables controlled release of the hydroxyl ions (Table 1).

Table 1: *List of products synthesized using different precipitating agent.*

Code	Fe ions	Precipitating agent		React. Cond.		XRD	
		Type	Fe/OH	T (°C)	t_1** (min)	Phase *	Size (nm)
M60-U	Fe^{3+}-urea, Fe^{2+}	$CO(NH_2)_2$	excess	70	10	G+L	/
M60-Mg	Fe^{3+}-urea, Fe^{2+}	$Mg(OH)_2$	0.75	60	10	S	60

*S stand for spinel, G stands for goethite α-FeOOH phase and L stands for lepidocrocite γ-FeOOH
** refers to the time at final temperature after which the precipitating agent was added into Fe^{3+}-urea/Fe^{2+} ions solution

First, the Fe^{3+}-urea /Fe^{2+} solution was maintained at the final temperature for 10 minutes giving rise for the formation of initial γ-FeOOH product with thermal hydrolysis. To promote its transformation to the γ-Fe_2O_3 phase during the precipitation of Fe^{2+}, precipitation agent was added. First, urea was tested as the precipitating agent. Urea was dissolved into the Fe^{3+}-urea /Fe^{2+} solution after it remained at the final temperature of 70 °C for 10 min. The increase of temperature caused slow decomposition of urea resulting in gradual release of the ammonium hydroxide. The release of the hydroxide caused increase in pH shown in pH vs. time plot of Figure 18 (sample M60-U). The slow increase in pH indicates the slow release of the hydroxide ions and their almost simultaneous consumption by chemical reactions. Additionally, the ammonia formed is rinsed from the reaction mixture with bubbling Ar.

Only after approximately 1 hour, the pH increased to the value of 6.2 required for Fe^{2+} precipitation, whereas in a next 1 hour final pH of 6.5 was reached. The XRD pattern of the sample M60-U (not shown) showed very poor crystallinity with few small peaks that

correspond to the orthorhombic α-FeOOH structure. The presence of needle-like crystals of α-FeOOH was also revealed by TEM analysis of the sample (Figure 19). The formation of α-FeOOH phase indicates that the release of hydroxide ions from decomposed urea and consequently the precipitation of Fe^{2+} were too slow. The long time at the high temperature and pH below 6.2 resulted in growth of initially formed γ-FeOOH, which most probably resulted in its transformation into the α-FeOOH. It is known that at increased particles size transformation to α-FeOOH is favored due to the thermodynamic factors like enthalpy of formation and surface enthalpy of hydration in dependence of the surface area [43, 44]. Moreover, during the decomposition of urea besides ammonia also CO_2 is formed. It is known that CO_2 favors the formation of α-FeOOH [45]. Formed α-FeOOH is stable and does not further transform into spinel. The release of hydroxyl ions would be faster at the higher temperatures that would result in faster decomposition of urea. However, the application of the higher temperature is not desired since it would also results in the increased rate of the Fe^{3+}-urea complex decomposition.

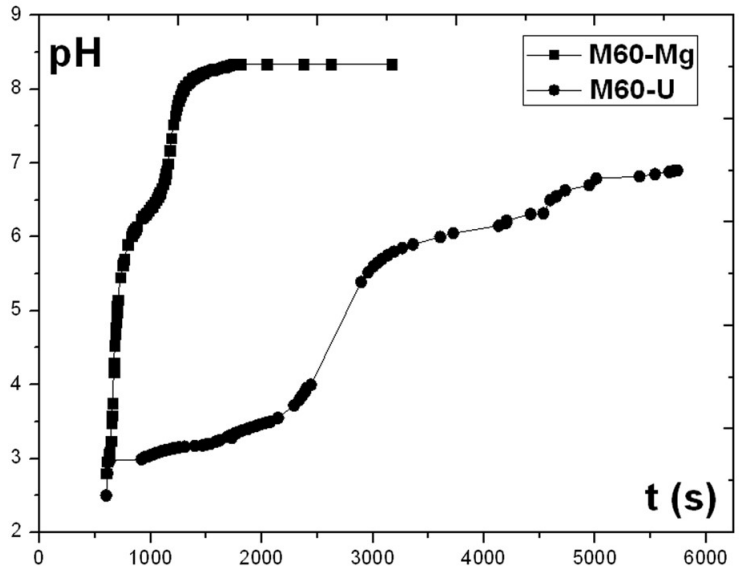

Figure 18: *pH vs. time curves for samples M60-0 and M60-U.*

To increase the rate of the hydroxyl ions release while still retaining homogeneity through the reaction vessel, $Mg(OH)_2$ was tested. Solid $Mg(OH)_2$ was admixed into the Fe^{3+}-urea /Fe^{2+} solution after it was maintained at temperature of 60 °C for 10 min. The solubility of $Mg(OH)_2$ is low and increases with the temperature [46]. Due to its relatively low solubility, hydroxyl ions are slowly and homogeneously released. The pH value of 6.2 needed for the precipitation of Fe^{2+} was reached in approximately 15 min, while final pH of 8.2 was reached after 0.5 hour (Figure 18).

The XRD pattern of the product M60-Mg is shown in Figure 22. The diffraction peaks match to those for cubic spinel structure, while from the line broadening the average particles size was estimated to be around 60 nm.

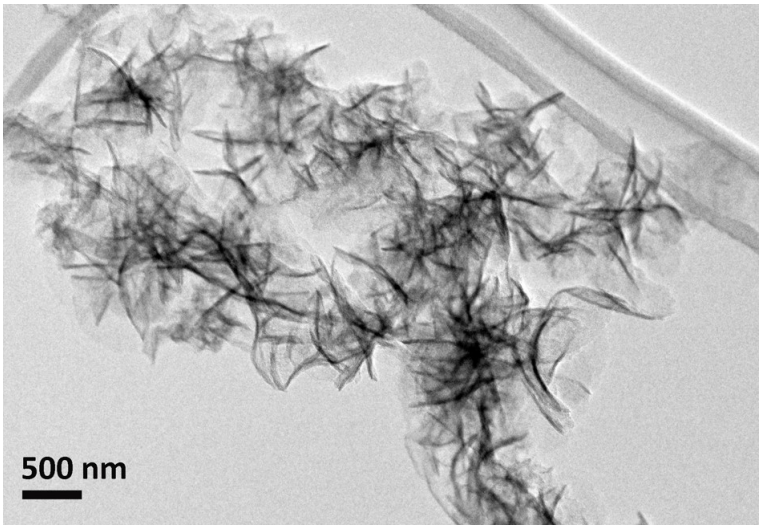

Figure 19: *TEM image of M60-U.*

The M60-Mg product was also evaluated with TEM analysis. The TEM image in Figure 20 shows particles with bimodal size distribution. Besides small nanoparticles of only approximately 20 nm, also larger, octahedrally-shaped nanoparticles of the size up to 100 nm are present.

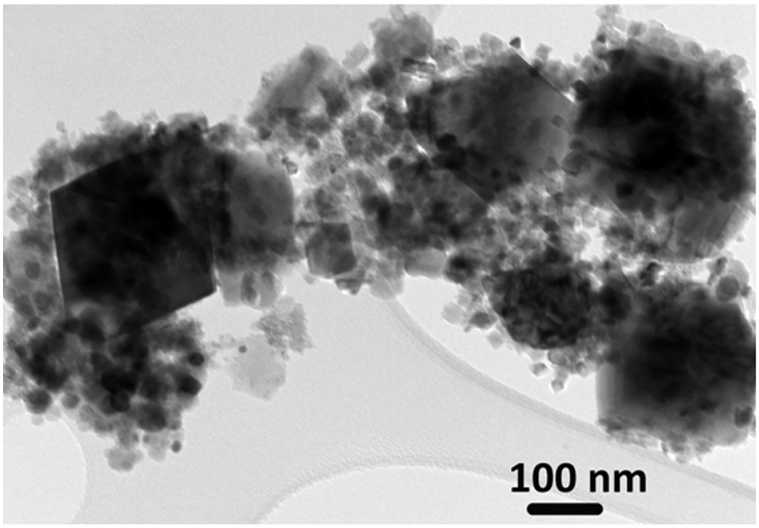

Figure 20: *TEM image of iron-oxide particles M60-Mg, synthesized with the additions of $Mg(OH)_2$ into the Fe precursors solution at temperature of 60 °C.*

Slow and homogeneous release of hydroxyl ions achieved by the addition of solid $Mg(OH)_2$ resulted in precipitation of the Fe^{2+} ions that caused transformation of γ-FeOOH, previously formed by the thermal hydrolysis of the Fe^{3+} released from the Fe^{3+}-urea complex, into spinel as the only product. $Mg(OH)_2$ appeared as the most promising precipitating agent enabling controlled and at the same time homogeneous release of hydroxyl ions.

The release of hydroxyl ions from $Mg(OH)_2$ depends also on the temperature. With increasing temperature the solubility of $Mg(OH)_2$ increases, which results in the faster

release of hydroxyl ions. To examine the effect of temperature on the solubility of $Mg(OH)_2$ and thus the control of hydroxyl-ions release, three different reaction temperatures: 50, 60 and 70 °C were tested.

However, the temperature apart from $Mg(OH)_2$ solubility influences also the rate of the Fe^{3+}-urea complex decomposition and thermal hydrolysis of the released Fe^{3+} ions. The Fe^{3+}-urea complex starts to decompose at the temperature around 50 °C, which results in gradual release of Fe^{3+} ions. Thermal hydrolysis starts to proceeds around 55 °C [47–50] and is more pronounced as the temperature increases and/or at the prolonged temperature exposure.

Thus, to evaluate the effect of the reaction temperature on the release of the hydroxyl ions, the $Mg(OH)_2$ was admixed into the solution of the Fe precursors, which was maintained at selected temperature (50, 60, or 70 °C) for different periods of time (denoted as t_1 in Table 2). At t_1 =0, $Mg(OH)_2$ was admixed into heated degassed water together with Fe precursors. Most likely, under such conditions, the effect of thermal hydrolysis will be less pronounced. However, at t_1 =10 or 60 min, expected formation of different products (α-FeOOH, γ-FeOOH) proceed first while subsequent addition of $Mg(OH)_2$ after elapsing t_1 gave rise to the precipitation of Fe^{2+} and results in the formation of final oxide.

Table 2: *List of products synthesized at different temperatures*.

Code	Fe ions	$Mg(OH)_2$	React. Cond.		XRD	
		Fe/OH	T (°C)	t_1** (min)	Phase *	Size (nm)
M50-Mg_0	Fe^{3+}-urea, Fe^{2+}	0.75	50	0	S	22
M50-Mg_{10}	Fe^{3+}-urea, Fe^{2+}	0.75	50	10	S	20
M60-Mg_0	Fe^{3+}-urea, Fe^{2+}	0.75	60	0	S	33
M60-Mg	Fe^{3+}-urea, Fe^{2+}	0.75	60	10	S	60
M60-Mg_{60}	Fe^{3+}-urea, Fe^{2+}	0.75	60	60	S+H+G	45
M70-Mg_0	Fe^{3+}-urea, Fe^{2+}	0.75	70	0	S	28
M70-Mg_{10}	Fe^{3+}-urea, Fe^{2+}	0.75	70	10	S	54

*S stand for spinel, G stands for goethite α-FeOOH phase and H stands for hematite α-Fe_2O_3

** refers to the time at final temperature after which the precipitating agent was added into Fe^{3+}-urea/Fe^{2+} ions solution

Figure 21 shows pH vs. time curves for the samples synthesized after $Mg(OH)_2$ was admixed together with the Fe precursors solution heated to 60 °C (M60-Mg_0), or only after the Fe precursors solution was maintained at 60 °C for 10 min (M60-Mg). After immediate addition of $Mg(OH)_2$, rapid increase of hydroxyl ions concentration was observed for the sample M60-Mg_0. The pH value required for the Fe^{2+} precipitation (6.2) was reached in less than 3 min, while after only 10 min final pH of 8 was reached. Conversely, the addition of $Mg(OH)_2$ with delay of 10 minutes in the sample M60-Mg resulted in reduced slope of the pH vs. time curve. The pH required for Fe^{2+} precipitation was reached only after 20 min, while final pH of 6.5 was reached in 1 hour.

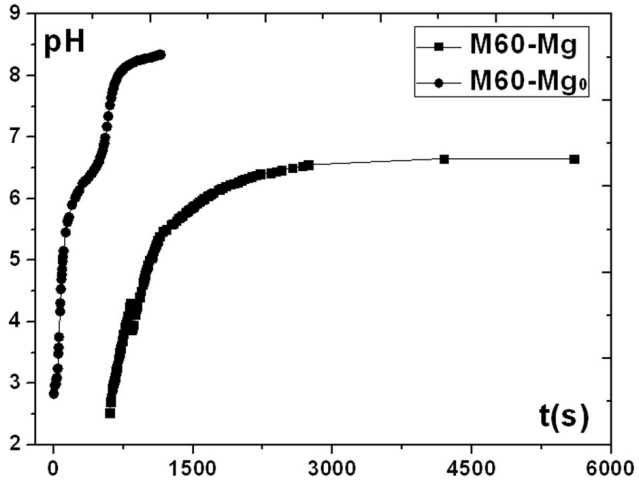

Figure 21: *pH vs. time curve for samples M60-Mg0 and M60-Mg.*

Figure 22 shows XRD patterns of the products M60-Mg$_0$ M60-Mg and M60-Mg$_{60}$. The latter was synthesized when Mg(OH)$_2$ was admixed after the Fe precursor solution was maintained at temperature of 60 °C for 60 min.

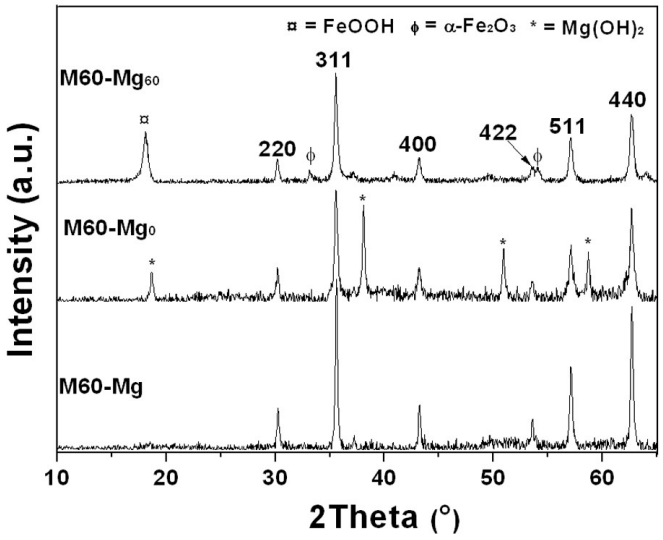

Figure 22: *XRD pattern for samples M60-Mg, M60-Mg0 and M60-Mg60.*

The XRD pattern of all three samples reveals narrow peaks indicating the formation of well crystalline products. In the XRD pattern of M60-Mg$_0$ and M60-Mg, all peaks of the products present can be indexed according to cubic spinel structure (additional peaks in the pattern of M60-Mg$_0$ can be indexed according to an orthorhombic structure of Mg(OH)$_2$). The XRD patterns M60-Mg$_{60}$, however, apart from cubic spinel show presence of α-FeOOH phase and small content of hexagonal hematite (α-Fe$_2$O$_3$). From the line broadening of all three samples, significant differences in the particles size of the formed spinel were observed. The average particles size in the sample M60-Mg$_0$ yields around 33 nm and it increase significantly for M60-Mg, yielding 60 nm. The particles size of M60-Mg$_{60}$, slightly decreased compared to M60-Mg, to average value of 45 nm.

At 60 °C the release of hydroxyl ions proceeds with the same rate in all three samples

however, pH vs. time curve suggests that its consumption for Fe^{2+}/Fe^{3+} precipitation varied in dependence of the free Fe^{3+}. When $Mg(OH)_2$ was admixed together with the Fe precursors (M60-Mg_0), a limited concentration of free Fe^{3+} together with Fe^{2+} was available for the precipitation, which gave rise to the large increase of the hydroxyl ions through the volume of the reaction mixture resulting in the rapid increase of the measured pH.

However, when $Mg(OH)_2$ was admixed after elapsing t_1 (10 or 60 min), the formation of the γ-FeOOH product caused by the thermal hydrolysis of Fe^{3+} ions proceeded first. When concentration of hydroxyl ions gradually increased due to the addition of $Mg(OH)_2$ the precipitated Fe^{2+} reacted with γ-FeOOH resulting in the γ-FeOOH-to-spinel transformation. Most likely, the remained Fe-precursors were consumed for the growth of the formed spinel nanoparticles.

The parallel formation of the secondary phases α-FeOOH and α-Fe_2O_3 in the sample M60-Mg_{60} suggests the increased particles size of the γ-FeOOH formed by thermal hydrolysis due to larger concentration of free Fe^{3+} ions. Increased particles size resulted in partial transformation of the initial γ-FeOOH to the α-FeOOH phase that is favored at increased size due to the thermodynamic factors [51,52]. Since Fe^{3+} ions were partially consumed for the formation and growth of α-FeOOH, reduced amount of the Fe precursor left was available for spinel growth thus resulting in slightly decreased particles size. α-Fe_2O_3 detected in the final product resulted as a partial dehydration of α-FeOOH [41].

When the synthesis proceeds at higher temperature of 70 °C the results were similar to that described for 60 °C. First, the solution of the Fe precursors was maintained at 70°C for different periods (denoted as t_1 in Table 2). In dependence on the concentration of free Fe^{3+} ions released from the decomposed Fe^{3+}-urea complex, differently pronounced thermal hydrolysis can result in the formation of γ-FeOOH phase. After elapsing t_1 $Mg(OH)_2$ was admixed into the solution, giving rise to the precipitation resulting in the formation of final oxide nanoparticles.

Dissolving $Mg(OH)_2$ in the reaction mixture resulted in gradual increase in the concentration of the hydroxyl ions observed on pH vs. time curve (Figure 23). The curve plot is very step for M70-Mg_0, reaching final pH of 8 in a less than 7 min, while curve plot for sample M70-Mg_{10} shows a reduced slope, since pH required for Fe^{2+} precipitation was reached only after 20 min, whereas pH of 6.8 was reached in approximately 1 hour. However, final pH measured in either case was slightly higher to that observed when the synthesis proceeded at 60 °C, which can be attributed to the increased solubility of $Mg(OH)_2$ with increasing temperature, and thus faster release of hydroxyl ions.

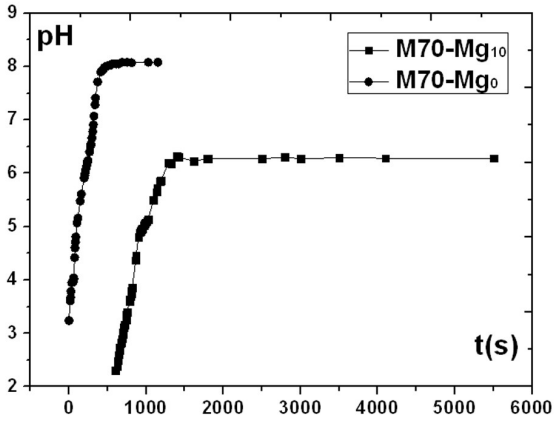

Figure 23: *pH vs. time curve for samples M70-Mg_0 and M70-Mg_{10}.*

XRD analysis (not shown) of sample M70-Mg_0 and M70-Mg_{10} showed the presence of single spinel phase with the particles size of 28 and 54 nm, for samples M70-Mg_0 and M70-Mg_{10}, respectively. Although similar behaviour to that with samples synthesized at 60 °C was observed, the size of the final spinel nanoparticles slightly decreased. This can be related to the increased solubility of $Mg(OH)_2$ at the higher temperature, which resulted in faster release of the hydroxyl ions causing an increased supersaturation.

Finally, the synthesis at temperatures of 50 °C was tested. The addition of $Mg(OH)_2$ resulted in the gradual increase of the hydroxyl ions (ph vs. time curve, Figure 24). The curves for the samples M50-Mg_{10} and M50-Mg_0 reveal similar rate of hydroxyl ions increase, since in either case pH required for Fe^{2+} ions precipitation was reached after 8 min. Further, final pH of 8.5 for the sample M50-Mg_0 was reached after 40 min, while for the sample M50-Mg_{10} pH of 8.5 was reached only after 1.5 h.

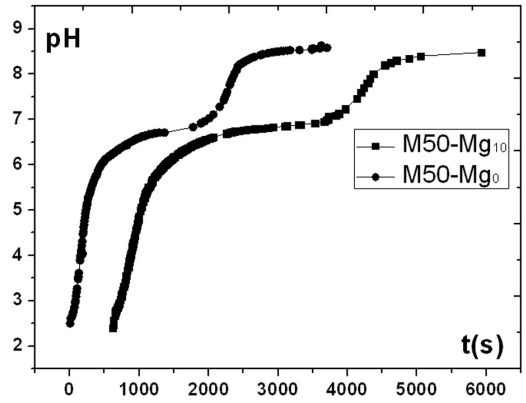

Figure 24: *pH vs. time curve for samples M50-Mg_0 and M50-Mg_{10}.*

Figure 25 shows XRD patterns of samples M50-Mg_0 and M50-Mg_{10}. The XRD patterns of both samples show presence of broader peaks that can be indexed according to cubic spinel structure.

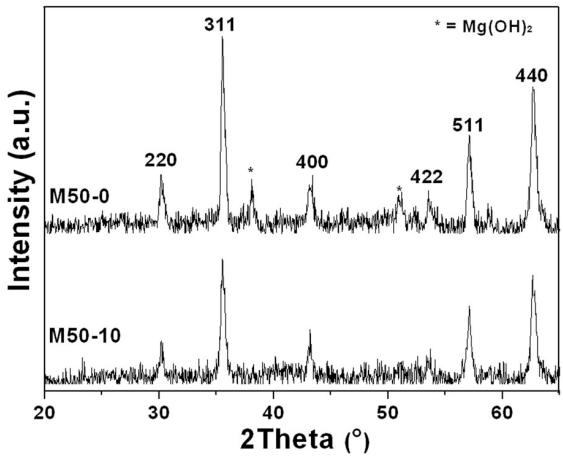

Figure 25: *XRD pattern for sample M50-Mg_0 and M50-Mg_{10}.*

The average particles size determined from line broadening yields 23 and 24 nm for

samples M50-Mg_0 and M50-Mg_{10}, respectively. Almost the same average particles size determine in the both cases suggests that the temperature treatment of the Fe precursors solution at the temperature of 50 °C before the addition of $Mg(OH)_2$, has no significant effect on the course of reaction, suggesting less pronounced or even absent process of the thermal hydrolysis.

These presented results demonstrate the temperature dependence of $Mg(OH)_2$ solubility and thus the rate of hydroxyl ions release on the course of the precipitation reactions. Additionally, temperature dependence of Fe^{3+}-urea complex decomposition and extend of the thermal hydrolysis are also important.

The lowest solubility of $Mg(OH)_2$ and thus slowest release of hydroxyl ions at the temperature of 50 °C would otherwise enable better control of hydroxyl ions release. However, at this temperature, the rate of decomposition of Fe^{3+}-urea is low, whereas the absence of the thermal hydrolysis at 50 °C hinders the formation of γ-FeOOH product. Similar results were obtained when reaction proceeded at higher temperature, but at conditions where γ-FeOOH wasn't formed before the addition of $Mg(OH)_2$ (M60-Mg_0 and M70-Mg_0).

Only when reaction proceeds at temperatures of 60 and 70 °C and $Mg(OH)_2$ was admixed after the Fe precursor was maintained at the final temperature for 10 min, the conditions seem optimal for coating of the spinel to the core nanoparticles. In either case the thermal treatment of the Fe precursors solution before $Mg(OH)_2$ addition resulted in the formation of γ-FeOOH. The subsequent gradual increase of the hydroxyl ions initiated the precipitation of Fe^{2+} that resulted in the transformation of γ-FeOOH to spinel. In the either case, the unreacted Fe precursors were most likely preferentially consumed for the growth of the spinel nanoparticles. However, the use of lower temperature would still enable better control of the hydroxyl ions release, so for the further studies, reaction temperature of 60 °C was selected.

4.2 Core nanoparticles

For heterogeneous nucleation of spinel on the surface of selected core nanoparticles, the supersaturation of the nucleating phase needs to be closely controlled. However, also the core nanoparticles can influence the nucleation kinetics with its structure, size and morphology. At different supersaturation of the nucleating phase, these effects are differently pronounced [27]. To examine the effect of core nanoparticles crystal structure, size and morphology different core nanoparticles, amorphous silica (SiO_2) nanoparticles and crystalline Ba hexaferrite nanoparticles ($BaFe_{12}O_{19}$, later referred to as BaM) of different size and morphology were used. Additionally, to synthesize uniform layers of spinel on the surfaces of the core nanoparticles, it was crucial to achieve the colloidal stability of core nanoparticles in water.

4.2.1 Silica (SiO_2) core nanoparticles

First, aqueous suspension of amorphous silica nanoparticles was prepared and examined with TEM and ζ-potential measurements. Figure 26a presents a TEM image of the amorphous silica core nanoparticles (SiO_2). The specimen was prepared by drying stable

aqueous suspension on a specimen support. From the TEM image it is evident that the sample consists of agglomerated globular particles with a broad size distribution. While majority of the core nanoparticles is of the size between 20–30 nm, also larger 50 nm nanoparticles are present. From electro-kinetic measurement it was determined that silica nanoparticles exhibited a large negative ζ-potential enabling their colloidal stability over large pH region (Figure 26b). To obtain the silica nanoparticles with opposite, positive surface charge, the silica nanoparticles were pre-treated with hydrolyzed APS (sample APS-SiO_2). The APS grafted onto the nanoparticles surfaces enabled the high positive zeta potential with its protonated amino groups, thus enabling the colloidal stability of the nanoparticles' suspension (Figure 26b).

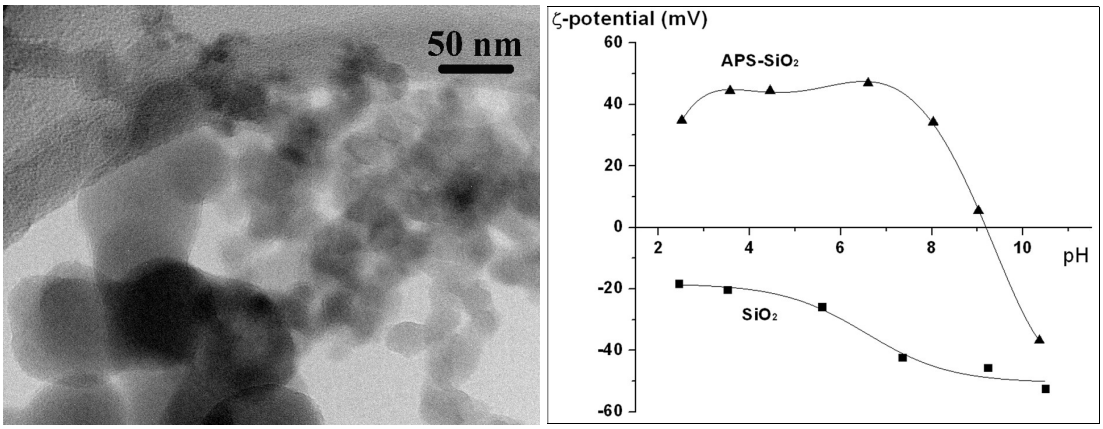

Figure 26: *TEM image of dried suspension of SiO_2 nanoparticles revealing bimodal size distribution (a), and ζ-potential measurements of the stable silica core nanoparticles' suspension (SiO_2) and the silica nanoparticles functionalized with hydrolyzed aminopropyl silane (APS-SiO_2) (b).*

4.2.2 Ba hexaferrite (BaM) core nanoparticles

The Ba-hexaferrites core nanoparticles of different size and morphology were synthesized with hydrothermal synthesis. Figure 27a presents Ba-hexaferrite nanoparticles hydrothermally synthesized at temperature of 150 °C ($BaM_{10\text{-}70}$). The TEM image reveals that the synthesized product consists of the nanoparticles with bimodal size distribution. While the majority of the nanoparticles are in the form of small discoids with equivalent diameter of 10 nm and thickness of only approximately three nanometeres, also large platelet crystal with the size of up to 100 nm are visible. The nanoparticles were stabilized in water with its high positive zeta potential at pH of 4 - 5 (Figure 28). High positive ζ-potential in the acidic media also enabled the stabilization of $BaM_{30\text{-}70}$ nanoparticles. TEM image of $BaM_{30\text{-}70}$ core nanoparticles (Figure 27b) reveals the presence of larger platelet crystal of diameter between 30–70 nm, and thickness of approximately 5 nm [53].

The Ba-hexaferrite nanoparticles were synthesized also in the presence of oleic acid. Oleic acid absorbs onto the nanoparticles surfaces and thus blocks their exaggerated growth during hydrothermal synthesis. The oleic acid also enables colloidal stability of the nanoparticles in non-polar liquids. Using addition of oleic acid, the nanoparticles with narrower size distribution were synthesized. Since the spinel synthesis in a subsequent procedure takes place in aqueous solution, the oleic acid was replaced with citric acid in a ligand-exchange reaction. The citric acid adsorbed on the nanoparticles surfaces enabled

high negative ζ-potential and thus the colloidal stability of the core nanoparticles in water (sample BaM_{10}, Figure 27). Figure 27c shows the TEM image of the Ba-hexaferrite discoid nanoparticles synthesized at 240 °C (BaM_{10}). The equivalent diameter yields around 10 nm, while their thickness was around 3 nm. Figure 27d shows a HREM image of the discoid particles oriented edge-on along [0001] direction of the hexagonal structure. The measured distance between lattice fringes yields approximately 1.15 nm corresponding to (0002) planes of the structure. When the addition of oleic acid was used and the temperature of hydrothermal synthesis was increased to 270 °C, the nanoparticles BaM_{100} in the form of larger hexagonal platelet crystals of the equivalent diameter of around 100 nm and average thickness of 8 nm were obtained (Figure 27e). Figure 14f shows TEM image of the platelet Ba hexaferrite crystal oriented edge-on. Form the TEM image it is evident that the lattice image is terminated on the surface of the particle, revealing the absence of surface amorphous layer. The measured distance between lattice fringes yields around 1.15 nm and corresponds to the distance between the (0002) planes of the hexagonal structure.

The differences in Ba-hexaferrites nanoparticles' size reflects also in their magnetic properties (Table 3). The magnetization (measured at 1T) increases with the increasing size. For the sample BaM_{100} consisting of only large platelet crystal it yields around 34.5 Am^2/Kg. With decreasing particles size (BaM_{30-70}) it decreases to 27 Am^2/kg, whereas in the sample BaM_{10-70} it decreases to only 5 Am^2/kg. The lower magnetization detected in the sample consisting of the smaller Ba hexaferrite core nanoparticles is a consequence of the increase in the relative surface area and the decrease in their magnetic ordering. Finally, for the sample BaM_{10} consisting of only the 10 nm-sized nanoparticles, the magnetization decreases to only 1.5 Am^2/kg [37, 39]. Low remanent magnetization for the BaM_{10} and the BaM_{10-70} nanoparticles indicates that the majority of the Ba-hexaferrite nanoparticles is in or close to the superparamagnetic state. At increased size of the Ba hexaferrite core nanoparticles (BaM_{30-70} and BaM_{100}) higher remanent magnetization indicates the presence of the mono-domain ferromagnetic particles.

Table 3: *List of SiO_2 and BaM core nanoparticles with their properties.*

Code	Type		Size (nm)	Colloidal stability	Magnetic properties		
				ζ-potential	M (Am^2/kg)**	M_R (Am^2/kg)	H_c (4π kA/m)
SiO_2	SiO_2	amorphous	20–50	- charge	/	/	/
APS-SiO_2	SiO_2	amorphous	20–50	+ charge	/	/	/
BaM_{10}	$BaFe_{12}O_{19}$	crystalline	~ 10	- charge (CA)	2.5	0.3	30
BaM_{10-70}	$BaFe_{12}O_{19}$	crystalline	10–70	+ charge	7.1	2.6	390
BaM_{30-70}	$BaFe_{12}O_{19}$	crystalline	30–70	+ charge	27	13	1700
BaM_{100}	$BaFe_{12}O_{19}$	crystalline	~ 100	- charge (CA)	34.5	17.8	2550

* CA stands for citric acid

** corresponds to the magnetization measured at 1T

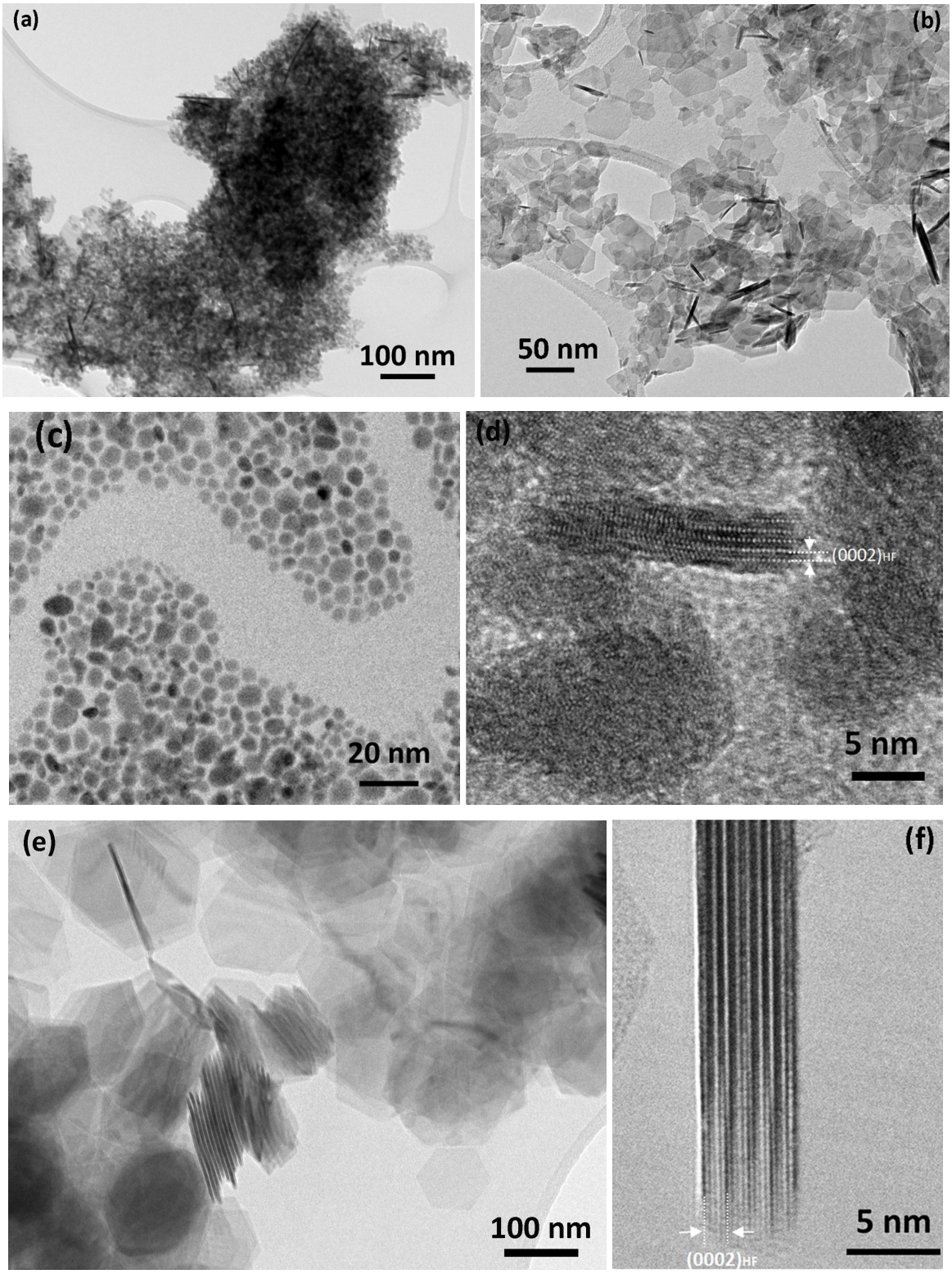

Figure 27: *TEM images of the Ba-hexaferrite core nanoparticles, with different size and morphology: (a) mixture of small discoid and larger platelet crystals with average size between 10–70 nm (BaM_{10-70}), (b) the platelet crystals of the size between 30–70 nm, (c) the Ba-hexaferrite discoid nanoparticles with diameter of 10 nm and thickness of approximately 3 nm (BaM_{10}), (d) HREM pattern of the discoid Ba-hexaferrite nanoparticle BaM_{10} oriented edge-on, (e) hexagonal platelet crystals with average diameter of ~ 100 nm and thickness of 5 nm (BaM_{100}) and (f) TEM image of Ba hexaferrite platelet crystal oriented edge-on with its large surfaces parallel to the*

electron beam.

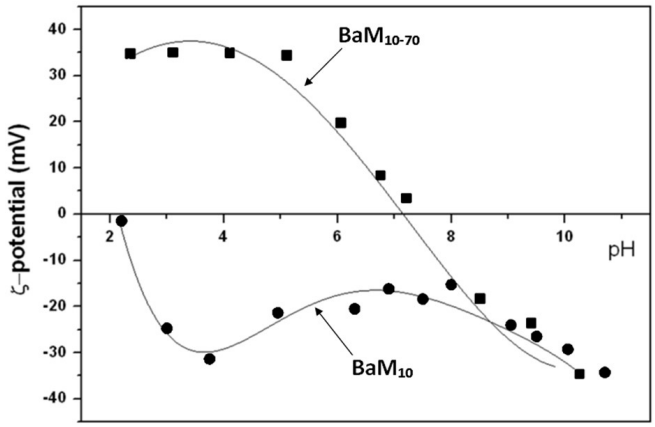

Figure 28: *ζ-potential measurement or the stable aqueous suspension of BaM_{10-70} and BaM_{10}.*

4.3 Synthesis of the spinel with heterogeneous nucleation

Further syntheses were subjected to study the coating of spinel on the surfaces of appropriate core nanoparticles. The synthesis of spinel proceeded in stable aqueous suspensions of the core nanoparticles (silica or Ba-hexaferrite core nanoparticles). As I state before the coating of the spinel phase can be achieved when the initial product nucleates heterogeneously. After subsequent chemical reaction the initial product transforms into final spinel phase, which remains on the core surfaces as coating. Heterogeneous nucleation of the initial product can be achieved under conditions of low supersaturation. Results described in section 4.1 showed that controlled release of Fe^{3+} and hydroxyl ions, required for close control of supersaturation of initial product can be achieved with immobilization of Fe^{3+} into complex and use of $Mg(OH)_2$ as a precipitating agent. The subsequently precipitated Fe^{2+} ions after react with γ-FeOOH phase that forms with thermal hydrolysis, resulting in the formation of spinel as the single phase.

4.3.1 S@SiO_2 nanocomposite particles

To obtain heterogeneous nucleation of spinel on the surface of the silica nanoparticles, the Fe precursors, i.e., an aqueous solution of a Fe^{3+}-urea complex and Fe^{2+} ions, were dissolved into silica suspension heated to 60 °C, under argon bubbling. After the suspension remained at the initial pH of 2.2 for 10 min (defined as Stage 1) the $Mg(OH)_2$ was admixed. The additions of $Mg(OH)_2$ resulted in gradual increase of pH (Figure 28). After approximately 25 min, the pH required for the precipitation of Fe^{2+} was obtained (Stage 2, Figure 28), while in another 30 min, final pH of 6.8 was reached. After the reaction mixture maintained at final pH for 1.5 hour (Stage 3, Figure 28), the reaction was stopped and the final product (S@SiO_2-10) was collected and examined with TEM.

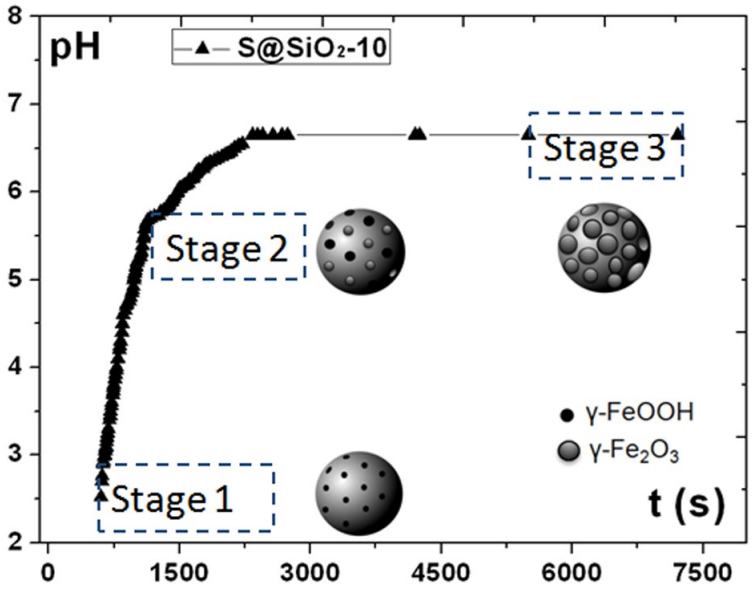

Figure 28: *pH vs. time curve measured during the synthesis of S@SiO_2-10.*

Figure 29a shows a representative TEM image of the sample S@SiO_2-10. The TEM image reveals the presence of larger amorphous silica core nanoparticles of the size between 20–50 nm, covered with small round-shape nanoparticles in a relatively high surface concentration. Detailed TEM analysis reveals that the small nanoparticles are of average size between 5–7 nm and positioned exclusively on the surfaces of the silica core nanoparticles, while no homogeneously nucleated nanoparticles were detected. Obviously the established reaction conditions favored heterogeneous nucleation.

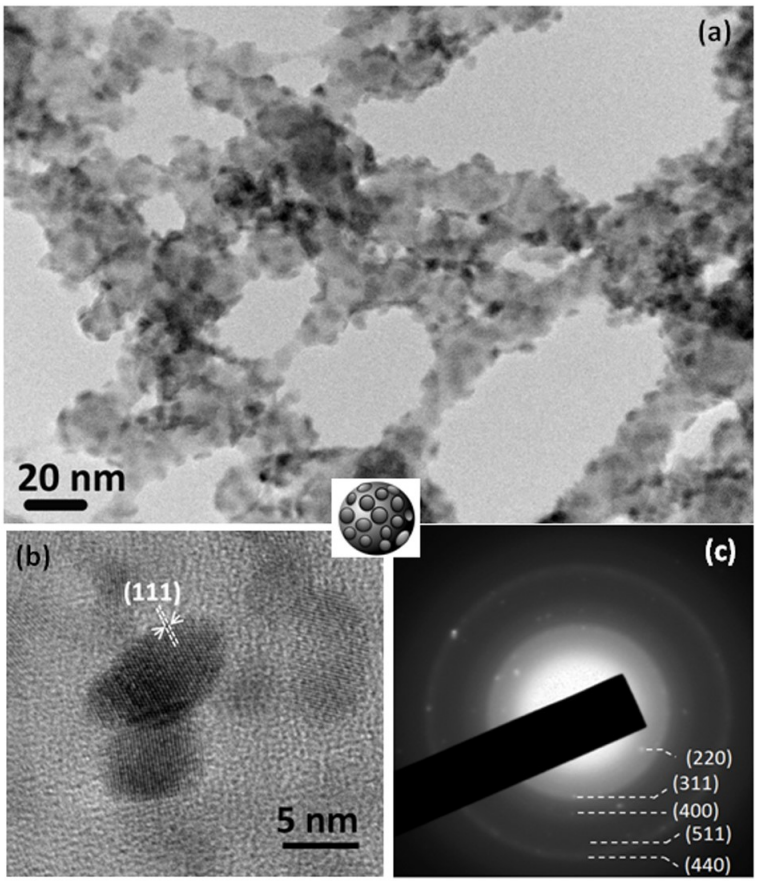

Figure 29: *Representative TEM image of the product S@SiO2-10 (a), the HREM image of the spinel nanoparticles on the surfaces of the silica core nanoparticle (b), and the electron diffraction pattern recorded from a large area of the material (c).*

The electron diffraction pattern, taken from a large area reveals apart from broad diffuse ring of the amorphous silica, also sharper rings and spots that correspond to a cubic spinel structure. Taking into consideration the experimental conditions and inert reaction atmosphere most likely the first spinel phase formed is cubic spinel magnetite (Fe_3O_4). However, the magnetite is prone to oxidize into cubic spinel maghemite (γ-Fe_2O_3). Most likely the final phase was maghemite because of complete oxidation of the relatively small nanoparticles.

HREM analysis (inset in Figure 29b) confirms that the nanoparticles are crystalline and oriented in different crystallographic directions. The lattice fringes in the HREM pattern of the largest nanoparticle show periodicity of 4.8 nm, corresponding to the distance between (111) planes of the spinel structure. Additionally, EDS spectra recorded over the larger area of the material confirms the formation of the Fe-rich phase.

4.3.2 Reaction mechanism

To obtain further insight into reaction mechanism that governs the formation of iron oxides, during the early stages of the reaction, intermediate products corresponding to the Stage 1 and Stage 2 (Figure 29) were collected and examined using TEM.

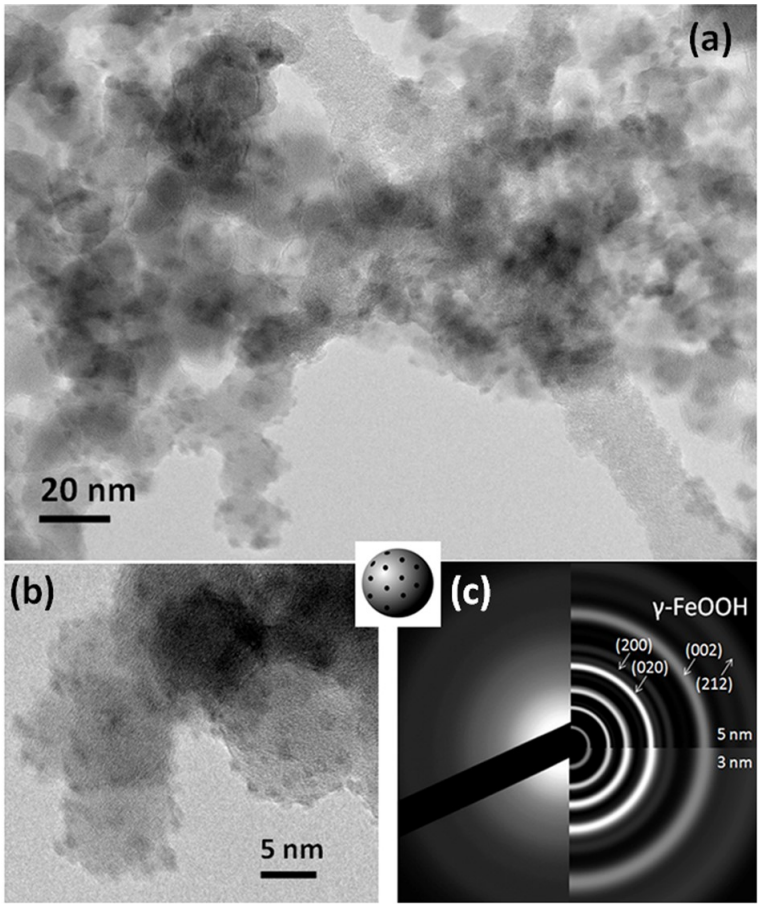

Figure 30: *Representative TEM image of S@SiO$_2$-10 sample collected after Stage 1 (a), TEM image the sample at higher magnification (b), electron diffraction pattern recorded from the larger area of the material (left) is compared to the calculated patterns for 3 (right down) and 5 nm (right top) nanoparticles with structure of γ-FeOOH (c).*

Figure 30a represents TEM image of the intermediate product sampled after reaction mixture was maintained at final temperature for 10 minutes, before the addition of $Mg(OH)_2$. The representative TEM image shows that the surfaces of the silica spheres are covered with small nanoparticles in low surface concentration, while no homogeneously nucleated nanoparticles were detected. The detailed TEM investigation (Figure 30b) reveals that nanoparticles are arranged at approximately equal distance apart while their size was estimated to be around 3 nm. The nanoparticles exhibit poor crystalline order, which reflects also from the electron diffraction pattern that was taken over larger area of the sample (Figure 30c, left). The diffraction pattern shows prevailing diffuse rings of amorphous silica and week reflection rings. The diffraction pattern was compared with diffraction patterns calculated for different Fe-oxide-hydroxide phases (α-FeOOH, γ-FeOOH), formation of which is consistent with expected hydrolysis of Fe^{3+} ions in acidic medium [43, 44]. The recorded diffraction pattern matched with the one calculated for the orthorhombic phase of γ-FeOOH. In Figure 30c the diffraction patterns calculated for the nanoparticles of the γ-FeOOH structure with the size of 5 nm (top right) and 3 nm (right down) is shown. The comparison of both, the recorded and the calculated electron diffraction patterns reveals that week rings observed in the experimental pattern can be ascribed to (200) and (002) planes of γ-FeOOH phase. The formation of γ-FeOOH phase is consistent with the thermal hydrolysis of Fe^{3+} ions [43, 44].

As reaction further proceeded the addition of $Mg(OH)_2$ gave rise to the increase in pH,

resulting in the precipitation of Fe^{2+} ions. The intermediate product was sampled at the end of Stage 2 and examined with TEM. Figure 31a shows representative TEM image revealing that after the addition of $Mg(OH)_2$ the size of the nanoparticles on the silica spheres increased, however, the nanoparticles are still arranged at approximately equal distance apart. Detailed TEM examination revealed the absence of any homogeneously nucleated nanoparticles.

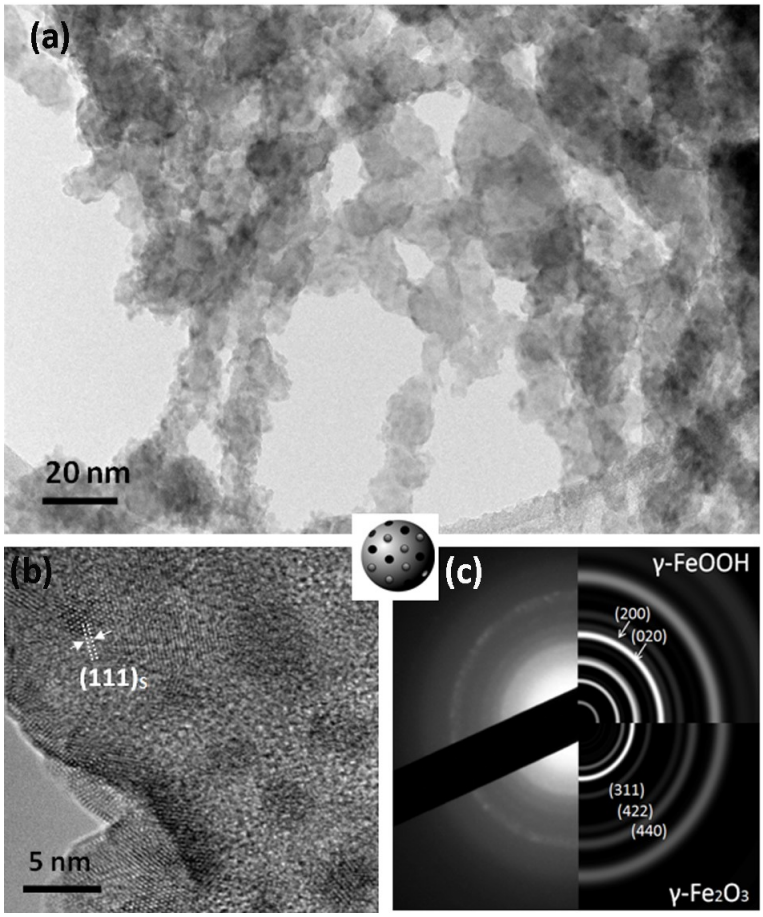

Figure 31: *Representative TEM image of sample S@SiO₂-10 sampled after Stage 2 (a), HREM image of selected area revealing the increased particles size and improved crystalline order (b) electron diffraction recorded over large area of the material (left) and simulated electron diffraction for 5 nm orthorhombic γ-FeOOH phase (top) and cubic spinel phase (down).*

Detailed HREM analysis revealed the increase in the nanoparticles' size from 3 to 5 nm and also improved crystalline order (Figure 31b). The lattice image of the nanoparticle marked in the image reveals that the periodicity of the lattice fringes corresponds to the distance between (111) planes of the cubic spinel structure. However, the electron diffraction pattern shown in Figure 31c that was recorded from the larger area of the sample revealed the reflection rings that can be ascribed to more than one phase. The recorded electron diffraction in Figure 31c is compared to calculated ones for 5 nm nanoparticles of the cubic spinel structure (down right) and the 5 nm nanoparticles of the orthorhombic γ-FeOOH structure (top right). The comparison between recorded and both calculated diffractions reveals matching with the both structures; cubic spinel structure and orthorhombic structure of γ-FeOOH.

Finally, after prolonging the reaction the analysis of final product $S@SiO_2$-10 showed

complete transformation of the formed nanoparticles into the spinel structure, together with their increase in size, as shown in Figure 29.

As predicted, the final spinel product was obtained on the surfaces of the core nanoparticles as a consequence of the heterogeneous nucleation of the initial product and its further transformation into the final spinel structure. For the product S@SiO_2-10, the examination of the intermediate product of the Stage 1 revealed that already after thermal hydrolysis of the Fe precursors, the heterogeneous nucleation of γ-FeOOH phase on the surfaces of the core nanoparticles occurs. After addition of $Mg(OH)_2$, the precipitation of Fe^{2+} gave rise to the γ-FeOOH-to-spinel transformation, while the remained Fe-precursors were consumed for the growth of the formed spinel nanoparticles.

Additional studies were performed to exclude the possibility that the nanoparticles would form homogeneously in the suspension and subsequently adhere to the silica surfaces only due to the electrostatic attractions. Typically, the iron oxides in aqueous solution exhibit positive ζ-potential in acidic medium, negative in basic and isoelectric point at pH around 7.5, whereas the colloidal suspension of the silica core nanoparticle used in above described experiment exhibited high negative ζ-potential through a wide pH region (Figure 26b). In the pH region where reaction proceeds (pH = 2–7), the spinel iron oxide and the silica core nanoparticles are oppositely charged. To exclude the possibility that the iron-oxide would form with homogeneous nucleation and only subsequently electrostatically adhere to the core nanoparticles, additional experiment were performed. In these experiments the synthesis preceded under the same reaction conditions as described above, however, in the suspension of positively charged silica core nanoparticles APS-SiO_2. The protonated amino groups of the surface APS molecules enabled high positive ζ-potential of the core nanoparticles, as shown in Figure 26b.

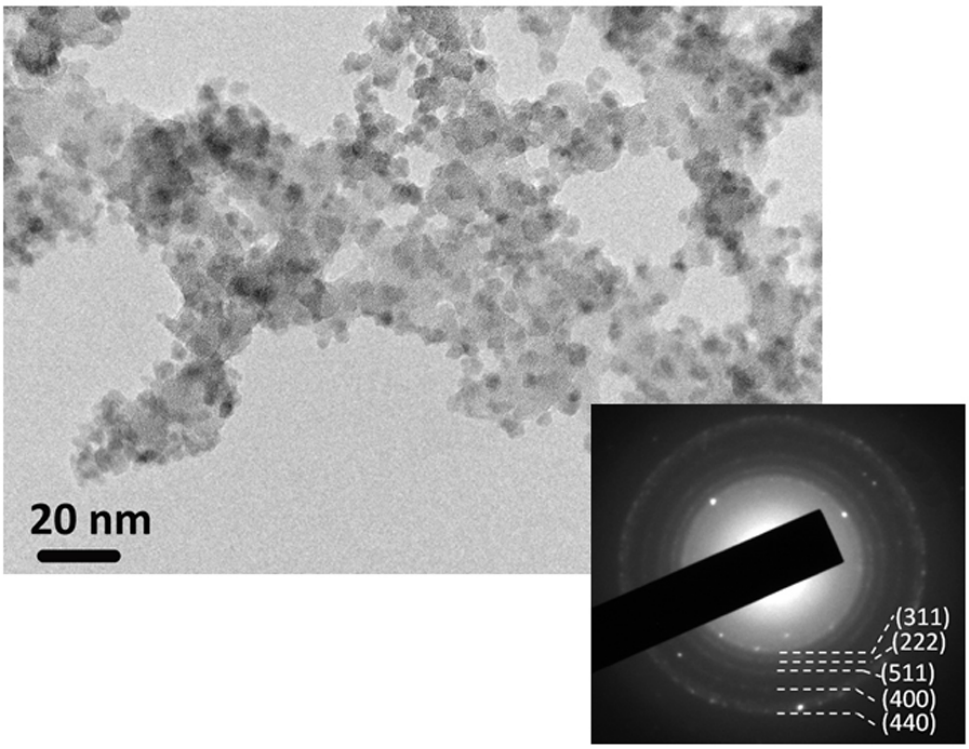

Figure 32: *Representative TEM image of the sample S@APS-SiO_2 with corresponding electron diffraction.*

The Figure 32 shows a TEM image of the sample S@APS-SiO_2. The TEM image reveals that silica surfaces are covered with globular nanoparticles in large surface concentration. The detailed TEM examination again revealed the absence of any homogeneously nucleated nanoparticles. Additionally, the TEM examination reveals that the nanoparticles are crystalline and of the size between 5–7 nm. The corresponding electron diffraction pattern revealed apart from diffuse rings of the amorphous silica also the sharp reflections that corresponded only to cubic spinel structure (Figure 32).

Regardless of the surface charge of the silica core nanoparticles (SiO_2 or APS-SiO_2) used for the synthesis, the results indicate that the reaction most likely followed the same chemical processes resulting in spinel particles at the core surfaces.

Presented results indicate that the selected reaction conditions used for the synthesis of S@SiO_2-10 and S@APS-SiO_2 (Table 4) obviously favor the heterogeneous nucleation of the initial product that subsequently, in chain of chemical reactions transforms into the final spinel phase. The heterogeneous nucleation of initial product to a large extent proceeds with thermal hydrolysis, before the addition of $Mg(OH)_2$. Further I have investigated the effect of extend of thermal hydrolysis on the morphology and type of the nucleation (heterogeneous and homogeneous) of the final products. Here I have selected different time interval (denoted as t_1 in Table 4) at which Fe precursors dissolved in the suspension of the silica core nanoparticles were aged at final temperature before $Mg(OH)_2$ was admixed. First, at t_1=0, the $Mg(OH)_2$ was admixed into silica core suspension together with Fe precursors (Sample M@SiO_2-0 in Table 4), whereas at t_1=60 min, the reaction mixture was aged first at 60 °C for 60 min before $Mg(OH)_2$ was admixed (Sample M@SiO_2-60 in Table 4). The synthesized products, together with reaction conditions and results obtained after TEM examinations are listed in Table 4.

Table 4: *List of reaction conditions used for synthesis of spinel in the suspension of silica core nanoparticles (SiO_2 or APS-SiO_2) and the results of product analyses.*

Code	Core nanoparticles	React conditions			Stage	TEM	
		T (°C)	t_1* (min)	t (min)		Size (nm)	Nucleation**
S@SiO_2-10	SiO_2	60	10	10	1	3	HEN(L)
	SiO_2	60		25	2	3–5	HEN(L+S)
	SiO_2	60		210	3	5–7	HEN(S)
S@APS-SiO_2	APS-SiO_2	60	10	10	1	3	HEN(L)
	APS-SiO_2	60		30	2	3–5	HEN(L+S)
	APS-SiO_2	60		220	3	5–7	HEN(S)
S@SiO_2-0	SiO_2	60	0	/	1	/	/
	SiO_2	60		3	2	5	HEN(S)+HON(S)
	SiO_2			6	3	5–7	HEN(S)+HON(S)
S@SiO_2-60	SiO_2	60	60	60	3	3-5	HEN (L+G)
	SiO_2	60		63	2	5	HEN (S)+HON (L)
	SiO_2	60		120	3	5–7	HEN (S)+HON (G)

* denotes the time interval for which the reaction mixture maintained at 60 °C before the $Mg(OH)_2$ was added

**HON and HEN denotes homogeneous and heterogeneous nucleation, respectively. S,

L, and G stands for spinel, lepidocrocite (γ-FeOOH) and goethite (α-FeOOH)

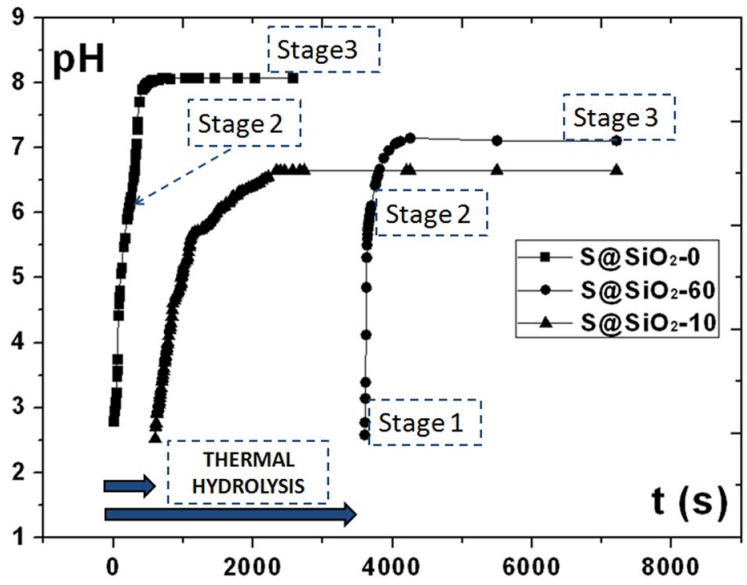

Figure 33: *pH vs. time curve for the sample S@SiO₂-0, S@SiO₂-10 and S@SiO₂-60 monitored during the course of reaction*.

First, when $Mg(OH)_2$ was admixed to the silica core nanoparticles suspension (60 °C) together with Fe precursors (sample S@SiO_2-0) rapid increase of the hydroxyl ions concentration was observed (Figure 33). This resulted in a steep increase in pH of the suspension, much steeper to that measured for the sample S@SiO_2-10, where $Mg(OH)_2$ was admixed only after the reaction mixture remained at the final temperature for 10 min. In a short period of only 3 min, the pH value of 6 was reached while it further increased to the value above 8 in another 3 min. After gradual decrease in the curve slope, the final pH of 8.2 was reached.

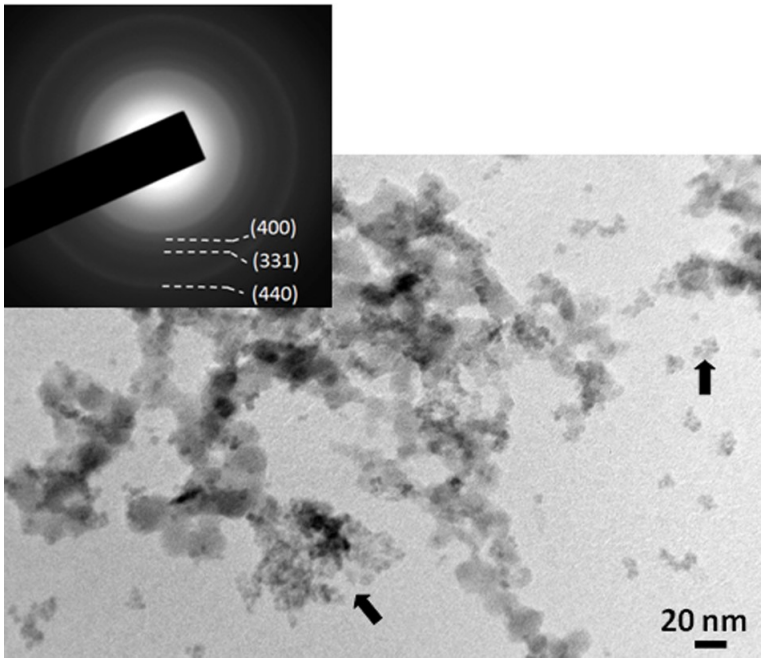

Figure 34: *Representative TEM image corresponding to stage 2 of sample S@SiO₂-0 with the corresponding electron diffraction pattern.*

The intermediate product corresponding to stage 2 of product S@SiO₂-0 was examined using TEM. Figure 34 presents the TEM image of the intermediate product of S@SiO₂-0 that was sampled after pH increased to the value of 6. It is evident from the TEM image that the sample consists of two types of particles: the larger amorphous silica spheres and the agglomerates of smaller spherical particles of approximately 3–5 nm. The EDS spectra confirms the formation of the Fe-rich phase, while electron diffraction pattern taken over larger area shows week diffraction rings that can be indexed according to the spinel structure. Detailed TEM observation revealed the absence of other Fe-phases. Spinel in the form of the small nanoparticles is seen on the surface of silica spheres, as well in the form of small agglomerates lying separately from the silica core nanoparticles (marked with arrow on Figure 34). The latter are strongly agglomerated, while spinel nanoparticles on silica core nanoparticles are arranged distance apart. These results indicate that the nanoparticles on the silica surfaces most likely nucleated heterogeneously, rather than homogeneously in solution and adhere to the silica surfaces only during drying of the sample on specimen support, where agglomerated particles nucleated homogeneously in solution.

The reaction conditions that were established during the synthesis of the S@SiO₂-0 nanocomposite particles obviously lead to the spinel formation. However, rapid increase of hydroxyl ions at the beginning of the reaction increased the supersaturation of the initial product over the value needed for the homogeneous nucleation.

In the next experiment, the $Mg(OH)_2$ was admixed into the reaction mixture (suspension of silica core nanoparticles and Fe precursors), only after it remained at the final temperature for 60 min. Figure 33 shows pH vs. time curve for the sample S@SiO₂-60. The reaction mixture was maintained at the initial pH of 2.2 for 60 min before the addition of $Mg(OH)_2$ caused rapid increase in the hydroxyl ion concentration, where pH value for the precipitation of Fe^{2+} ions was reached in a time interval of only 3 min. Final pH of 7.2 was reached in another 10 min, while after the 2 hours the reaction was stopped

and the product was examined using TEM.

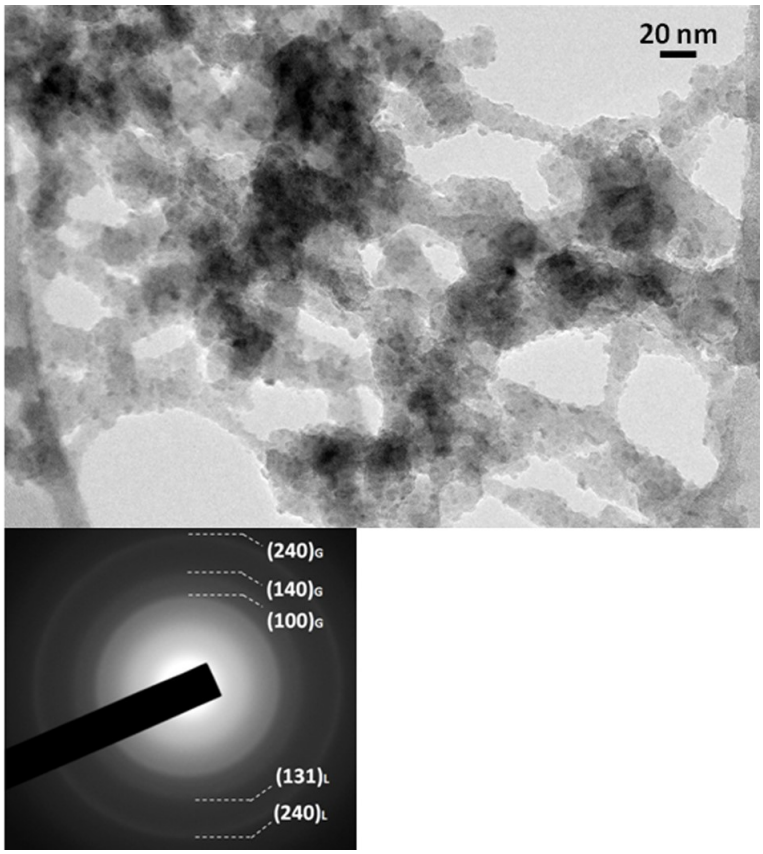

Figure 35: *Representative TEM image of product corresponding to Stage 1 of sample S@SiO₂-60 (a) and corresponding electron diffraction pattern recorded over large area of the material (b).*

Figure 35 presents the TEM image of the intermediate product sampled at the end of the Stage 1 of the sample S@SiO_2-60. TEM image shows that the surfaces of the silica core nanoparticles are partially covered with small globular nanoparticles, of size between 3 and 5 nm. The electron diffraction pattern recorded from the large area reveals the diffuse rings that can be ascribed to, either (240), (140) and (100) planes of the orthorhombic structure of α-FeOOH, or (131) an (240) planes of the orthorhombic structure of γ-FeOOH. Distinction between the both phases is difficult due to overlapping of the diffraction rings together with small particles size and consequently diffuse reflections, however, formation of both phases is consistent with the reaction conditions. After the addition of $Mg(OH)_2$, the increase in pH caused the precipitation of Fe^{2+}. The TEM image (Figure 36a) of intermediate product sampled after pH of 6 was reached, showed the presence of large sheet-like particles and agglomerates of the silica nanoparticles. Detailed examination revealed that the surfaces of the silica nanoparticles were partially covered with the small spherical particles of approximately 3–5 nm.

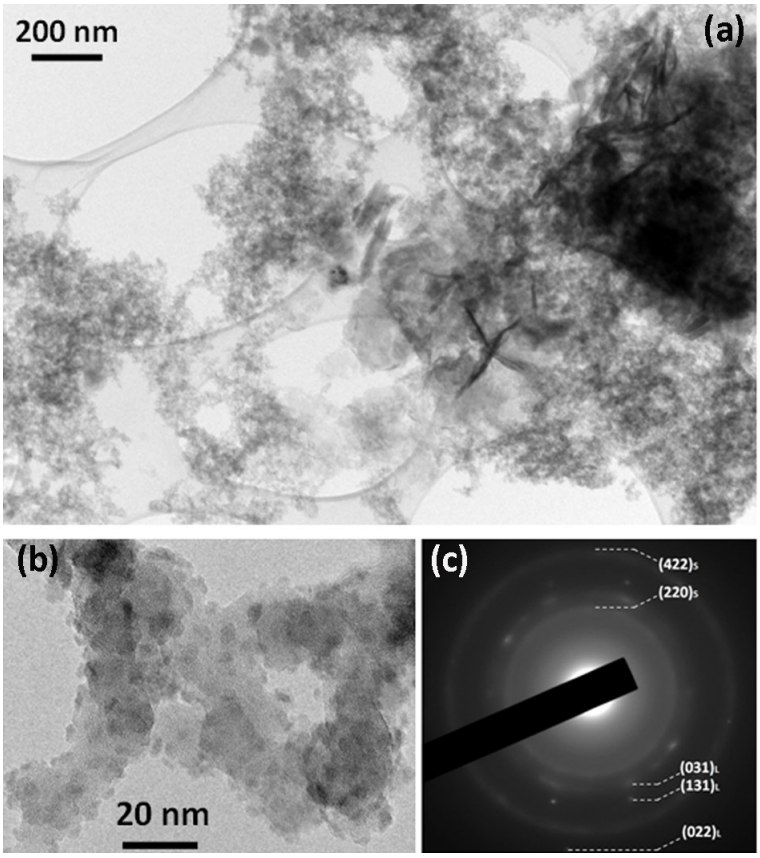

Figure 36: *Representative TEM image of second intermediate product of sample S@SiO₂-60 (a), TEM image revealing heterogeneously nucleated spinel nanoparticles on the silica core surfaces (b) and corresponding electron diffraction recorded over large area of the material (c).*

The electron diffraction pattern taken from the larger area of the material indicates the formation of the phases that diverse in their crystalline order: apart from diffuse rings originating from the small nanoparticles, discrete reflections indicate the phase of better crystallinity. The diffraction rings can be indexed according to the cubic spinel structure while discrete reflection matches to the orthorhombic γ-FeOOH structure. The detailed TEM observation reveals that all the spinel nanoparticles are located exclusively on the surfaces of the silica spheres while homogeneously nucleated spinel nanoparticles were never detected. The γ-FeOOH phase obviously nucleated homogeneously in the suspension and subsequently grew to the final form of sheet-like particles. Finally, the product was collected after the reaction mixture was aged at the final pH of 7.2 for 2 hours. The TEM image of the final product shown in Figure 37 reveals the presence of the particles with distinct morphology. The sample contained, apart from silica spheres, also large rood-like particles with length of approximately 300 nm and width of 50 nm.

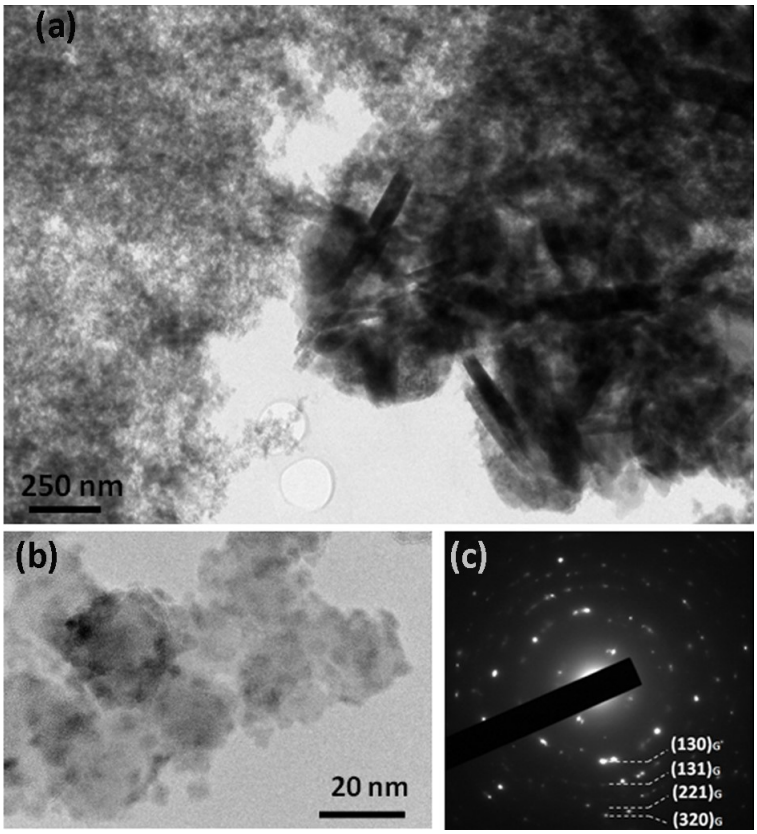

Figure 37: *Representative TEM image of final product of sample S@SiO₂-60 (a), TEM image revealing heterogeneously nucleated spinel nanoparticles on the silica core surfaces (b) and corresponding electron diffraction pattern recorded over limited area of rood-like particles shown in (25a) (c).*

Detailed TEM observation revealed that the surface of silica spheres is covered with the spherical nanoparticles, which size increased to 5 nm, while the electron diffraction confirmed the cubic spinel structure. The electron diffraction recorded only over selected area of the rod-like particles reveals the well crystalline phase with discrete reflections that can be indexed according to the orthorhombic α-FeOOH structure.

When the thermal-hydrolysis stage was prolonged to 60 min, apart from γ-FeOOH, also α-FeOOH phase formed. Both phases nucleated heterogeneously on the surfaces of the silica core nanoparticles. The α-FeOOH was formed because of the pronounced growth of the previously-formed γ-FeOOH nanoparticles. γ-FeOOH phase is stable only at the particles size below 5 nm, where at increasing particles size, it transforms to more stable α-FeOOH [43, 44].

As reaction further proceeds the γ-FeOOH phase transforms into spinel and remains on the silica surfaces. However, γ-FeOOH phase forms also homogeneously in the solution as a consequence of Fe^{2+} excess. Thus, the final product contained the mixture of the spinel phase on the silica core surfaces and the larger α-FeOOH particles, formed with the transformation from homogeneously-nucleated sheet-like γ-FeOOH particles.

4.3.3 S@BaM nanocomposites particles

To attain the knowledge regarding the influence of the crystal structure of the core nanoparticles on the spinel formation, the synthesis was also done in the suspension of the Ba-hexaferrite core nanoparticles (later referred to as BaM). Here, the Ba-hexaferrite core nanoparticles of different size, size distribution and morphology were selected (Table 3, chapter 4.2.2.).

In contrast to the amorphous silica core nanoparticles, the Ba-hexaferrite core nanoparticles exhibit crystalline order (Figure 27). Furthermore in certain crystallographic directions the Ba hexaferrite also exhibit structural similarities with spinel structure. Large surfaces of BaM core nanoparticles, which are parallel with {0001} basal planes of their hexaferrite structure exhibit the same oxygen stacking as {111} planes of cubic spinel structure. I assumed that this structural similarity will cause the preferential growth of spinel on basal planes of hexaferrite.

Furthermore, the Ba-hexaferrite core nanoparticles in dependence of their size and morphology also exhibit certain interesting magnetic properties (Table 3, chapter 4.2.2.) Especially when nanoparticles are larger but still singledomain (BaM_{100}), they typically exhibit hard magnetic properties, in contrast to the soft magnetic spinel phase. I assumed that the synthesis of the nanocomposite particles consisting of the hard magnetic hexaferrite core and the soft magnetic spinel shell would result in their improved magnetic properties. Because to the exchange coupling of the magnetic moments of both phases the synthesized nanocomposite would exhibit increased magnetization due to the soft magnetic phase, and high remanence duo to the hard magnetic hexaferrite. However, the exchange coupling will only be efficient in the absence of any intermediate layer between both phases, especially if the spinel phase will grow epitaxially on the BaM core surfaces.

4.3.3.1 Effect of core nanoparticles structure

First, the Fe precursors were dissolved into the air bubbling aqueous suspension of the Ba-hexaferrite core nanoparticles $BaM_{10\text{-}70}$ at temperature of 60 °C. After the suspension remained at final pH of 2.2 for 10 min to allow thermal hydrolysis of Fe^{3+}, the $Mg(OH)_2$ was admixed, giving rise to the precipitation of Fe^{2+} ions. After the reaction mixture remained at final pH of 6.8 for 2 hours, the reaction was stopped and the collected products were examined using TEM. Figure 38a shows the representative TEM image of the sample $S@BaM_{10\text{-}70}$, revealing bimodal size distribution of small discoids and larger platelet crystals.

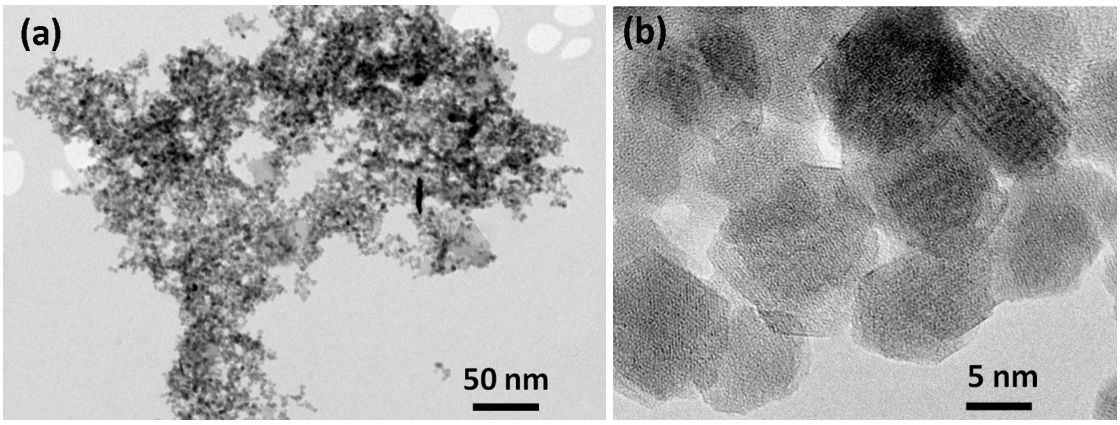

Figure 38: *Representative TEM image of S@BaM$_{10-70}$ nanocomposite particles (a) and TEM image at increased magnification revealing edge-shaped nanocomposite particles (b).*

Closer observations reveal that the surfaces of the BaM$_{10-70}$ core nanoparticles are covered with the layer of precipitated material. Actually, the layer is not easily observed by TEM, since the platelet core nanoparticles lay flat on the specimen support. However, there is notable change of the coated nanoparticles compared to the untreated BaM$_{10-70}$ core nanoparticles. The coated nanoparticles appear in the form of hexagonal platelets and were edge-shaped (Figure 38b) compared to the more rounded discoid core nanoparticles (Figure 27a–c). Due to the structural similarity between the hexaferrite structure of the core nanoparticles and the spinel structure of the shell, it is difficult to conclude whether the synthesized particles are really the nanocomposites or the mixture of the nanoparticles of the two different phases. It was only possible to define their structure, when the platelet nanoparticles were oriented edge-on, i.e., with its large faces parallel to the electron beam (Figure 39). They were always composed of the hexaferrite core and the spinel shell. The nanocomposite structure is easily visible as the hexaferrite structure in its c-dimension clearly differs from the cubic spinel structure. The new phase nucleated on the large surfaces of the BaM core nanoparticles, which are parallel to the basal planes of their hexagonal structure. The analysis of the HREM images (see later in the text) confirmed that this new iron-rich phase was spinel. The whole large surfaces of the core nanoparticles were completely covered with the uniform spinel layers. The spinel layers formed symmetrically on the both sides of the core nanoparticles, which resulted in the formation of sandwich-type nanoparticles. The layer was never present on the side surfaces of the platelet core nanoparticles, which are in some segment parallel to the prismatic {01-10} planes of the hexaferrite structure. The thickness of the spinel layer was of relatively uniform thickness, yielding approximately 2 nm. The thickness did not depend on the size of the individual core nanoparticle.

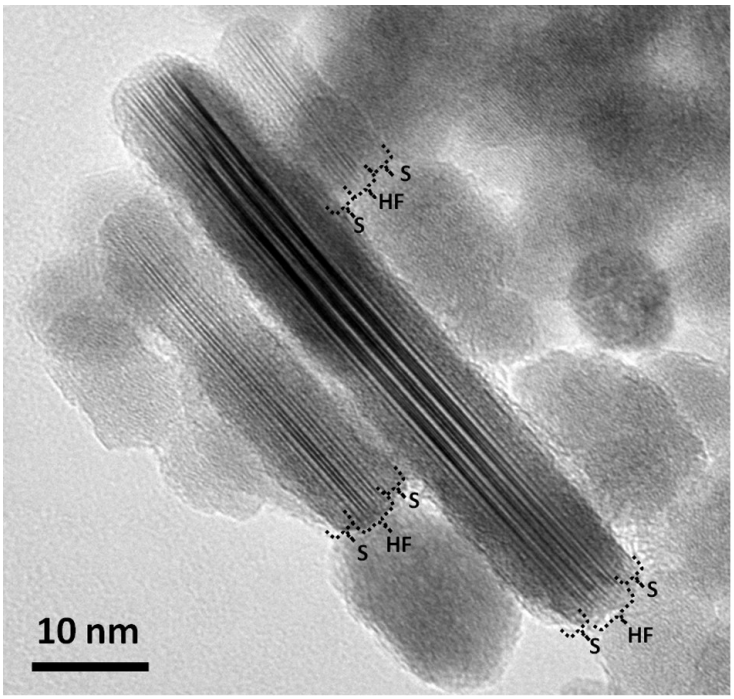

Figure 39: *Nanocomposite particles of sample S@BaM, oriented edge-on; HF denotes hexaferrite and S denotes spinel.*

Figure 40 compares the EDXS spectra of the product S@$BaM_{10\text{-}70}$ nanocomposite particle and the $BaM_{10\text{-}70}$ core nanoparticles. The EDXS spectra of the both show the presence of Ba, Fe and O, apart from Cu originating from the TEM specimen support.
The EDXS spectra were quantified using the well crystalline Ba-hexaferrite nanoparticle as the standard. The core nanoparticles contained 3.12±0.1 at. % of Ba and 37.5±0.08 at.% Fe, whereas the nanocomposite particles contained much higher concentration of Fe (38.8± 015 at.% Fe), and lower concentration of Ba (1.3±0.2 at.% Ba).

To investigate, whether the analyzed sample only consisted of the nanocomposite particles or additionally the homogeneously-nucleated spinel nanoparticles were present, a systematic EDXS analysis was performed. The EDXS analysis enables evaluation of the sample homogeneity in terms of the chemical composition. The comparison of several spectra recorded from different regions of the specimen including approximately 10 nanoparticles revealed no deviations in the chemical composition. These results strongly suggest that under given reaction conditions spinel phase nucleated only heterogeneously at the Ba-hexaferrite core nanoparticles. If the homogeneously nucleated nanoparticles would be present, the composition would vary.

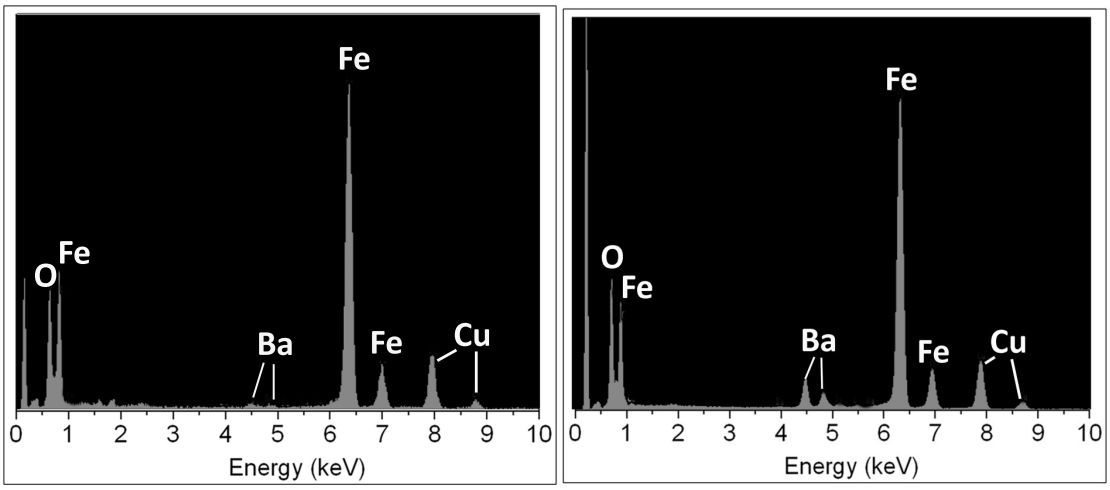

Figure 40: *EDXS spectra of S@BaM$_{10\text{-}70}$ nanocomposite particles (a) and BaM$_{10\text{-}70}$ core nanoparticles (b) (Cu originates from the specimen support).*

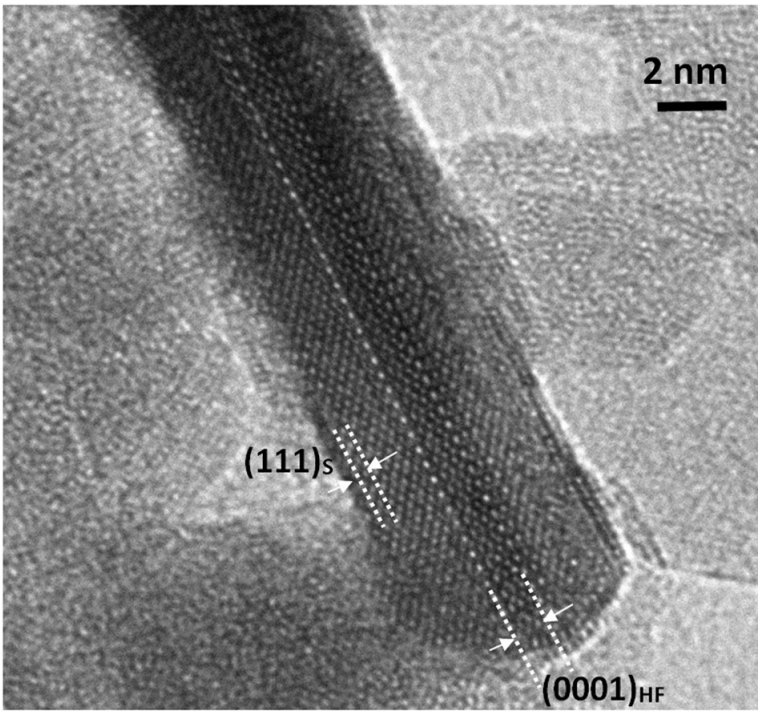

Figure 41: *HREM image of one nanocomposite particle oriented with its large surface parallel to the electron beam.*

The synthesized nanocomposite particles were further examined with high resolution electron microscopy (HREM). Figure 41 shows the HREM image of the nanocomposite particle that is oriented with its large surfaces parallel to the electron beam. The formed spinel layers at the hexaferrite core are well crystalline. The measured periodicity of the HREM image reveals that the hexaferrite core nanoparticle is oriented in the $<1010>_{HF}$ zone. The largest periodicity in the image of the core yields 11.5 Å corresponding to the distance between $(0002)_{HF}$ planes of the hexaferrite structure (marked in image of Figure

41). The HREM pattern of the surface layers corresponds to the cubic spinel structure in the $<110>_S$ zone. Here, the largest periodicity of 4.8 Å in the direction perpendicular to the platelet corresponds to $\{111\}_S$ planes of the cubic spinel structure (marked in Figure 41). The $\{0002\}_{HF}$ planes are parallel with the spinel $\{111\}_S$ planes. The thickness of the Ba-hexaferrite nanoparticle is 2.8 nm, that is just over the size of its hexagonal unit cell in the corresponding c-direction (2.3 nm), while the thickness of the spinel layer yields around 2 nm on each side of the hexaferrite core. The periodicity of the HREM image of the spinel layers terminates at the surface of the particle indicating no amorphous surface layer.

Also, the HREM analysis revealed that the spinel phase grew only on the basal planes of hexaferrite, while no spinel was observed at the side surfaces of the core particles. Thus, the nanocomposite particles have the form of multilayer or sandwich, rather than core-shell structure.

These results suggest that crystal structure of the core nanoparticles has an important effect on the spinel formation. When synthesis proceeded in the suspension of the amorphous silica core nanoparticles, the spinel phase formed on silica surfaces in the form of randomly-oriented discrete nanoparticles. In contrary, when synthesis proceeds in the suspension of the crystalline $BaM_{10\text{-}70}$ core nanoparticles, the uniform and homogeneous spinel layer was only obtained on the basal plains of the cores. Moreover, the spinel layer grew epitaxially forming coherent interface with $(0001)_{HF} \parallel (111)_S$. The $\{111\}_S$ spinel planes exhibit the same oxygen stacking as the $(0001)_{HF}$ basal planes of hexaferrite and the two structures perfectly match at the interface. However, the structure of the two phases does not match along c-direction of the hexaferrite structure. This attributes to the differences in the interfacial energies, which are lower for the coherent $(0001)_{HF} \parallel (111)_S$ interface. Thus, spinel formation preceded exclusively on the large surfaces of the hexaferrite core nanoparticles, which are parallel to $(0001)_{HF}$ planes. The hexaferrite core nanoparticles serve as templates directing the crystallization of the spinel layer.

4.3.3.2 Effect of the core nanoparticles size and morphology

The formation of the spinel layer can also depend on the core-nanoparticles size and morphology and the availability of the core nanoparticles surfaces for the precipitating species. I assumed that the nucleation would be in any case partially homogeneous if the concentration of the core nanoparticles would be too low. Thus the synthesis of spinel was done also in the suspension of the larger Ba-hexaferrite nanoparticles $BaM_{30\text{-}70}$ (Table 3), however, keeping the total surface area of the nanoparticles roughly the same as in the case for synthesis of the $S@BaM_{10\text{-}70}$ sample. In either case, only large surfaces of the platelet hexaferrite particles were considered as the core-surfaces. Thus, in the reaction mixture of the larger $BaM_{30\text{-}70}$ core nanoparticles, the numerical concentration of the nanoparticles was lower for over one order of magnitude. The experimental procedure of the spinel deposition remained the same as used for the sample $S@BaM_{10\text{-}70}$.

Table 5: *List of S@BaM products and the results of products analysis.*

Code	BaM core	React. Cond.		TEM	
	Size (nm)	T (°C)	t_1 (min)	Phase	Nucleation type*
S@BaM$_{10\text{-}70}$	10–70	60	10	BaM+S	HEN
S@BaM$_{30\text{-}70}$	30–70	60	10	BaM+S	HEN (s) + HON (S)
S@BaM$_{100}$	100	60	10	BaM+S + L	HEN (S) + HON (L)
S@BaM$_{10}$	10	60	10	New phase	HEN*

* HEN denotes heterogeneous, while HON homogeneous nucleation root
** S denotes spinel phase, L denotes lepidocrocite (γ-FeOOH), BaM denotes Ba-hexaferrite phase

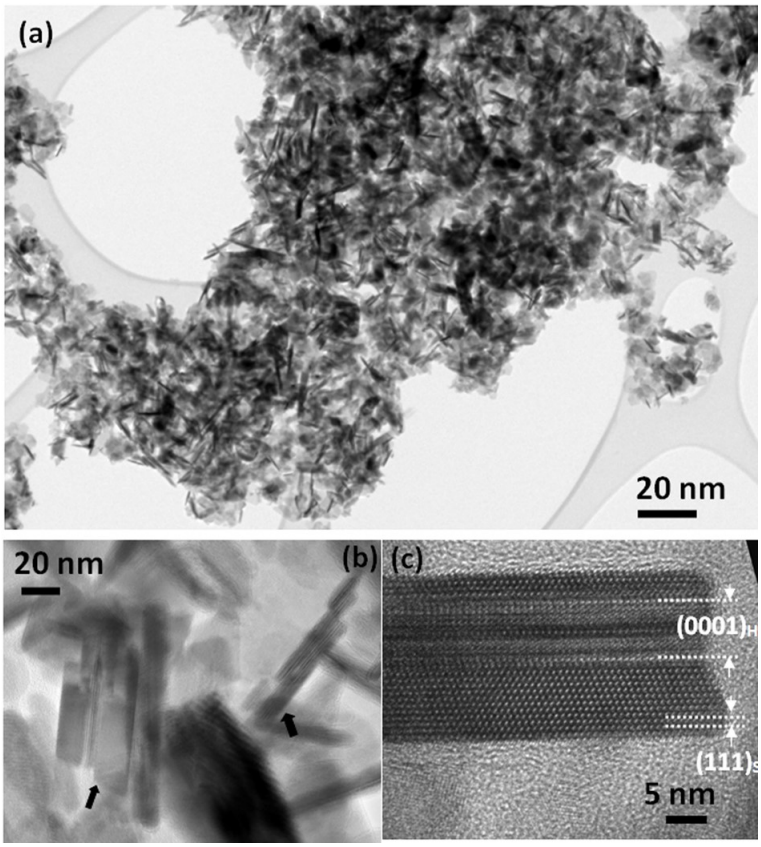

Figure 42: *Representative TEM image of the sample S@BaM$_{30\text{-}70}$ (a), TEM image revealing the S@BaM$_{30\text{-}70}$ nanocomposite particles of different thickness (b), and HREM image of the S@BaM$_{30\text{-}70}$ nanocomposite particle revealing the epitaxial growth of spinel phase on the hexaferrite core (c).*

Figure 42a shows the representative TEM image of S@BaM$_{30\text{-}70}$, revealing platelet morphology of the particles. Only detailed TEM analysis of the nanoparticles oriented with large surfaces parallel with the electron beam shows that they are nanocomposites particles. The large surfaces of the Ba-hexaferrite cores are covered with the uniform layers of spinel. Figure 42b also reveals that the spinel layers unlike in sample S@BaM$_{10\text{-}70}$, varies in the thickness between the particles (particles with two different layer thicknesses are marked with arrows in Figure 42b). Furthermore, the spinel layers at

individual core nanoparticles are frequently not symmetric on both sides of the core nanoparticles (Figure 42c). The observed variation is the spinel-layer thickness can be atribute to partial agglomeration of the BaM_{30-70} core nanoparticles. Due to their increased particles size and consequently improved crystalline order, the BaM_{30-70} core nanoparticles exhibit improved magnetic properties in comparison to BaM_{10-70}. Thus, apart from van der Waals attractive forces, particles tend to agglomerate also due to the magnetic dipole-dipole interaction. The inner surfaces of the core nanoparticles agglomerated into the stacks are less accessible for the precipitating species.

Detailed TEM observation also reveals that apart from heterogeneously nucleated spinel layers on the BaM core nanoparticles, also homogeneously nucleates spinel nanoparticles were present (Table 5). The homogeneously nucleated spinel nanoparticles appear in the form of large, octahedral nanoparticles of the size around 50 nm. The large particles size indicates that most likely during the synthesis, the conditions were close to those required for the heterogeneous nucleation. However, the lower numerical concentration of the core nanoparticles in the reaction mixture resulted in partial homogeneous nucleation since the core nanoparticles were not always available for the precipitating iron species.

To further investigate the effect of the core particles size and morphology, the spinel synthesis was also done in the suspension of the Ba-hexaferrite cores in the form of either large hexagonal platelet crystals, approximately 100 nm wide and 8 nm thick (BaM_{100}, Figure 27e,f) or in the suspension of the thin discoid nanoparticles, approximately 10 nm wide and 3 nm thick (BaM_{10} Figure 27c,d). Final products together with the reaction conditions and TEM observations are listed in Table 5.

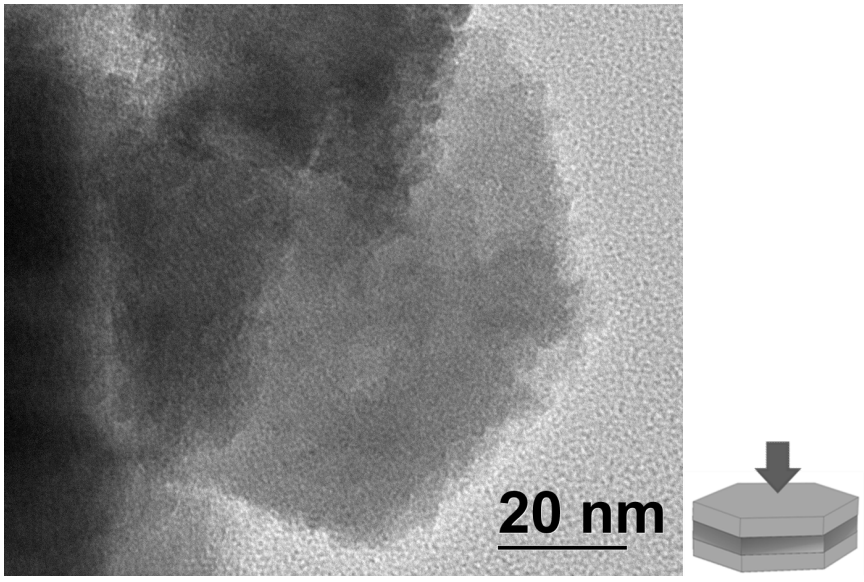

Figure 43: *TEM image of large hexagonal platelet crystal laying flat on specimen support, revealing the formation of layer of additional material on its surface.*

Figure 43 shows TEM image of sample S@BaM_{100} where spinel synthesis proceeded in the suspension of the BaM_{100} core nanoparticles. TEM image shows the Ba-hexaferrite platelet crystal laying flat on the specimen support. The surface of the Ba-hexaferrite crystal is covered with the additional material that gives appearance of increased roughness of the particle surface compared to the untreated core crystal shown in Figure 27e,f. When the nanocomposite particles were oriented with its large surface parallel with the electron beam the formation of the product layer on the both sides of the platelet crystal is clearly visible (Figure 44). Also here, the layers formed only at the large surfaces of the Ba hexaferrite core. Estimated thickness of new formed layer is approximately 7 nm on each side of the core nanoparticles, whereas the thickness of the BaM core nanoparticles yields approximately 5 nm.

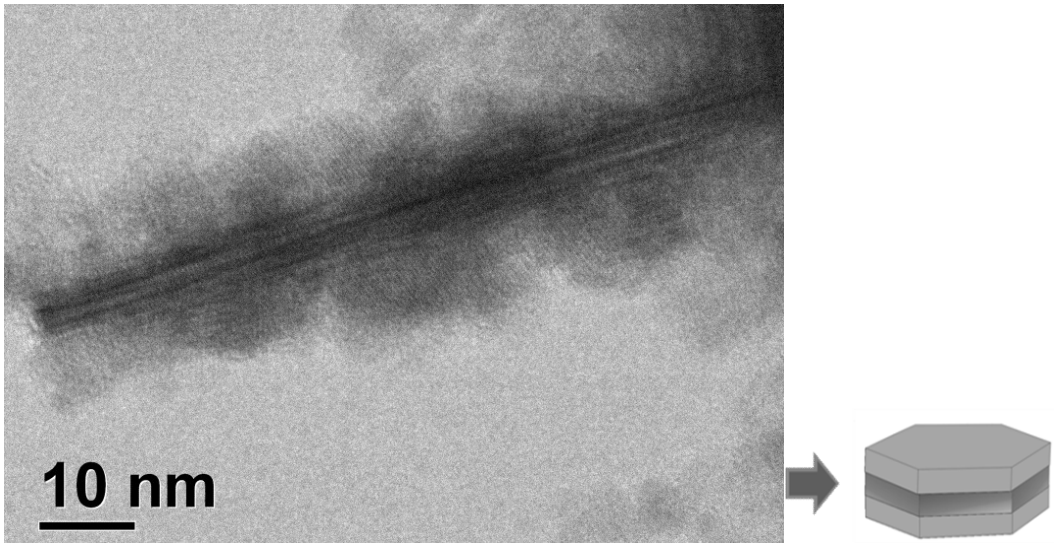

Figure 44: *TEM image of large hexagonal platelet crystal oriented with is large surface parallel with the electron beam.*

Detailed TEM observation of the sample S@BaM_{100} also showed absence of any homogeneously nucleated spinel nanoparticles. However, low concentration of homogeneously nucleated γ-FeOOH in the size between 3 and 5 nm was detected (Table 5). γ-FeOOH most probably formed due to the Fe^{2+} excess that was the consequence of partial Fe^{3+} coordination with free citric acid present in suspension of the core nanoparticles. The citric acid was used to assure colloidal stability of the core nanoparticles in the suspension during coating procedure.

The HREM analysis (Figure 45) revealed that the spinel layers at the core nanoparticles are well crystalline, growing epitaxially on the hexaferrite core. The thickness of the layer is nonhomogeneous, making the rough surface. Here, the larger size of the analyzed nanocomposite particle enabled recording of the diffraction pattern. The pattern confirms the orientational relationship between the two phases, defined by the $(0001)_{HF} \parallel (111)_S$ interface.

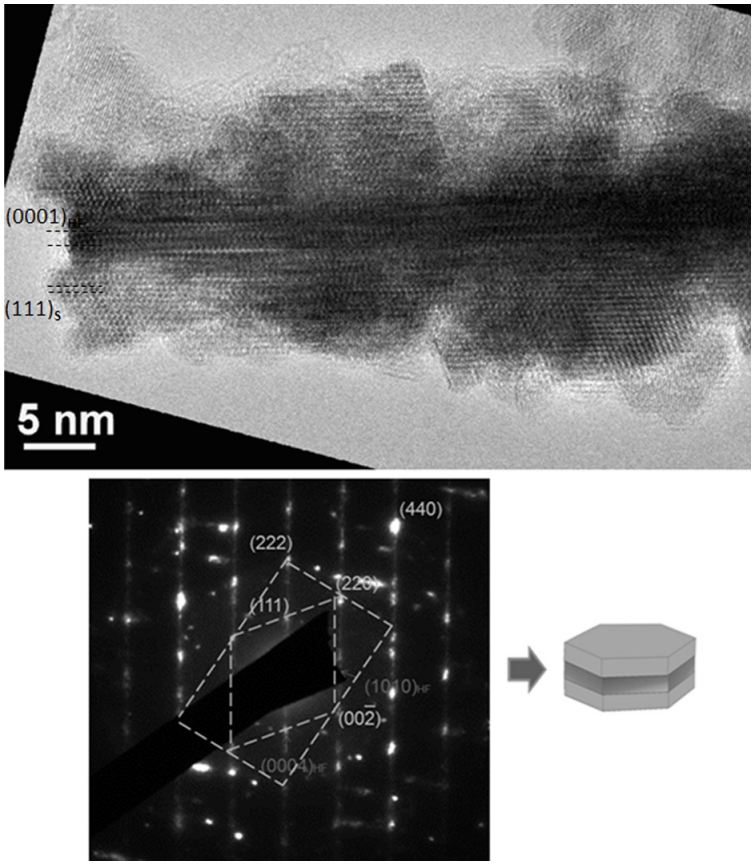

Figure 45: *HREM pattern of nanocomposite particles of sample S@BaM$_{100}$, oriented with its large surface parallel with the electron beam (a) and corresponding electron diffraction pattern revealing the superimpositions of reflection cubic spinel and hexagonal structure (b).*

Like in the case of S@BaM$_{10\text{-}70}$ and S@BaM$_{30\text{-}70}$ the core nanoparticles with their crystalline structure obviously influence the formation of spinel layers. When smaller core nanoparticles were used the spinel layers were uniform and homogeneous. The precipitated material nucleated homogeneously at the whole large surfaces of the nanoparticles. Conversely, at the much larger surfaces of the BaM$_{100}$ platelet crystals the spinel layer formed after nucleation at separate points at the surfaces. With growth these "islands" come to contacts. On the TEM image of the nanocomposite particle laying flat on the specimen support (Figure 46) several spinel nanoparticles of the anisotropic, elongated shape can be resolved at the surfaces of the core.

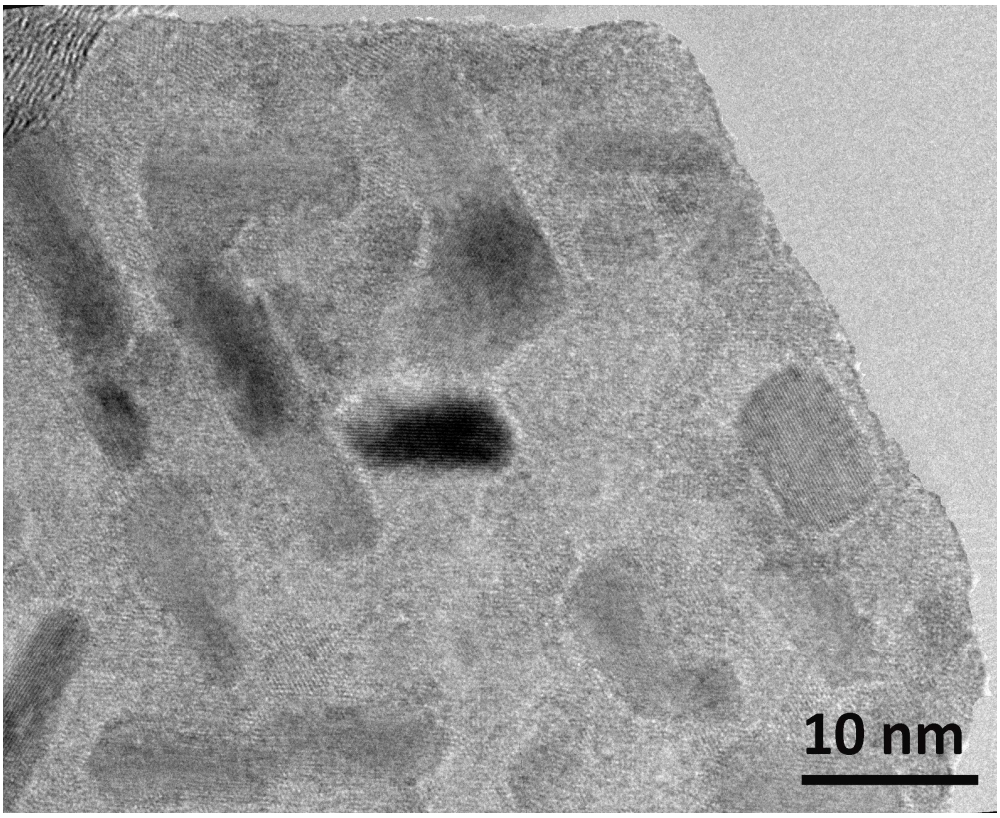

Figure 46: *TEM image of sample S@BaM$_{100}$, revealing hexaferrite platelet crystal lying with its large surface perpendicular to the electron beam.*

The deposition of the spinel layers also proceeded in stable aqueous suspensions of the 10 nm Ba-hexaferrite discoid nanoparticle (BaM$_{10}$). Figure 47 shows representative TEM image of product S@BaM$_{10}$, revealing that sample consists of uniform round shape particles. The particles appear thicker than the untreated Ba-hexaferrite core nanoparticles BaM$_{10}$ (Figure 27d). HREM analysis revealed that the Ba-hexaferrite core nanoparticles obviously reacted with the precipitated iron-rich species during the layer deposition. The HREM image of such particle (Figure 48) reveals the dominant periodicity along the particles thickness of approximately 9.5 Å that is significantly smaller to the periodicity of (0002) of the hexaferrite structure (11.5 Å, Figure 27d).

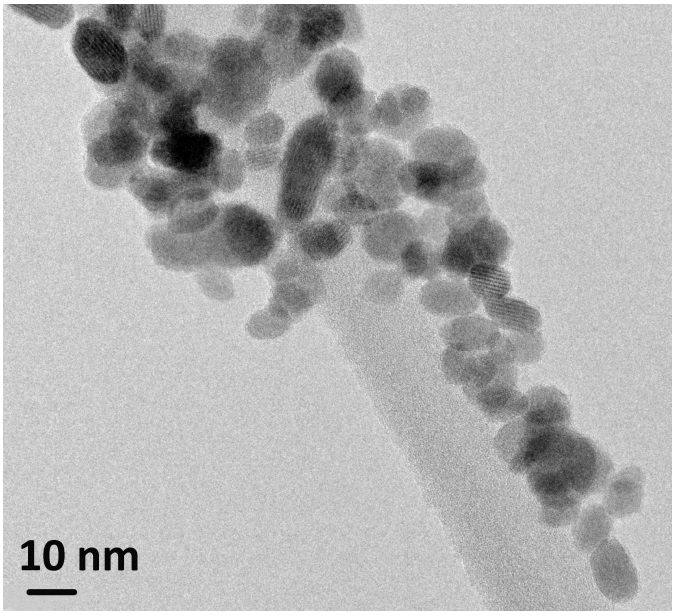

Figure 47: *Representative TEM image of S@BaM$_{10}$ nanocomposite particles*.

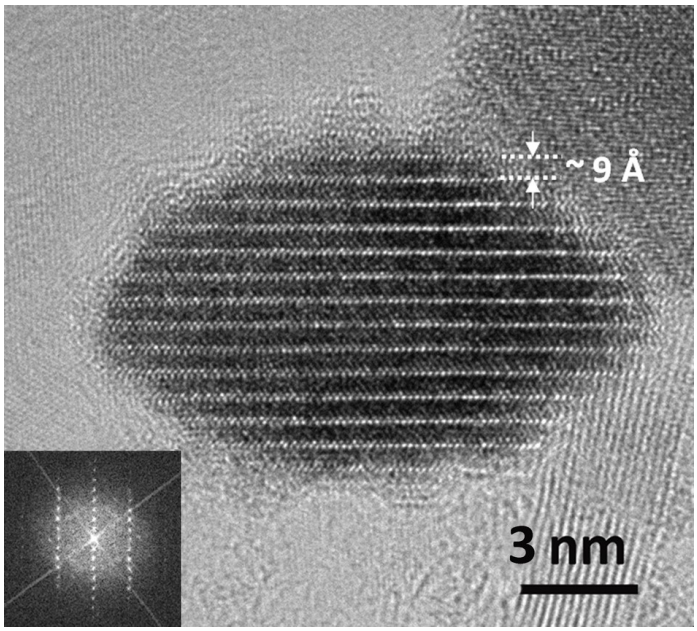

Figure 48: *HREM image of the S@BaM$_{10}$ particles (inset Fast Furrier Transform).*

Additionally, EDXS spectrum (not shown) of the particle shown in Figure 49 was compared with spectra of the Ba-hexaferrite nanoparticle standard. The analysis revealed significant decrease in Ba content compared to the composition of the hexaferrite, while the content of Fe slightly increased. The analysis showed 2.2±0.3 at.% of Ba ($BaFe_{12}O_{19}$ contains – 3.13 at.% Ba) and 37.9±0.2 at % of Fe ($BaFe_{12}O_{19}$ contains– 37.5 at.% Fe).

The ambiguous change in the structure of the core particle after the coating observed as change in the periodicity, as well as the change in the composition strongly suggest that the small BaM_{10} discoid nanoparticles reacted with the precipitated Fe species. Due to the small size, the core nanoparticles display poor structural order and have increased energy compared to well-crystalline material. This could be the reason for their high

reactivity after the Fe-rich material nucleated on their surfaces. The product particles are also more isotropic in comparison to the initial BaM_{10} core nanoparticles. It is known that the hexaferrite nanoparticles grow preferentially in the a-b plane [53, 55]. In contrary the product particles grew much more isotropically.

The product between the precipitated Fe species and the small hexaferrite core nanoparticles is not any of the known compounds. Also, there is no data on compounds with the composition and the structure close to that observed in the product particles in the literature. The difference in the periodicity observed in the product particles and that of hexaferrite (0002) is too large to be explained by small changes related to dissolution of additional Fe_2O_3 into the hexaferrite structure. Most probably, the product particles can be viewed as a new compound, stable only in the form of nanoparticles.

4.4 Magnetic properties

It is expected that the synthesized S@BaM nanocomposite particles will exhibit improved magnetic properties due to the synergy of two magnetically-different phases. Here the presence of the soft magnetic spinel phase can contribute to the improved magnetization, while coercivity is dominated by the Ba hexaferrite phase. The magnetic properties of the Ba-hexaferrite core nanoparticles significantly vary with particles' size and morphology. Here, the BaM_{10} core nanoparticles show superparamagnetic properties, while at increased size, for example monodomain BaM_{100} core nanoparticles show typic hard-magnetic behaviour.

Further, the HREM analysis (Chapter 4.3.2.2.) revealed that the spinel phase forms a coherent interface and grew epitaxially on the Ba-hexaferrite core nanoparticles. I assumed that this could give rise to the additional exchange coupling of the magnetic moments of both phases that can result in the samples improved energy product [56 - 60].

First the magnetic properties of the $S@BaM_{10\text{-}70}$ were evaluated. Figure 49 shows the magnetic hysteresis of $S@BaM_{10\text{-}70}$ nanocomposite particles in comparison to the untreated $BaM_{10\text{-}70}$ core. Here, the measurements reveal the significant increase in the saturation magnetization of the $S@BaM_{10\text{-}70}$ sample (31 Am^2/kg) in comparison to $BaM_{10\text{-}70}$ (7.1 Am^2/kg). Also the coercivity, due to the presence of soft magnetic spinel decrees (from 31 Am to 18 Am).

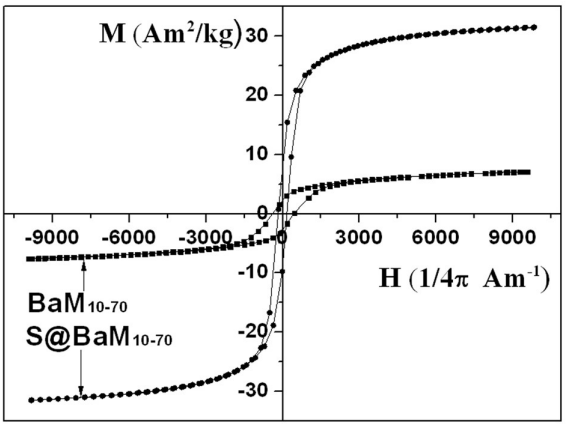

Figure 49: *Magnetic hysteresis of $S@BaM_{10\text{-}70}$ nanocomposite particle in comparison to $BaM_{10\text{-}70}$ core nanoparticles.*

The increase in the magnetization (from 1.3 to 3.3 Am^2/kg) measured at 1 T was also detected for the sample S@BaM_{10}, where BaM_{10} Ba-hexaferrites were used as the core nanoparticles (Figure 50). Here, the hysteresis of BaM_{10} core reveals that the majority of Ba hexaferrite particles are in or close to the superparamagnetic state. Typical superparamagnetic behavior (no remanence and coercivity) was also observed in the sample S@BaM_{10}.

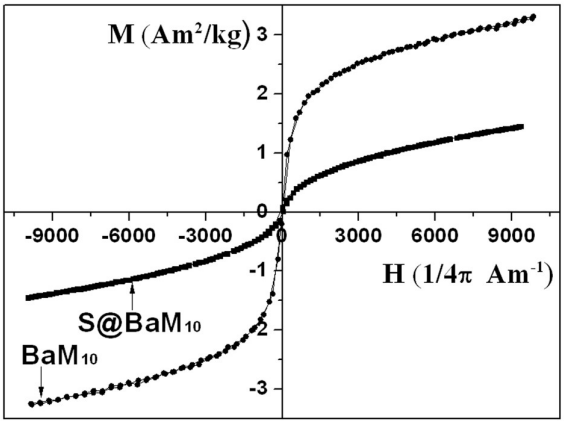

Figure 50: *Magnetic hysteresis of S@BaM_{10} nanocomposite particle in comparison to BaM_{10} core nanoparticles.*

In further experiments I have evaluated the magnetic properties of the synthesized S@BaM_{100} nanocomposite particles. From comparison of the magnetic hysteresis of S@BaM_{100} nanocomposite particles and untreated BaM_{100} core nanoparticles (Figure 51), notable differences are detected. Saturation magnetization of the BaM_{100} core nanoparticles (measured at 1T) yields 34.5 Am^2/Kg. High remanence of 17.8 Am^2/kg and coercivity of 203 A/m indicates its monodomain state. The magnetic hysteresis of S@BaM_{100} nanocomposite particles, however, show increased saturation magnetization (56 Am^2/kg) and increased remanence (28.2 Am^2/kg), while the coercivity slightly decreased (175 A/m). The observed increase in saturation magnetization and decrease in coercivity is due to the presence of the soft magnetic spinel phase. The soft magnetic spinel ferrite maghemite (γ-Fe_2O_3) typically exhibit higher saturation magnetization (bulk saturation magnetization 86 Am^2/kg) in comparison to hexaferrite (bulk saturation magnetization 72 Am^2/kg). The shape of the magnetic hysteresis for the S@BaM_{100} nanocomposite particles is similar to that measured for the untreated BaM_{100} core nanoparticles. This indicates the coherent switching of the magnetization of the both phases in the nanocomposite. The nanocomposite is switched as it would be a single magnetic phase, because the magnetic moments of both phases are coupled. For comparison, magnetic hysteresis of the untreated BaM_{100} core nanoparticles homogeneously mixed with superparamagnetic spinel nanoparticles (in the same volume ratio as present in S@BaM_{100}) were measured (Figure 52, $BaM_{100}S_{Mix}$). The magnetic hysteresis reveals slight increase in saturation magnetization (compared to the Ba hexaferrites core nanoparticles) and significant reduction in coercivity. However, the shape of hysteresis loops shows typical kinks revealing the incoherent, separate switching of both phases in reverse field and negligible changes in remanence.

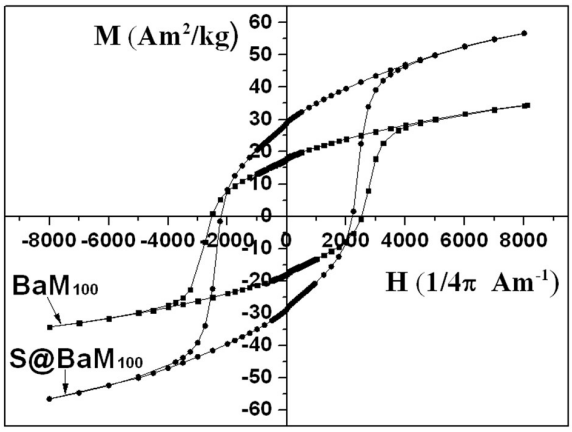

Figure 51: *Magnetic hysteresis of S@BaM$_{100}$ nanocomposite particle in comparison to BaM$_{100}$ core nanoparticles.*

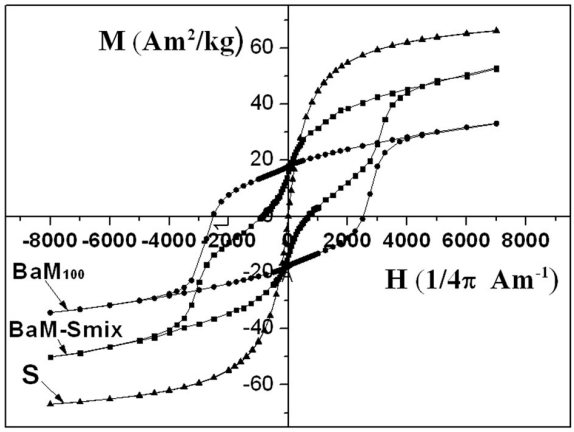

Figure 52: *Magnetic hysteresis of BaM$_{100}$ core nanoparticle, superparamagnetic spinel nanoparticles and their homogeneous mixture BaM-S$_{MIX}$.*

The increased remanence in sample S@BaM$_{100}$ however, cannot only be ascribed to the exchange-coupling interaction. The increase in remanence can also be observed as a result of preferred alignment due to the particles platelet morphology. I assumed that both, the BaM$_{100}$ core nanoparticles and the S@BaM$_{100}$ nanocomposite particle will partially orient due to their platelet morphology. Thus the resulting increase in remanence can be the sum of both effects; magnetic coupling and preferential orientation. To evaluate the contribution of the particles' preferred alignment due to their platelet morphology, the particles in the both samples (BaM$_{100}$ core nanoparticles and S@BaM$_{100}$ nanocomposite particles) were prepared in the form of magnetically oriented assembly. To reduce the additional effect of the inter-particles interaction, the nanoparticles were first hydrophobized and then a low concentration of the nanoparticles was homogeneously dispersed in a liquid wax. The particles were magnetically oriented in the homogeneous magnetic field of 1 T and then the wax was solidified by cooling.

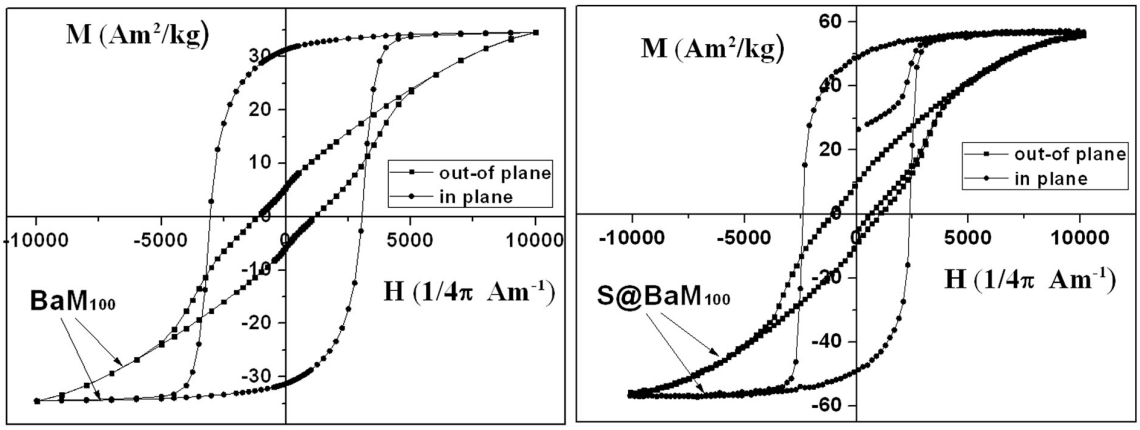

Figure 53: *Magnetic hysteresis of magnetically-oriented BaM_{100} core nanoparticles (a), and magnetically-oriented S@BaM_{100} nanocomposite particles (b).*

Figure 53a shows the magnetic hysteresis of the oriented BaM_{100} core nanoparticles, where the hysteresis was measured with field either parallel (in - plane) or perpendicular (out-of plane) to the Ba-hexaferrite easy - axis. The magnetic easy axis of the Ba hexaferrite is oriented parallel to the crystallographic c-direction, i.e, along particles thickness.

Large difference in the ratio between remanent and saturation magnetization (*Mr*/*Ms*) of both hysteresis indicates good magnetic orientation of the particles. Figure 53b shows magnetic hysteresis of the oriented S@BaM_{100} nanocomposite particles measured parallel and perpendicular to the samples easy axis. A good particle magnetic orientation is again indicated with large differences in *Mr*/*Ms* ratio of either hysteresis.

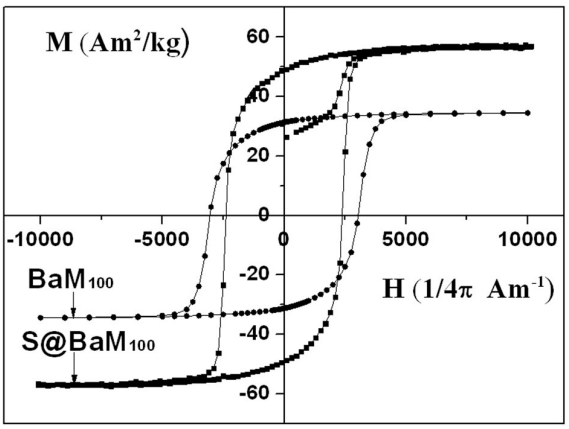

Figure 54: *In-plane magnetic hysteresis of oriented BaM_{100} core nanoparticles compared to in-plane oriented S@BaM_{100} nanocomposite particles.*

Finally the in-plane magnetic hysteresis of the oriented BaM_{100} core nanoparticles was compared to the in-plane magnetic hysteresis of the oriented S@BaM_{100} nanocomposite particles (Figure 54). The comparisons of the remanent magnetization of both oriented samples revealed the increased remanence of S@BaM_{100} for 35%.

Further the energy product was evaluated for the sample S@BaM_{100} and compared to the energy product of the untreated BaM_{100} core nanoparticles. Figures 55 and 56 show the $B(H)$ loops for BaM_{100} and S@BaM_{100} sample. Here the shaded area corresponds to the energy products. The estimated value of the energy product for the untreated BaM_{100}

core nanoparticles was 7.2 kJ/m^3. The exchange spring interaction, present in the S@BaM$_{100}$ nanocomposite particles caused the increase of energy product for 53 %, to 15.2 kJ/m^3.

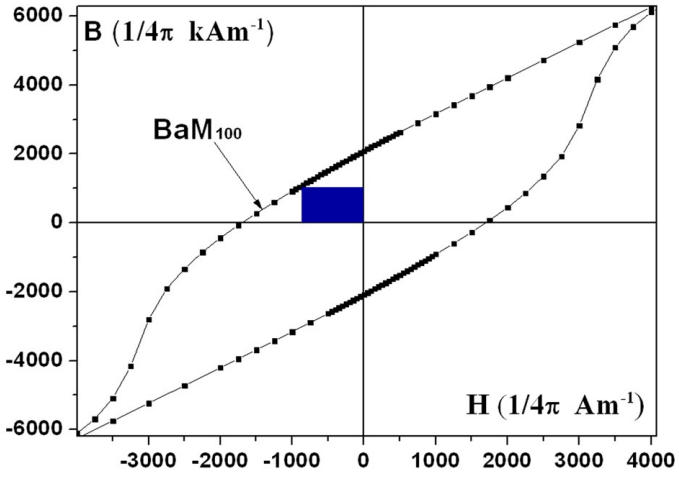

Figure 55: *B(H) loop for the sample BaM$_{100}$. The shaded area indicates the corresponding energy product* $|BH|_{MAX}$.

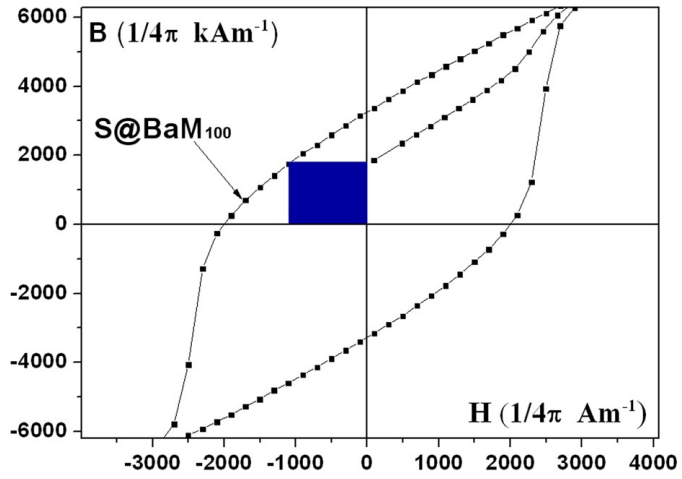

Figure 56: *B(H) loop for the sample S@BaM$_{100}$. The shaded area indicates the corresponding energy product* $|BH|_{MAX}$.

5 Discussion

The preparation of uniform layers of magnetic iron oxides (later referred to as spinel) on the surface of selected colloidal core nanoparticles is desired since it would open the possibility to prepare numerous different multifunctional materials. Especially when nanoparticles of different functionalities (besides magnetic also ferroelectric, photocatalytic, etc.) would be selected as core nanoparticles, the formation of magnetic spinel layer on their surfaces would result in the synthesis of novel multifunctional nanocomposite particles. The formation of spinel layer can either enhance the magnetic properties or core-nanoparticles or it can lead to synergy of properties when the core-nanoparticles of other functionalities are applied. These new properties, alongside the ability to manipulate them using the powerful tools of wet-chemistry also leads to potential applications of these colloidal nanocomposite particles in diverse fields in biological tagging [61–63], medical diagnostics and treatment [64–66] magneto-optical applications [67] and several others.

The synthesis of spinel with homogeneous nucleation in the solution was described in detail in the introduction (Chapter 1.3). There, different wet-chemical approaches like: co-precipitation [26], synthesis in microemulsion [9], hydrothermal synthesis [11–12], sonochemical synthesis [10], sol-gel method [16] and thermal decomposition of metal organic compound [13–14], are described.

Among all available known methods for the synthesis of spinel nanoparticles, however, data in literature comprise only limited reports on the synthesis of spinel layers on the surface of colloidal core nanoparticles [68–73]. Furthermore, the reported methods are characterized by several drawbacks. Typically, the spinel layers are formed after high temperature treatment (around 300 °C) of toxic organic Fe precursors (Fe-$(acac)_3$, $Fe(CO)_5$, etc.) in organic solvents [74–77]. Apart from complex synthesis procedures, the use of organometallic reagents besides its increased production costs, significantly enhance the possibility of environmental pollution [78]. Furthermore, the synthesis with thermal decompositions proceeds very fast, which hinders the desired, controlled heterogeneous nucleation of spinel. Thus apart from spinel on the core surfaces, also homogeneously nucleated spinel nanoparticles are often detected [73].

The synthesis procedure that would be simple and at the same time efficient in terms of the selective spinel formation following heterogeneous nucleation thus still remains a challenge.

The method developed in my studies comprised the formation of spinel layers with simple co-precipitation of mix valent Fe^{2+}/Fe^{+3} ions. The co-precipitation technique is probably the simplest and most efficient method for the synthesis of spinel nanoparticles. Further the method involves the use of Fe salts and it proceeds in aqueous solutions, which limits its environmental impact. The co-precipitation method is otherwise widely used for the synthesis of spinel nanoparticles, however, there is no data in the literature that such simple procedure would also be modified for the synthesis of spinel layers on colloidal core nanoparticles.

Generally, the synthesis of spinel nanoparticles with co-precipitation proceeds with the addition of hydroxide into the Fe^{2+}/Fe^{+3} ions solution involving high supersaturation. This

results in the formation of spinel following homogeneous nucleation. The spinel formation proceeds according to the following chemical reactions:

Fe^{2+} (aq)+ $2Fe^{3+}$ (aq)+ $8OH^-$ (aq)→ Fe_3O_4 +$4H_2O$
$2Fe_3O_4$ +½O_2 → 3γ-Fe_2O_3

Aging of the Fe^{2+}/Fe^{+3} ions solution at pH 3 first results in the formation of $Fe(OH)_3$ that immediately transforms into Fe oxide hydroxide. The precipitation of Fe^{2+} ions that proceeds at higher pH (6.2) is achieved with rapid addition of hydroxide. The precipitated Fe^{2+} ions then react with FeOOH phase resulting in spinel formation. First, magnetite Fe_3O_4 is formed that in air ambient oxidizes into maghemite γ-Fe_2O_3 [43, 44].

Typically the synthesis of spinel nanoparticles proceeds under conditions of very high supersaturation that results in rapid burst of nuclei through the reaction vessel. The process is very fast and it happens in a very narrow concentration range, which limits its control. At reaction conditions resulting in high supersaturation of nucleating species, the controlled heterogeneous nucleation and thus formation of spinel layers is impossible to be achieved. Conversely, reaction conditions leading to the low supersaturation of nucleating species would result in lower concentration of the formed nuclei and thus enabled better control.

In my work, I have concluded that when reaction conditions leading to the low supersaturation of nucleating species would be achieved, the reaction conditions will be closer to those required for heterogeneous nucleation.

To coat the spinel on the surface of the core nanoparticles, the supersaturation of the first initial phase formed was closely controlled. This was achieved with the close control of the kinetics of the initial phase formation and by maintaining low concentration of the reactants. At the same time it was crucial to assure reactants homogeneity throughout a reaction vessel.

First issue arises from the high reactivity of Fe^{3+} toward hydroxylation [25]. The hydroxylation of Fe^{3+}ions proceeds either with addition of hydroxide or with heat treatment above 55 °C [47, 48, 80]. In either case the process is very rapid and in dependence of the reaction conditions (pH, concentration, ionic strength) results in the formation of Fe oxide hydroxide of different crystallographic modifications (γ-FOOH, α-FeOOH or β-FeOOH) [25, 81, 82].

It is known from the literature that the hydrolysis of Fe^{3+} ions can only be controlled in the presence of strong polydentate ligands like polycarboxylate or amino ligands [25]. I have tested different Fe^{3+}-complexing ligands like oxalate, ureate, citrate and ammonium citrate.

In my work, I have selected urea as a complexing ligand since it forms water soluble complex with Fe^{3+} ions, ($[Fe((CO(NH_2)_2)_6)](NO_3)_3$) (later referred to as Fe^{3+}-urea). Fe^{3+}-urea complex also demonstrated its room temperature stability over wide pH region. However, the complex decomposes at elevated temperatures, enabling the desired slow and gradual release of Fe^{3+} ions, simply by the temperature control. The decomposition of Fe^{3+}-urea complex can be described with the following chemical reaction:

$[Fe((H_2N)_2C=O)_6](NO_3)_3 \rightarrow Fe^{3+}$ (aq) + $3NO_3^-$ (aq)+ 6 $(NH_2)_2CO$

Simultaneously with the Fe^{3+} ions release, their hydroxylation proceeds when the temperature exceeds 55 °C, due to thermal hydrolysis. This resulted in the formation of Fe oxide hydroxide of certain crystallographic modification. The processes can be described according to the following chemical reactions:

$Fe^{3+}(aq) \leftrightarrow Fe(H_2O)_{6-n}\,(OH)_n^{(3-n)}\,(aq)$
$2Fe(OH)_3 \rightarrow 2\gamma\text{-}FeOOH + 2H_2O \rightarrow \gamma\text{-}FeOOH + \alpha\text{-}FeOOH + 2H_2O$

I have determined that during the Fe^{3+}-urea decomposition that results in gradual release of Fe^{3+} ions, the Fe oxide hydroxide phases form in sequence. The first phase formed is γ-FeOOH, while increasing temperatures and prolonging temperature exposure resulted in its transformation to the thermodynamically more stable α-FeOOH phase. Data from literature state that the thermal hydrolysis of Fe^{3+} ions solution can result in the formation of γ-FeOOH phase. However, this happens only at very small particles size (below 5 nm), where the decreased surface enthalpies for hydration increases the thermodynamic stability of γ-FeOOH.

Spinel phase forms when formed γ-FeOOH phase will reacts with precipitated Fe^{2+} ions. The precipitation of Fe^{2+} is initiated with the addition of precipitating agent. Here it was crucial that the hydroxyl ions are released homogeneously through the reaction vessel resulting in controlled Fe^{2+} precipitation.

Conventionally, in the spinel synthesis the co-precipitation of Fe^{2+}/Fe^{3+} ions is achieved after addition of hydroxide solution (NaOH, NH_4OH, etc.) [21–24]. During addition of base, strong pH gradient occurs, since mixing and homogenization proceeds relatively slow. This results in local in-homogeneities leading to the undesired local high supersaturations.

I have improved homogeneities of hydroxyl ions by using other precipitating agents like urea and $Mg(OH)_2$. It is known from the literature, that homogeneous release of hydroxyl ions can be achieved for example during the thermal hydrolysis of urea. However, the use of $Mg(OH)_2$ in spinel synthesis has not been reported before. In either case the precipitating agent was admixed into the aqueous solution of Fe^{3+}-urea and Fe^{2+} ions at 60 °C after initial γ-FeOOH phase formed due to thermal hydrolysis.

When urea was admixed, its thermal decomposition resulted in gradual release of hydroxyl ions. However, the kinetic of urea decomposition was too slow and consequently the pH required for Fe^{2+} ions precipitation was reached only after the γ-FeOOH in large extents already transformed to thermodynamically more stable α-FeOOH. α-FOOH phase once formed can only transform to the nonmagnetic α-Fe_2O_3 hematite [43].

To increase the rate of hydroxyl ions release and still retain their homogeneity, I have used $Mg(OH)_2$. $Mg(OH)_2$ displays relatively poor solubility of (0.001 g/100ml) at room temperature in comparison to NaOH (111g/100mL H_20) or NH_4OH otherwise used in spinel synthesis [21]. When solid $Mg(OH)_2$ was admixed its slow dissolution resulted in gradual release of hydroxyl ions, however, in higher rate in comparison to when urea was applied. The precipitated Fe^{2+} ions reacted with γ-FeOOH phase that resulted in its complete transformation to spinel according to the following chemical reaction.

$Fe^{2+}(aq) + Mg(OH)_2 \rightarrow Fe(OH)_2 + Mg^{2+}\,(aq)$
$2\gamma\text{-}FeOOH + Fe(OH)_2 \rightarrow Fe_3O_4 + 2H_2O$
$2Fe_3O_4 + ½\ O_2 \rightarrow 3\gamma\text{-}Fe_2O_3$

The formation of final spinel phase was confirmed with XRD and TEM analysis. Taking into the consideration the reaction conditions and inert atmosphere used, the first spinel phase formed was most likely cubic spinel magnetite (Fe_3O_4) that due to oxidation in air transforms to maghemite (γ-Fe_2O_3) [25]. The formation of magnetite phase in my experiments was indicated by the formation of black precipitate. After prolong air-

exposure the colour turned to dark brown which is typical for γ-Fe_2O_3 nanoparticles, when their size exceeds approximately 10 nm [2].

With additional studies, I have also demonstrated the temperature dependence on $Mg(OH)_2$ solubility and thus the rate of hydroxyl ions release. However, the temperature apart from $Mg(OH)_2$ solubility also affected the Fe^{3+}-urea decomposition rate and extent of thermal hydrolysis of Fe^{3+}. Here optimal reaction temperature, that resulted in sufficient control of hydroxyl ions release, desired for coating of spinel on the core nanoparticles was found to be 60 °C. At this temperature, the thermal treatment of the Fe precursor solution before the addition of $Mg(OH)_2$ resulted in the γ-FeOOH formation, whereas the addition of $Mg(OH)_2$ resulted in Fe^{2+} precipitation and formation of the spinel phase.

The spinel formed with the reaction of γ-FeOOH with precipitated Fe^{2+}. It is known that in dependence of γ-FeOOH solubility, the transformation of γ-FeOOH to spinel can proceed following different pathways. The solubility of γ-FeOOH phase decisively depends on the pH of reaction mixture and it strongly decrease in pH range between 4 and 10. Thus depending on the acidity of medium the γ-FeOOH-to-spinel transformation proceed with either dissolution-precipitation mechanism (pH < 4 or pH >10) or with *in situ* dehydration and local structural rearrangement (4 < pH < 10) [41, 81-82]. The solid transformation with structural rearrangement is initiated by the Fe^{2+} that with adsorption on surfaces initiates Fe-Fe electron transfer. Since in my experiments Fe^{2+} ions precipitated at conditions close to neutral pH I can conclude that the γ-FeOOH-to-spinel transformation proceeded with the dehydration and local structural rearrangement initiated by the precipitated Fe^{2+} ions. After complete γ-FeOOH-to-spinel transformation, the remained precursor is consumed for the particles growth.

Described mechanism is also favorable in terms of the heterogeneous nucleation. When heterogeneously nucleated γ-FeOOH phase on the core surfaces would form its transformation to spinel followed with subsequent growth would result in desired spinel coating.

In subsequent experiments I have used the above method to coat the spinel on the selected core nanoparticles. Apart from the reaction conditions tuned to obtain the spinel phase under conditions favoring low supersaturation, the kinetics of heterogeneous nucleation can also be influenced by the core nanoparticles properties. It is known, that the kinetic of nucleating phase can be affected by core particles crystal structure, size, size distribution and morphology (curvature of core nanoparticles) [27, 83]. Thus for the coating of the spinel, amorphous silica core nanoparticles and crystalline Ba hexaferrite nanoparticles of different size, size distribution and morphology were used as cores.

Special attention was given to the core nanoparticles colloidal stability. To ensure for example, the spinel layer formation controllably on the surfaces of the each core nanoparticle, the core nanoparticles were prepared in the form of stable aqueous suspension.

Colloidal stability of nanoparticles is often difficult to be achieved. The nanoparticles display large tendency for agglomeration due to the attractive van der Waals forces prevailing over electrostatic repulsive forces. Moreover, the magnetic BaM nanoparticles tend to agglomerate also due to attractive magnetic dipole-dipole interactions. In general the nanoparticles colloidal stability in water is achieved with particles high surface charge (in dependence of pH and ionic strength), while particles charge can be additionally enhanced by grafting charged molecules (alkyl carboxylic acids, alkyl amines, etc) [84–86] on their surfaces.

Silica core nanoparticles due to their large negative surface charge display colloidal stability in water at pH between 2 and 7 used for their coating with spinel. High positive

surface charge density of amorphous silica nanoparticles was assured with grafting of aminopropyl silane (APS) onto the silica surfaces. Thus, stable aqueous suspensions of amorphous silica core nanoparticles with positive and negative charge were obtained.

For the preparation of the Ba hexaferrite core nanoparticles (later referred to as BaM) I used hydrothermal synthesis. In dependence of the reaction conditions crystalline Ba hexaferrite nanoparticles of different size, size distribution and morphology were synthesized. Hydrothermal synthesis as wet-chemical method also enabled further preparation of the stable suspensions. The colloidal stability of larger BaM core nanoparticles is difficult to be achieved, due to the large tendency toward agglomeration resulting from strong magnetic dipole-dipole interactions. In products (BaM_{100} and $BaM_{30\text{-}70}$), particles colloidal stability in acidic medium was achieved based on their high positive surface charge density.

The surface charge density of the BaM nanoparticles was also increased with the adsorbed citric acid on the particles surface. For samples BaM_{10} and BaM_{100} a high negative zeta potential, caused by deprotonated carboxyl groups assured high negative zeta potential over large pH region and thus enabled particles' colloidal stability at the pH used for spinel coating.

To achieve spinel coating on the core surfaces, the spinel synthesis in subsequent reactions proceeded in the stable aqueous suspension of the core nanoparticles. Here it is desired, that the reaction conditions favor spinel formation as a single phase. Further it is also desired that the formation of spinel proceed selectively at the core surfaces following heterogeneous nucleation root.

In my studies the coating of spinel was first investigated by using amorphous silica core nanoparticles. In the literature there are several reports stressing the benefits of the core-shell nanoparticles where amorphous silica cores are coated with magnetic spinel shell. For example, when silica cores are dissolved in NaOH [87–89] or HF buffer solution [87], hollow magnetic spheres can be obtained. Hollow magnetic spinel spheres are advantageous in terms of acting as a multi-functionalize magnetic carriers [87, 89]. Already a hollow structure can hold drugs without any further modifications of its surface, however, their additionally functionalization can enable their applicability in anti-cancer hyperthermia and drug delivery systems [90, 92]. Up to now, large up to 300 nm sized hollow magnetic spheres were synthesized by the different methods including the integration of SiO_2 and spinel nanoparticles into anionic polymer, subsequently burned out by heat treatment at 500 °C [87, 90] or by using functionalized silica as a binder [72]. However, the coating of spinel on the silica core surfaces without any grafted functional group (-COOH, -SH, $-NH_2$) has not yet been reported.

The coating of spinel in my studies involved the use of amorphous silica core nanoparticles. Here, the formation of spinel shell along with the mechanism of its formation was investigated. The spinel synthesis proceeded in aqueous suspensions of silica core nanoparticles under the reaction conditions involving low supersaturation. First step in the synthesis comprise the formation of γ-FeOOH with the thermal hydrolysis of Fe^{3+} ions, released from decomposing Fe^{3+}-urea complex. Second, the addition of $Mg(OH)_2$ initiated the formation of Fe^{2+} precipitates that reacted with γ-FeOOH forming spinel. The homogeneity of the products ($S@SiO_2$-10) was investigated with TEM. The analysis revealed that the formed spinel phase was in the form of small 5–7 nm nanoparticles positioned exclusively on the surfaces of larger (~ 25 nm) silica cores. The spinel nanoparticles were present in large concentration and arranged uniformly. No homogeneously-nucleated nanoparticles were detected. The spinel coating was obtained also when oppositely charged silica core nanoparticles were used as cores. This excluded the possibility that the spinel nanoparticles would for example homogeneously nucleated

in the solution and only subsequently electrostatically adhere to the silica surfaces.

The coating of spinel on the silica surfaces has also been obtained by others [92]. However, the spinel coating was achieved after the formation of covalent bond between functionalized pre-synthesized spinel nanoparticles and functionalized silica core nanoparticles [92]. The spinel coating has also been achieved with electrostatic attraction of oppositely charged functional groups grafted on spinel and the silica nanoparticles surfaces [89, 92]. However, additional steps involving the synthesis of spinel nanoparticles and functionalization of the nanoparticles' surfaces are thus required. This often results in the partial agglomeration of the spinel nanoparticles before grafting to the silica surfaces. Partial agglomeration also limits the control of the grafting process thus typically non-uniform spinel coating is obtained [87, 90, 92].

Here, the method developed in my studies display several advantages. The formation of spinel layer proceeds regardless of the core surfaces charge, i.e. additional steps involving the functionalization of the core-nanoparticles surfaces can thus be omitted. Further, after nucleated nanoparticles with their subsequent growth come in direct contact, uniform layer of spinel phase is obtained.

However, the success of the spinel coating formation, involving heterogeneous nucleation root, relied upon the close control of the supersaturation of the nucleating phases. The final spinel phase is obtained only after chain of chemical reaction where γ-FeOOH phase reacted with Fe^{2+} precipitates.

Here I have also investigated the early stages of the reaction, to determine at what stage of chemical reaction the heterogeneous nucleation occurs. By investigated intermediate product, sampled at the end of Stage 1 (Figure 30), the TEM analysis revealed that already a short heated treatment (10 min) of Fe precursors dissolved into the silica core suspension resulted in the formation of small 3 nm nanoparticle of γ-FeOOH. The γ-FeOOH phase formed during thermal hydrolysis of Fe^{3+} ions solution. The γ-FeOOH nanoparticles were positioned exclusively on the silica core surfaces, while no homogeneously-nucleated nanoparticles were detected. After the addition of $Mg(OH)_2$, the precipitation of Fe^{2+} ions was initiated. The product sampled at the end of Stage 2 (Figure 31), revealed improved crystalline order and increased size (4–5 nm) of the nanoparticles on the silica surfaces. The nanoparticles on the silica surfaces were present in larger concentration. Here electron diffraction revealed the presence of two phases: cubic spinel and orthorhombic γ-FeOOH phase.

It is known, that the formation of spinel phase can proceed following two different paths: (i) with topotactic process, where incorporated Fe^{2+} ions cause the electron mobility bringing structural rearrangement [41, 25] or (ii) with dissolution-crystallization process initiated by surface adsorption of Fe^{2+} [25, 81, 82]. The formation of spinel after heat treatment (60 °C) of 3 nm γ-FeOOH nanoparticles in the solution of $FeSO_4$ and Na acetate (at pH = 9) was reported by Fu et.al.[43]. Here, authors suggested that the spinel synthesis proceeds following dissolution-crystallization path due to the increased final spinel nanoparticles size (22 nm). In my studies, however it is not possible to define the reaction path leading to spinel formation, although the smaller spinel size (final size is 7 nm) and decreased solubility of γ-FeOOH phase (at pH = 6) could suggests the topotactic transformation.

TEM examination also revealed the increased concentration of nucleated nanoparticles on silica surfaces. This indicates that along with the growth of formed spinel nanoparticles also the new nanoparticles can form following heterogeneous nucleation (Figure 57). The formation of new nanoparticles on the silica surfaces may proceed because after addition of $Mg(OH)_2$ the increased concentration of hydroxyl ions may result in higher supersaturation (at pH where Fe^{2+}/Fe^{3+} both ions precipitate). The literature state, that when higher supersaturation is established, the nucleating species

rather nucleate on the core nanoparticles of poor structural match while at lower saturation preferentially nucleation on core surfaces with strong interactions in good structural match is present [27]. This could also explain why at established higher supersaturation the new nanoparticles would nucleate on the silica surface, rather than material would be consumed for the growth of existing spinel nanoparticles.

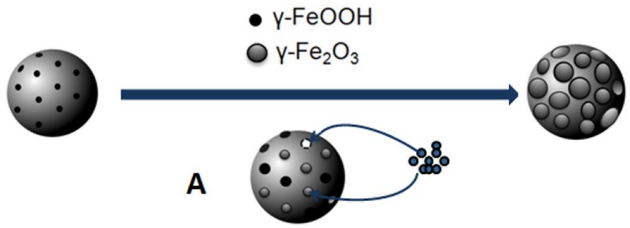

Figure 57: *The schematic of the spinel coating formation.*

Eventually γ-FeOOH-to-spinel transformation precedes completely resulting in final spinel phase on the silica surfaces.

Crucial step for the heterogeneous nucleation of γ-FeOOH that after transformation and growth resulted in final spinel coating was in the close control of its supersaturation, during the heat treatment of acidic Fe^{3+} ions solution. Already the data in the literature state the importance of the controlling of the reaction conditions of thermal hydrolysis. In dependence of the reaction temperature and ageing time, the formation of different Fe oxide hydroxide phases can be obtained [43, 44]. For example, the thermodynamics of α-FeOOH and γ-FeOOH phase during the thermal hydrolysis is size-driven. The enthalpy of formation for α-FeOOH (-561.5 $kJmol^{-1}$) is lower in respect to γ-FeOOH (-552.0 $kJmol^{-1}$) hence, the α-FeOOH is thermodynamically more stable. However, at very small particles size hydration enthalpy becomes the important parameter, due to the increased surface-to-volume ratio. Here the hydration enthalpy of γ-FeOOH is lower (0.4 Jm^{-2}) in comparison to that of α-FeOOH (0.6 Jm^{-2}), which increases its thermodynamic stability [43, 44]. It has been shown that at particles size of less than 5 nm γ-FeOOH is stable, while at increased size the transformation of γ-FeOOH to α-FeOOH proceeds.

However, to obtain the final spinel phase, it is necessary that the Fe oxide hydroxide phase, formed after thermally hydrolysis is γ-FeOOH. The thermal hydrolysis is characterized with rapid nucleation, however, subsequent growth proceeds very slowly [47–50]. For example, it may take hours or even days for particles to grow to the size of few tens of nm [50].

In my studies I have evaluated the effect of extend of the thermal hydrolysis during the synthesis of spinel coating on the silica surfaces. Here it was demonstrated that the process of thermal hydrolysis need to be closely controlled to achieve final spinel as the single-phase product.

Spinel formed selectively on silica surfaces only when the initial time of thermal hydrolysis was 10 min that resulted in the formation of 3 nm sized γ-FeOOH nanoparticles nucleated on the silica surfaces. When for example, the reaction time of thermal hydrolysis was prolonged to 60 min (S@SiO2-60), the TEM analysis revealed the formation of small 3–5 nm nanoparticles nucleated on silica surfaces. However, apart from γ-FeOOH phase also the α-FeOOH phase was detected. γ-FeOOH phase obviously partially transformed to thermodynamically more stable α-FeOOH phase, due to the increased nanoparticles growth. Consequently after addition of $Mg(OH)_2$, the precipitated

Fe^{2+} ions only reacted with γ-FeOOH phase, which resulted in excess of Fe^{2+} precipitates. The excess of Fe^{2+} precipitates reacted to form γ-FeOOH phase, however homogeneously in the solution, resulting in the formation of large sheet-like nanoparticles (Figure 36a). The formation of sheet-like γ-FeOOH nanoparticles from Fe^{2+} precipitates alone following the oxidation is consistent also with data in the literature [2].
After prolonging reaction time, the homogeneously formed γ-FeOOH phase transformed to more stable α-FeOOH phase, resulting in the formation of large rod-like nanoparticles.

Controlled heterogeneous nucleation of the γ-FeOOH phase was however found to be crucial for achieving final spinel coating. For example, when synthesis proceeds under reaction conditions where thermal hydrolysis is absent or less pronounced the γ-FeOOH phase did not form on the silica surfaces. Consequently the precipitation of Fe ions initiated with the addition of $Mg(OH)_2$ lead to the homogeneous nucleation that resulted in a formation of the spinel nanoparticles, however not on the silica surfaces (sample S@SiO2-0).

The spinel coating on the surface of amorphous silica core nanoparticles consists of randomly oriented discrete spinel nanoparticles. However, notable differences in the morphology of spinel coating were detected when crystalline Ba hexaferrites were used as the core nanoparticles.

Here, the crystal structure of Ba core nanoparticles, to some extend similar to the spinel structure directed the growth and thus the final morphology of spinel coating. The structures of spinel and hexaferrite were presented in the introduction (Chapter 1.2). Here it was shown, that in certain crystallographic directions, the Ba-hexaferrite structure exhibit similarity with spinel structure. Ba-hexaferrite structure can be presented as close-packed stacking of oxygen and barium ions with iron atom at interstitial positions. The hexaferrite structure divides in alternating S ($(Fe^{3+}_6O^{2-}_8)^{2+}$) and R ($(BaFe^{3+}_6O^{2-}_{11})^{2-}$) block. S block presents the cubic spinel structure in [111] direction, while R block represents hexagonal stacking of oxygen and barium. Further, the [10-10] direction of hexagonal structure Ba hexaferrite exhibit the same oxygen stacking as spinel in [110] direction [4].

When the Ba-hexaferrite nanoparticles were used as the core, the spinel layer was formed, on their surfaces. Here detailed TEM analysis revealed that the spinel layer formed preferentially on large surfaces of Ba-hexaferrite nanoparticles. This was determined with TEM analysis by examining nanocomposite particles oriented edge-on, with its large surfaces parallel to the electron beam. The spinel layer is uniform and completely covers the large surfaces of the Ba-hexaferrite core nanoparticle, symmetrically on both sides, forming sandwich-type nanostructure. Here detailed HREM analysis of the synthesized nanocomposite particles revealed that the spinel phase formed coherent interface with $(0001)_{HF} \parallel (111)_S$ and the epitaxial growth of spinel layer on the hexaferrite platelet nanoparticles. However, formation of spinel phase was not detected on side surfaces of hexaferrite core nanoparticles that are to some extend parallel with {01-10} prism planes. Preferential formation of the spinel layers detected only on the large faces of the hexaferrite core nanoparticles is related to similarity between the two structures. The large surfaces of the platelet Ba-hexaferrite core nanoparticle are parallel with the {0001} planes of their hexagonal structure, that exhibit the same oxygen stacking as {111} planes of cubic spinel. The structural matching of hexaferrite in <0001> and spinel in <111> zone is illustrated also in Figure 58.

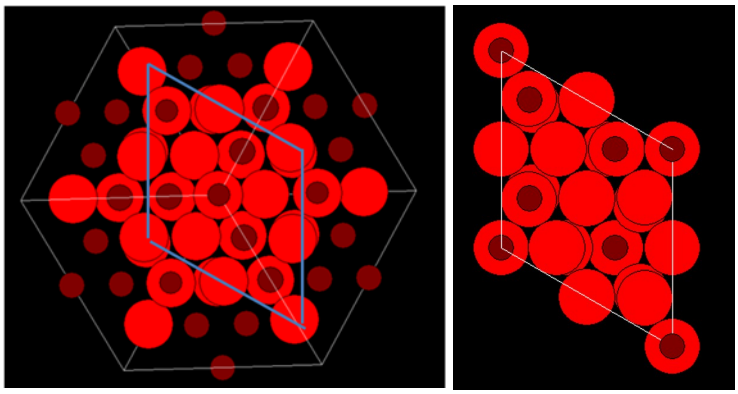

Figure 58: *Schematic of spinel in <111> zone and hexaferrite in <0001> zone.*

However, along particles thickness lower degree of structural match exist between hexaferrites and spinel. Here Ba hexaferrite structure can be divided into cubic S blocks and hexagonal R blocks (Figure 59). Despite perfect lattice match between hexagonal S block and spinel structure in <110> zone, the lattice mismatch between the hexagonal R block and spinel would result in the increased tensions, and increased interfacial energy. Due to the lower interfacial energy for $(0001)_{HF} \| (111)_S$ interface the spinel preferentially nucleated on the basal planes of the hexaferrite. Most likely during the synthesis, the heterogeneous nucleation of first initial phase proceeds on the whole surfaces of Ba hexaferrite core nanoparticles and only subsequently during crystallization of spinel, the material nucleated on side planes diffuse to the large hexaferrite surface.

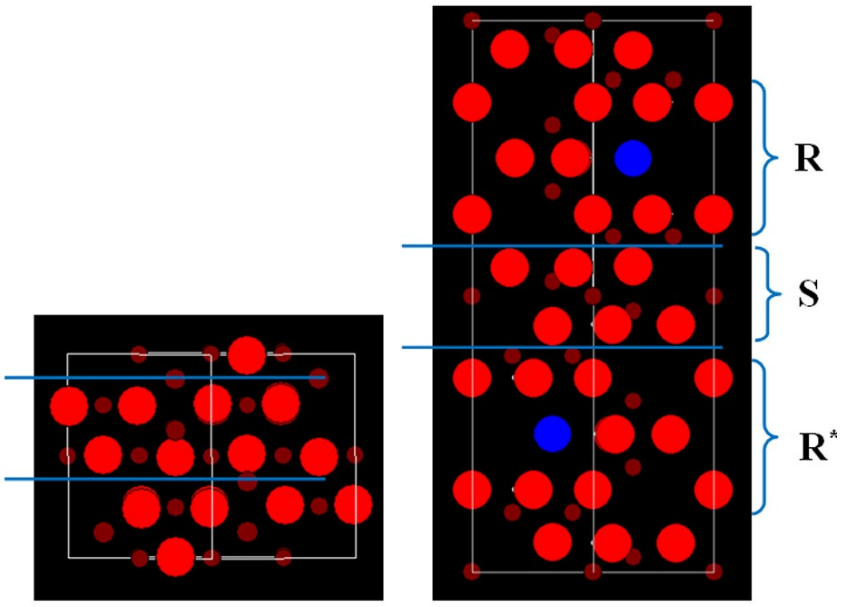

Figure 59: *Schematic of spinel in <110> zone and hexaferrite in <11-20> zone.*

Further, the anisotropic platelet Ba hexaferrite core nanoparticles also acted as a template directing the spinel growth. Thus spinel phase of anisotropic morphology were obtained. The preparation of highly anisotropic spinel nanoparticles would be interesting since the particles' shape significantly influences its properties [83]. Spinel however, due to its cubic structure predominantly forms the isotropic cubic or octahedral nanoparticles.

Apart from template-assisted growth, data in the literature comprises other strategies

for the synthesis of anisotropic spinel. For example, the synthesis of platelet spinel nanoparticles were obtained with disintegration of pre-synthesized hexaferrite nanoparticles [39]. Here the method involved the hydrothermal decomposition of hexaferrite in the presence of $NaHCO_3$ in reducing environment. The resulted platelet spinel nanoparticles formed after complete decomposition of hexaferrite. Here however, the spinel nanoparticles with isotropic globular or octahedral morphology were also detected. The as-synthesize platelet spinel nanoparticles after prolonging hydrothermal exposure and/or increased temperature re-shaped into more equilibrium isotropic shape. Only partial decomposition of hexaferrite resulted in the formation of spinel intergrown into hexaferrite matrix. The formation of particles containing intergrown of spinel and hexaferrite can also be prepared with thermal treatment of mixed Ba and Fe precursors. For example, Sudaker et. all. used wet-chemical gel-to-crystallite conversion, for the synthesis of Ba-hexaferrite-Ni-ferrite intergrown particles, of the size over 100 nm. Here the spinel layers were randomly intergrown into M-hexaferrite matrix, while spinel S block varied in dependence of the spinel ferrite content.

My results have also demonstrated that the spinel coating significantly depends also on the core nanoparticles size, morphology, their crystalline order and availability of core nanoparticles for nucleating species through reaction vessel. For example when the size of the selected core nanoparticles was larger ($BaM_{30\text{-}70}$) the availability of core surfaces through the reaction vessel was reduced. In particular, the numerical concentration of Ba-hexaferrite in the sample $BaM_{30\text{-}70}$ was for the order of magnitude lower than in the sample $S@BaM_{10\text{-}70}$ where $BaM_{10\text{-}70}$ were used as cores although the net surface area remained approximately the same. Lower availability of core nanoparticles reflected in the shape of synthesized nanocomposite particles. Here the variations of the spinel layer thickness between nanocomposite particles were detected. Also the spinel layers of individual nanocomposite particles were not always symmetric. Further, apart from the formation of the spinel coating here also the homogeneously nucleated nanoparticles were detected. The presence of homogeneously nucleated particles and changes of nanocomposite particles morphology can be attributed to lower concentration of core nanoparticles. It can also be attributed to the reduced colloidal stability of core nanoparticles. $BaM_{30\text{-}70}$ already shows hard-magnetic properties and thus nanoparticles already partially agglomerate due to the strong magnetic interactions [94, 37].

When the Ba hexaferrite nanoparticles with the average size up to 70 nm were used as core nanoparticles the formed spinel layers were uniform and homogeneous. However, when larger Ba-hexaferrite core nanoparticles were used (>100 nm) the spinel layer formed after separate nucleation on the core surfaces. After the growth these nanoparticles came in contact and formed spinel layer. The growth of these island varied which resulted in the appearance of rougher surfaces.

Entirely different behaviour was observed when small BaM_{10} discoid nanoparticles were used as core. Here, the results showed that during the reaction of spinel coating Fe-species that nucleated on the core surfaces reacted with Ba hexaferrite core nanoparticles. The small Ba hexaferrite discoids obviously showed higher reactivity toward nucleated species than larger core nanoparticles. This might be related to the relatively small particles size, especially their small thickness that corresponds to less than two repetitions of the hexagonal unit cell along c-direction [37, 38]. The reason for the higher reactivity of small BaM discoids can thus be in large extend ascribed to the larger proportion of incompletely coordinated surface atoms and also possible structural tension, as a result of particles small size.

The product particle also appeared more isotropic in comparison to the anisotropic discoid Ba hexaferrite core nanoparticle. Generally Ba hexaferrite nanoparticles grow

preferentially in a-b direction of hexagonal unit cell, which results in the particles' platelet morphology. Preferential growth is a consequence of the energy differences for the formation of side prism planes {10-10} and basal planes {0001}. Here, product nanoparticles of the sample S@BaM_{10} show more isotropic particles shape, indicating that the nucleated material, although most likely nucleated on whole particles surfaces, preferentially grew on large surfaces of core nanoparticles. The HREM image of product S@BaM_{10} obtained after reaction between BaM_{10} core nanoparticles also shows reduced dominant periodicity (9.5Å) along particles thickness, in comparison to the dominant periodicity of (0002) planes in hexaferrite (11.5 Å). Also EDXS analysis showed reduced content of Ba and increase in Fe. Here for example, the combination of chemical composition and HREM analysis does not match any of the known mix–layered hexagonal ferrites [8] or any other known compound. The product particles can thus be viewed as a new compound.

The nanocomposite particles S@BaM consisting of different hard-soft hexaferrite-spinel magnetic phases are especially interesting due to their magnetic properties. The synergy of two magnetically-different phases together with possible magnetic coupling can induce improved magnetic properties. Typically spinel iron oxide exhibit soft magnetic properties, with high saturation magnetization (bulk saturation magnetization 86 Am^2/kg). Additionally, the magnetic properties are size-dependent. When particles' size decreased below approximately 20 nm the magnetic moment relaxes due to the thermal energy [3] thus spinel nanoparticles display superparamagnetic properties. The superparamagnetic behaviours of spinel nanoparticles, is for some application favoured since it enables the preparation of relatively concentrated stable suspensions, i.e. ferrofluids. As such, spinel iron oxide (γ-Fe_2O_3) has been found as non-toxic material and is thus been subjected to the extensive research in the field of modern medical application [6]. Spinel nanoparticles in the form of ferrofluids have been extensively studied for the contrast enhancement in magnetic resonance imaging and as active constituents of drug delivery platforms. However, as mediators for magnetic hyperthermia the spinel iron oxide shows only moderate heating capacities, which limits their application [95]. It has been suggested in the literature that particularly the nanocomposites based on magnetically different phases, for example hard-soft hexaferrite-spinel ferrites would exhibit optimal magnetic properties for the magnetic fluid hyperthermia [95, 96]. This is due to the important differences in their magnetic anisotropies, where K_1 (γ-Fe_2O_3) = - ~ 10^3 Jm^{-3} and K_1 ($MFe_{12}O_{19}$, M= Ba, Sr) = ~ 10^6 Jm^{-3} [96]. The combined contribution of the magnetically different phases would enable to adjust the coercivity and the remanence to obtain the optimal shape of the hysteresis loop for the applications in the magnetic hyperthermia.

The magnetic properties of S@BaM nanocomposite particles, synthesized in my work shows notable differences in the magnetic properties in comparison to the untreated BaM core nanoparticles. In all the analyzed nanocomposite products (S@BaM_{10}, S@$BaM_{10\text{-}70}$, S@BaM_{100}) the magnetic hysteresis revealed significant increase in the saturation magnetization (measured at 1T) due to the presence of soft magnetic spinel phase. In the samples S@$BaM_{10\text{-}70}$ and S@BaM_{100} also the decrease in the coercivity is detected. Further, the shape of the hysteresis loops shows coherent switching of the phases, which suggests the coupling between magnetic moments of both phases.

The presence of the exchange coupling interaction is important because coupling of the magnetic moments of magnetically-different phases can result in the significant improvement of their magnetic properties, especially their energy products $|BH|$. It has been suggested in the literature that binary systems consisting of hard-magnetic phase, coated with soft-magnetic spinel could override the difficulties following the

miniaturization of spinel phase and improve the energy product [9, 8, 97]. Here for example, it has been demonstrated that when spinel iron oxide are introduced into the assembly of equally sized nanoparticles of hard-magnetic FePt phase, the heat treatment results in the FePt-Fe_3Pt nanocomposite exhibit very large energy product (20 MGOe) due to the exchange-coupling interactions [98].

It is known that for the exchange-coupling to be efficient, both hard and soft phase need to be controlled at nanoscale [98–103]. Further it is necessary that the magnetic phases (hard and soft) are intergrown. The HREM analysis of products particles S@$BaM_{10\text{-}70}$ and S@BaM_{100}, synthesized in my work revealed that the spinel phase grew epitaxially on the surface of the hexaferrite BaM core nanoparticles, forming the coherent interface. Further the magnetic measurements revealed the coherent switching of the magnetization in the reverse field that is typically observed in exchange-spring magnets [103], while also small decrease in coercivity and large increase in the remanent magnetization is observed. According to Stoner-Wohlfahrt theory the increase in the remanence over *Ms*/2 (*Ms* is saturation magnetization) can be due to the preferred alignment of nanoparticle or a result of the exchange-coupling interaction [103]. In my product S@BaM_{100} nanocomposite particles, the increase in the remanence can either be attributed to the particles platelet morphology and thus preferential orientation or the exchange interactions. Thus in my work, the magnetic hysteresis of product S@BaM_{100} nanocomposite particles forming magnetically-oriented assembly were compared to the hysteresis of the magnetically-oriented assembly of the untreated BaM_{100} core nanoparticles. The comparison of both in-plane hysteresis loops revealed the increase in the remanence for 35%. Apart from high remanence the VSM measurements of product S@BaM_{100} nanocomposite particles also revealed high coercivity (Figure 54) and improved energy product for over 50%.

6 Conclusions

This thesis covers the studies related to the synthesis of magnetic iron oxide coatings developed with the aim to prepare multiphase bimagnetic or multifunctional nanocomposite particles. The iron oxide coatings (referred as spinel coating) on the surfaces of different colloidal core nanoparticles were synthesized with coprecipitation of Fe^{2+}/Fe^{3+} ions. The controlled precipitation and condensation of Fe^{2+}/Fe^{3+} ions required for the heterogeneous nucleation and thus formation of spinel coating was achieved with close control of the reaction conditions. Spinel coating was only achieved when the kinetics of the initial phase formed were closely controlled. Further, the reactants concentration needs to be kept low while their homogeneity throughout the reaction vessel has to be assured.

In the first part of my thesis I have studied the synthesis of spinel iron oxide homogeneously in the solution under conditions involving low supersaturation of nucleating species. Low supersaturation was achieved with slow and homogeneous release of Fe^{3+} and hydroxyl ions. Thus I have immobilized highly reactive Fe^{3+} ions into a urea complex while slow and homogeneous precipitation of Fe^{2+} ions was achieved after using urea or $Mg(OH)_2$ as the precipitating agent. Here, I came to the following conclusions:

1. Slow and homogeneous release of Fe^{3+} ions from Fe^{3+}- urea complex can be achieved during thermal treatment of aqueous solution of Fe^{3+}- urea complex at temperatures above 50 °C. If temperature exceeds 60 °C the formation of Fe oxide hydroxide of different crystallographic modifications form in sequences due to the thermal hydrolysis. First γ-FeOOH phase forms while at prolong exposure at temperature the γ-FeOOH → α-FeOOH transformation was observed.
2. The formed γ-FeOOH phase transformed to the final spinel phase when it reacted with the precipitated Fe^{2+} ions. If α-FeOOH phase formed, it transformed only to the undesired non-magnetic α-Fe_2O_3 phase.
3. The homogeneous precipitation of Fe^{2+} ions was achieved with slow and gradual releases of hydroxyl ions from the precipitating agents (urea or $Mg(OH)_2$). The optimal rate of the hydroxyl ions release was obtained only when $Mg(OH)_2$ was used as the precipitating agent. In a later case the precipitated Fe^{2+} ions reacted with formed γ-FeOOH phase, resulting in its complete transformation into spinel.
4. The reaction temperature influences several processes: the decomposition rate of the Fe^{3+}- urea complex, the solubility of the $Mg(OH)_2$ and the rate of the thermal hydrolysis. It has been found that optimal reaction temperature for the controlled spinel formation favoring heterogeneous nucleation can be achieved at 60 °C.

Apart from the level of the supersaturation, nucleation kinetics is also influenced by properties of the core nanoparticles. Amorphous silica nanoparticles and Ba-hexaferrite nanoparticles of different sizes were used as the core nanoparticles. The core nanoparticles were dispersed in the reaction mixture. The colloidal stability of the suspension was achieved using high density surface charge enhanced also by grafting nanoparticles surfaces with charged functional groups.

In the second part of my thesis I have studied the spinel coating synthesis following the above-mentioned root where spinel was synthesized under conditions of low supersaturation involving heterogeneous nucleation. The spinel coating synthesis proceeded in stable aqueous suspensions of silica core nanoparticles. The first step of the synthesis comprised the formation of Fe oxide hydroxide phase with thermal hydrolysis of Fe^{3+} ions released from the Fe^{3+}-urea complex. Second, the addition of $Mg(OH)_2$ initiated the precipitation of Fe^{2+} ions that reacted with Fe oxide hydroxide resulting in the spinel formation. Here the reaction conditions play a significant role on the final phase formation and on the nucleation (homogeneous/heterogeneous) regime. After systematic studies, I came to the following conclusions:

1. The selective spinel nanoparticle formation on the surface of the core nanoparticles was achieved only when time interval of thermal hydrolysis at 60 °C (TH) was 10 min. Under these conditions, the TH of Fe^{3+} ions resulted in the formation of small 3 nm γ-FeOOH nanoparticles on silica surfaces. After the addition of $Mg(OH)_2$ the complete γ-FeOOH → spinel transformation resulted in spinel coating formation. The spinel coating consisted of dense packing of a 7 nm randomly-oriented spinel particle
2. The surface charge of the core nanoparticles had no influence on the formation of the spinel coating. This confirms that the spinel phase formed at the surfaces of the core nanoparticles with heterogeneous nucleation and not by electrostatic attractions of the homogeneously-nucleated nanoparticles in the suspension.
3. When the time interval of the initial TH was prolonged to 60 min the γ-FeOOH phase on silica-core surfaces formed after TH of Fe^{3+} ions already partially transformed to the undesired α-FeOOH phase. As a result, the final product apart from spinel contained also non-magnetic α-Fe_2O_3 phase.
4. When the synthesis proceeded under conditions where thermal hydrolysis was less pronounced or even absent, spinel phase homogeneously nucleated and thus spinel coating did not form.

The spinel was also coated onto the surfaces of platelet crystalline Ba-hexaferrite nanoparticles of different size, size distribution and morphology. Unlike when amorphous silica spheres were used as the core and spinel phase was formed as randomly oriented discrete nanoparticles, here the Ba hexaferrite with its crystal structure influenced the growth of the spinel phase. I found that:

1. When platelet crystalline Ba hexaferrite nanoparticles were used as core, the uniform and homogeneous spinel (S) layers were obtained on the hexaferrite (HF) basal planes. The spinel layer grew epitaxially forming coherent interface with $(0001)_{HF} \parallel (111)_S$. This was due to the structural similarities since $\{111\}_S$ planes exhibit the same oxygen stacking as $\{0001\}_{HF}$ planes. No spinel was formed on the side faces of the core nanoparticles, due to the lattice mismatch. This resulted in the observed sandwich-type morphology of the synthesized nanocomposite.
2. The uniform spinel layer on platelet Ba-hexaferrite core nanoparticles was synthesized only when the estimated diameter of platelet core nanoparticles was in the range between 10–70 nm. When larger Ba hexaferrite core nanoparticles were used (> 100 nm), the spinel layers formed after nucleation at several points at the core surfaces. After the growth these islands came into the contact resulting in the increased roughness of the coating.
3. When small Ba-hexaferrite discoid nanoparticles were used as the core nanoparticles, the precipitated Fe species reacted with the core nanoparticles that resulted in the formation of the product nanoparticles that differed in the

composition and structure to any known compound. Thus the formed particles can be viewed as a new compound stable only in the form of nanoparticles.

In nanocomposite particles where hard-magnetic platelet hexaferrite core was coated with uniform layer of spinel shell the improved magnetic properties were obtained in comparison to the magnetic properties of the untreated Ba hexaferrite core nanoparticles. I found that:

1. For the Ba hexaferrite core nanoparticles that were in or close to the superparamagnetic state, the presence of soft magnetic spinel phase resulted in higher magnetization.
2. For Ba-hexaferrite core nanoparticles that exhibited single-domain ferrimagnetic properties, the formation of spinel layer resulted in the increase in remanence and magnetization, while coercivity slightly decreased. The increase in the remanence can be attributed to the preferred alignment or the exchange-spring interaction. The presence of exchange-spring interaction was also indicated with coherent magnetization reversal in nanocomposite particles magnetic hysteresis.
3. The comparison of the magnetic hysteresis of nanocomposite particles to untreated hexaferrite core reveals the increase in the remanence for 35 %, while the energy product $|BH|_{MAX}$ increased for 53%.

The method for magnetic spinel coating, developed in my studies, has proved to be efficient and simple and thus promising to be widely applied for coating of other materials of versatile functionalities. Thus, different multifunctional (bimagnetic, magneto-ferroelectric, magneto-photocatalytic, etc.) nanocomposite materials can be synthesized.

7 Acknowledgements

I would like to thank my supervisor Asst. Prof. Dr. Darja Lisjak, for her guidance, encouragement and support during my Ph.D. work.

I would especially like to thank to Prof. Dr. Darko Makovec for his expert guidance, valuable discussions and suggestion related to my work.

I also thank to Dr. Marko Jagodič from Institute for Mathematics, Physics and Mechanics for his help and valuable discussions related to magnetic measurements.

I would also like to thank my colleagues in the Department of the Materials Synthesis and all other friends from Jožef Stefan Institute for all the support and nice moments that we have spent together in last five years.

Finally, I would deeply like to thank my family and my brother for all the moral support and encouragement during my years of study. Thank also too all my friends for support, and strength and for all the unforgettable moments we shared together.

8 References

[1] Cullity, B. D.; Graham, C. D. *Introduction to Magnetic Materials* (John Wiley & Sons, New Jersey, 2009).

[2] Cornell, R. M.; Schwertmann, U. *The Iron Oxide: Structure, Properties, Reactions, Occurrences and Uses* (Wiley-VCH Verlag GmbH & Co., Weinheim, 2003).

[3] Jiles, D. *Introduction to Magnetism and Magnetic Materials* (Champman & Hall, London, 1998).

[4] Smit, J.; Wijn, H. P. J. *Ferrites: Physical properties of ferrimagnetic oxides in relation to their technical applications* (N. V. Philips' Gloeilamenfabrieken, Eindhoven, 1959).

[5] Coey, J. M. D. Permanent magnetism. Solid State Communications **102**, 101–105 (1997).

[6] Than, N. T. K. *Magnetic nanoparticles, from fabrication to clinical applications* (CRS Press, London, 2012).

[5] Leslie-Pelecky, D. L.; Rieke, R. D. Magnetic properties of nanostructured materials. C*hemistry of materials* **8**, 1770 (1996).

[6] Odenbach, S. *Magnetoviscous effects in ferrofuids* (Springer, Berlin, 2002).

[7] Pollert, E. Crystal Chemistry of magnetic oxides part 2: Hexagonal ferrites. *Progress in Crystal Crowth and Characterization* **11**, 155 (1985).

[8] Pullar, R. C. Hexagonal ferrites: A review of the synthesis, properties and applications of hexaferrite ceramics. *Progress in Materials Science* **57**, 1191–1334 (2012).

[9] Chin, A. B.; Yaacob, I. I. Synthesis and characterization of magnetic iron oxide nanoaprtiocles via w/o microemulsion and Massart's procedure. *Journal of Materials processing technologies* **191**, 235–237 (2007).

[10] Kim, E. H.; Lee, H. S.; Kwak, B. K.; Kim, B. K. Synthesis of ferrofluid with magnetic nanoparticles by sonochemical method for MRI contrast agent. *Journal of magnetism and magnetic materials* **289**, 328 (2005).

[11] Daou, T. J.; Pourroy, G.; Bégin-Colin, S. ; Greneche, J. M.; Ulhaq-Bouillet, C.; Legaré, P.; Bernhardt, P.; Leuvrey, C.; Rogez, G Hydrothermal synthesis of monodispersed magnetite nanoparticles. C*hemistry of materials* **18**, 4399 (2006).

[12] Yan, J.; Mo, S.; Nie, J.; Chen, W.; Shen, X.; Hu, J.; Hao, G.; Tong, H. Hydrothermal synthesis of monodisperse Fe_3O_4 nanoparticles based on modulation of tartaric acid. *Colliods and Surfaces A: Physicochemical and Engineering Aspects* **340**, 109 (2009).

[13] Li, Z.; Chen, H.; Bao, H.; Gao, M. One-pot reaction to synthesize water-soluble magnetite nanocrystals. *Chemistry of Materials* **16**, 1391 (2004).

[14] Sun, S.; Zeng, H. Size-controlled synthesis of magnetite nanoparticles. *Journal of American Chemical Society* **124**, 8204 (2002).

[15] Hyeon, T.; Lee, S. S.; Park, J.; Chung, Y.; Na, H. B. Synthesis of highly crystalline and monodispersed maghemite nanocrystallites without a size selection process. *Journal of American Chemical Society* **124**, 12798 (2001).

[16] Alvarez, G. S.; Muhammed, M.; Zagorodni, A. A. Novel flow injections synthesis of iron

oxide nanoparticles with narrow size distribution. *Chemical Engineering Science* **61**, 4625 (2006).

[17] Sjogren, C. E.; Johansson, C.; Naevestad, A.; Sontum, P. C.; BrileySaebo, K.; Fahlvik, A. K. Crystal size and properties of superparamagnetic iron oxide particles. *Magnetic Resonance Imaging* **15**, 55 (1997).

[18] Babes, L.; Denizot, B.; Tanguy, G.; Le Jeune, J. J.; Jallet, P. J. Synthesis of iron oxide nanoparticles used as MRI contrast agents: A parametric study. *Journal of colloid and interface science* **212**, 474 (1999).

[19] Košak, A. *Disertacija: Sinteza in karakterizacija feritnih nanodelcev in priprava magnetnih tekočin* (Univerza v Mariboru, Maribor, 2006).

[20] Tronc, E.; Bellaville, P.; Jolivet, J.-P.; Livage, J. Transformation of ferric hydroxide into spinel by Fe^{II} adsorption. *Lungmuir* **8**, 813 (1992).

[21] Bellaville, P.; Jolivet, J.-P.; Tronc, E.; Livage, J. Crystalization of ferric hydroxide into spinel by adsorption on colloidal magnetite. *Journal of Colloid and Interface Science* **150**, 453 (1992).

[22] Massart, R. Preparation of aqueous magnetic liquids in alkaline and acidic media. *IEEE Transactions on Magnetics* **17**, 1247 (1981).

[23] Mohapatra, S.; Pramanik, N.; Mukherjee, S.; Ghosh, S. K.; Pramanik, P. A simple synthesis of amine-derived superparamagnetic iron oxide nanoparticles for bioapplications. *Journal of Materilas Science* **42**, 7566 (2007).

[24] Lee, J.; Isobe, T.; Senna, M. Preparation of ultrafine Fe_3O_4 particles by precipitation in the presence of PVA at high pH. *Journal of Colloid and Interface Science* **177**, 490 (1996).

[25] Jolivet, J.-P. *Metal Oxide Chemistry and Synthesis: From Solution to Solid State* (John Wiley & Sons, Chichester, 1994).

[26] Ivan Sondi, I.; Goia D. V.; Matijević, E. Preparation of highly concentrated stable dispersions of uniform silver nanoparticles. *Journal of Colloid and Interface Science* **260,** 75–81 (2003).

[27] Sato, K.; Nakajima, K.; Furukawa, Y. *Advances in crystal growth research* (Elsevier science, Amsterdam, 2001).

[26] Kralj, S.; Makovec, D.; Čampelj, S.; Drofenik, M. Producing ultra-thin silica coatings on iron-oxide nanoparticles to improve their surface reactivity. *Journal of Magnetism and Magnetic Materials* **322**, 1847 (2010).

[27] Čampelj, S.; Makovec, D.; Drofenik, M. Functionalization of magnetic nanoparticles with 3-aminopropyl silane. *Journal of magnetism and magnetic materials* **321**, 1346 (2009).

[28] Pogh, R.; Bergstrom, L. *Surface and colloidal chemistry in advanced ceramic processing* (Marcel Dekker Inc., New York 1994).

[29] Israelachvili, J. N. *Intermolecular and surfaces forces: With applications to colloidal and biological systems* (Academic Press Inc., London, 1985).

[30] Liang,Y.; Hilal,N.; Langston, P.; Starov, V. Interaction forces between colloidal particles in liquid: Theory and experiment. *Advanced colloid and interface science* **134,** 151 (2007).

[31] Porter, M.; *Handbook of surfactants* (Imprint of Chapman & Hall, Glasgow, 1994).

[32] Rosen, M. J. *Surfactants and interfacial phenomena* (John Wiley and Sons, New Jersey, 2004).

[33] Coey, J. M. D. Hard Magnetic Materials: A Perspective, *IEEE transactions on magnetic* 47, 4671 (2011).

[34] Pankhurst, Q. A.; Connolly, J.; Jones, S. K.; Dobson, J. Applications of magnetic nanoparticles in biomedicine. *Journal of applied physics* **36**, 167 (2003).

[35] Asuha, S.; Zhao, S.; Jin, X. M.; Hai, M. M.; Bao, H. P. Effects of synthetic routes of Fe–urea complex on the synthesis of γ-Fe_2O_3 nanopowder. *Applied Surface Science* **255**, 8897–8901 (2009).

[36] Kralj,S.; Drofenik. M.; Makovec, D. Controlled surface functionalization of silica coated magnetic nanoparticles with thermal amino and carboxyl groups. *Journal of Nanoparticle Research* **13**, 2829 (2011).

[37] Primc, D.; Makovec, D.; Lisjak, D.; Drofenik, M. Hydrothermal synthesis of ultrafine barium hexaferrite nanoparticles and the preparation of their stable suspensions. *Nanotechnology* **20**, 315605 (2009).

[38] Makovec, D. et al. Structural propeties of ultrafine Ba-hexaferrite nanoparticles. *Journal of solid state chemistry* **196**, 67–71 (2012).

[39] Makovec, D. et al. Structural properties of ultrafine Ba-hexaferrite nanoparticles. *Journal of Solid State Chemistry* **196**, 67–71 (2012).

[40] Schwertmann, U.; Friedl, J.; Stanjek, H. From Fe(III) ions to ferrydrite and to hematite. *Journal of Colloid and Interface Science* **209**, 215–223 (1999).

[41] Cudennec, Y.; Lecerf, A. Topotactic transformation of goethite and lepidocrocite into hematite and maghemite. *Solid State Sciences* **7**, 520–529 (2005).

[42] Filutowicz, Z.; Lukaszewski, K.; Pieszynski, K. Remarks on spectra-photometric monitoring of urea in dialysate. *Journal of medical informatics and technologies* **8**, 1642–6037 (2004).

[43] Fu, D.; Keech, P. G.; Sun, X.; Wren, C. J. Iron oxyhydroxide nanoparticles formed b forced hydrolysis: dependence of phase composition on solution concentration. *Physical Chemistry Chemical Physic* **13**, 18523–18529 (2011).

[44] Nevrtosky, A.; Mazeina, L.; Majzlan, J. Size-driven structural and thermodynamic complexity in iron oxides. *Science* **319**, 1635–1638 (2008).

[45] Carlson, L.; Schwertmann, U. The effect of CO_2 and oxidation rate of the formation of goethite versus lepidocrocite from an Fe(II) system at pH 6 and 7. *Clay Minerals* **25**, 65–71 (1990).

[46] Greenwood, N. N.; Ernshaw, A. *Chemistry of the Elements* (Elsevier, Oxford, 2006).

[47] Bailey, J. K.; Brinker, C. J.; Mecartney, M. L. Growth mechanism of iron oxide particles of differing morphologies from forced hydrolysis of ferric chloride solution. *Journal of Colloid and interface science* **157**, 1–13 (1993).

[48] Compean-Jasso, M. E.; Ruiz, F.; Martinez, J. R.; Herrera-Gomez, A. Magnetic properties of magnetite nanoparticles synthesized by forced hydrolysis. *Materials Letters* **62**, 4248–4250 (2008).

[49] Mucić, S.; Krehula, S.; Popović, S.; Skoko, Ž. Some factors influencing forced hydrolysis of $FeCl_3$ solution. *Materials Letters* **57**, 1096–1102 (2003).

[50] Mayer, W. R.; Pulcinelli, S. H.; Santilli, C. V.; Craievich, A. F. Formation of colloidal particles of hydrous iron oxide by forced hydrolysis. *Journal of non-crystalline solids* **273**, 41–47 (2000).

[51] Majzlan, J.; Grevel, K. D.; Nevrotsky, A. Thermodynamics of Fe oxides: Part II. Entalpies of formation and relative stability of goethite (α-FeOOH), lepidocrocite (γ-FeOOH), and maghemite (γ-Fe_2O_3). *American mineralogist* **88**, 855–859 (2003).

[52] Majzlan, J.; Lang, B. E.; Stevens, R.; Nevrotsky, A. Thermodynamics of Fe oxides: Part I: Entropy at standard temperature and pressure and heat capacity of goethite (α-FeOOH),

lepidocrocite (γ-FeOOH), and maghemite (γ-Fe_2O_3). *American mineralogist* **88**, 846–854 (2003).

[53] Lisjak, D.; Drofenik, M. Chemical substitution- An alternative strategy for controlling the particles size of barium ferrite. *Crystal growth and design* **12**, 5174–5179 (2012).

[54] Drofeni, M. The concept of a low-temperature synthesis for superparamagnetic $BaFe_{12}O_{19}$ particles. *Journal of American Ceramic Society* **93**, 1602–1607 (2010).

[55] Primc, D.; Drofenik, M; Makovec, D. Low-temperature hydrothermal synthesi of ultrafine Sr hexaferrite nanoparticles. *European journal of inorganic chemistry* **25**, 3802–3809 (2011).

[56] Sudakar, C.; Subbanna, G. N.; Kutty, T. N. R. Nanoparticle composite having structural intergrowths of hexaferrite and spinel ferrites prepared by gel-to crystallite conversion and their magnetic properties. *Journal of magnetism and magnetic materials* **268**, 75–88 (2004).

[57] Makovec, D.; Drofenik, M. Synthesis of plate-like spinel particles and spinel-hexaferrite nanocomposite particles using hydrothermal decomposition of Ba hexaferrite. *Crystal growth and design* **8**, 2182–2186 (2008).

[59] Topal, U. Improvement of the remanence properties and the weakening of interparticle interactions in BaFe12O19 particles by B2O3 addition. *Physica B* **407**, 2058–2062 (2012).

[60] Shen, X.Shape Anisotropy, exchange-coupling interactions and microwave absorption of Hard/soft nanocomposites ferrite microfibers. *Journal of American ceramic society* **95**, 3863–3870 (2012).

[61] Kocbek, P.; Obermajer, N.; Cegnar, M.; Kos, J.; Kristl, J. Targeting cancer cells using PLGA nanoparticles surface modified with monoclonal antibody. *Journal of Controlled Release* **120**, 18 (2007).

[62] Goetze, T.; Gansau, C.; Buske, N.; Roeder, M.; Görnert, P.; Bahr, M. Biocompatible magnetic core/shell nanoparticles. *Journal of Magnetism and Magnetic Materials* **252**, 399 (2002).

[63] Jordan, A.; Wust, P.; Scholz, R.; Tesche, B.; Fahling, H.; Mitrovics, T.; Vogl, T.; Cervos-Navarro, J.; Felix, R. Cellular uptake of magnetic fluid particles and their effects on human adenocarcinoma cells exposed to AC magnetic fields in vitro. *International Journal of Hyperthermia* **12**, 705 (1996).

[64] Chertok, B.; Moffat, B. A.; David, A. E.; Yu, F.; Bergemann, C.; Ross, B. D.; Yang, V. C. Iron oxide nanoparticles as a drug delivery vehicle for MRI monitored magnetic targeting of brains tumors. *Biomaterials* **29**, 487 (2008).

[65] Arbab, A. S.; Yocum, G. T.; Kalish, H.; Jordan, E. K.; Anderson, S. A.; Khakoo, A. Y.; Read, E. J.; Frank, J. A. Efficient magnetic cell labeling with protamine sulfate complexed to ferumoxides for cellular MRI. *Blood* **104**, 1217 (2004).

[66] Gupta, A. K.; Gupta, M. Synthesis and surface engineering of iron oxide nanoparticles for biomedical applications. *Biomaterials* **26**, 3995 (2005).

[67] Xu, Z.; Hou, Y.; Sun, S.; Magnetic core/shell Fe3O4 and Fe3O4/Au/Ag nanoparticles with tunable plasmatic propertied. *Journal of American chemical society* **129**, 8698–8699 (2007).

[68] Teranishi, T. et al. Conversion of anisotropically phase-segregated Pd/γ-Fe2O3 nanoaprticles into exchange coupled fct-FePd/α-Fe nanocomposite particles. *Journal of American chemical society* **130**, 4210–4211 (2008).

[69] Yu, H. et al, Dumbbell-like bifunctional Au-Fe3O4 nanoparticles. *Nano Letters* **5**, 379–382 (2005).

[70] Teng, X.; Black, D.; Watkins, N. J.; Gao, Y.; Yang, Honh. Platinum-maghemite core-shell nanoparticles using a sequential synthesis. *Nano letters* **3**, 261–264 (2003).

[71] Zhang,, G.; Liao, Y.; Baker, I.; Surface engineering of core-shell iron/iron oxide

nanoparticles for microemulsions for hyperthermia. *Materials science and Engineering* **30**, 92–97 (2010).

[72] Masala, O. et al, Preparation of magnetic spinel ferrite core/shell nanoparticles: soft ferrites on hard ferrite and vice versa. *Solid State Science* **8**, 1015–1022 (2006).

[73] Simeonidis, K. et al. Structural and magnetic features of heterogeneously nucleated Fe-oxide nanoparticles. *Journal of magnetism and magnetic materials*. **320**, 1631–1638 (2008).

[74] Zeng, H.; Li, J.; Wang, Z. L.; Sun, S. Bimagnetic core shell FePt/Fe_3O_4 nanoparticles. *Nano letters* **4**, 187–190 (2004).

[75] Hong, J. H.; Kim, W. S.; Lee, J. I.; Hur, H. H. Exchange-coupled magnetic nanocomposites of $Sm(Co_{1-x}Fe_x)_5/Fe_3O_4$ with core-shell structure. *Solid state communications* **141**, 541–544 (2007).

[76] Peng, S.; Xie, J.; Sun, S. Synthesis of Co/MFe_2O_4 (M= Fe, Mn) core/shell particles. *Journal of solid state chemistry* **181**, 1560–1564 (2008).

[77] Monodisperse Fe_3O_4/Fe@SiO_2 core/shell nanoparticles with enhanced magnetic property. *Colloids and surfaces A: Physicochemical and engineering aspect* **293** 278–285 (2007).

[78] Zhang, H.; Lim, H.; Wei, J.; Wong, C. Size and shape evolution of magnetite nanocrystals in water-soluble systems. *Nanoscience and Nanotechnology letters* **3**, 155–160 (2011).

[79] Flyn, C. M. Hydrolysis of inorganic iron(III) salts. *Chemical review* **84**, 31–41 (1984).

[80] Sugimoto, T.; Matijević, E. Fromation of unifrm spherical magnetite particles by crystallization from ferrous hydroxide gels. *Journal of colloid and interface science* **74**, 227–243 (1982).

[81] Jolivet, J. P.; Chaneac, C.; Tronc, E. Iron oxide chemistry. From molecular clusters to extend solid networks. *Chemical Communication* **20**, 481–487 (2004).

[82] Jolivet, J. P.; Tronc, E.; Chaneac, C.Iron oxide: From molecular clusters to solid. A nice example of chemical versatility. *C. G. Geoscience* **338**, 488–497 (2006).

[83] Liu, X. Y. Generic progressive heterogeneous process in nucleation in nucleation. *Langmuir* **16**, 7337–7345 (2000).

[84] Kralj, S.; Drofenik, M.; Makovec, D. Controlled surface functionalization of silica-coated magnetic nanoparticles with terminal amino and carboxyl groups. *Journal of Nanoparticle Research* **13**, 2829 (2011).

[85] Kralj, S.; Makovec, D.; Čampelj, S.; Drofenik, M. Producing ultra-thin silica coatings on iron-oxide nanoparticles to improve their surface reactivity. *Journal of Magnetism and Magnetic Materials* **322**, 1847 (2010).

[86] Čampelj, S.; Makovec, D.; Drofenik, M. Functionalization of magnetic nanoparticles with 3-aminopropyl silane. *Journal of Magnetism and Magnetic Materials* **321**, 1346 (2009).

[87] Caruso, F. et al. Magnetic nanocomposites particles and hollow spheres constructed by sequential layering approach. *Chemistry of materials* **13**, 109–116 (2001).

[88] Kawashita, M. et al. Enzymatic preparation of hollow magnetite microspheres for hyperthermic treatment of cancer. *Journal of Materials Science: Materials in Medicine* **17**, 605–610 (2006).

[89] Tada, M.; et al. Synthesis of hollow ferrite nanospheres for biomedical applications. *Journal of Magnetism and Magnetic Materials* **321**, 1414–1416 (2009)

[90] Caruso, F. Hollow capsule processing through colloidal templating and self assembly. *Chemistry- a European journal* **3**, 413–419 (2000).

[91] Khurshid, H.; Li, W.; Tzitzos, V.; Hadjipanayis, C. G. Chemical synthesis of hollow nanostructures in iron oxides. *Nanotechnology* **22**, 265605 (2011).

[92] Kim, J. et al. Generalzed Fabrication of multifunctional nanoparticles on silica spheres.

Angewante chemie international edition **45**, 4789–4793 (2006).

[93] Tronc, E.; Belleville, P.; Jolivet, J. P.; Livage, J. Transforamtion of ferric hydroxide into spinel by Fe(II) absorption. *Langmuir* **8**, 131–139 (1922).

[94] Lisjak, D.; Ovtar, S.; Drofenik, M. The stability of $BaFe_{12}O_{19}$ nanoparticles in polar solvents. *Journal of Materials Science* **46**, 2851–2859 (2011).

[95] Pollert, E. et all. Search of new core materials for magnetic fluid hyperthermia: preliminary chemical and physical issues. *Progress in slid state chemistry* **37**, 1–14 (2009).

[96] Veverka, P.; Pollert, E.;v Závêta, K.; Vasseur, S.; Duguet, E. Sr-hexaferrite/maghemite composite nanoparticles-possible new mediators for magnetic hyperthermia. *Nanotehnology* **19**, 215705 (2008).

[97] Bodnarchuk, M, I. et all. Exchange-coupled bimagnetic Wustite/Metal ferrite core/shell nanocrystals: Size, Shape and Compostional control. *Small* **5**, 2247–2252 (2009).

[98] Zeng, H.; Li, J.; Liu, P. J.; Wang, Z. L.; Sun, S. Exchange-coupled nanocomposite magnets by nanoparticle self-assembly. *Letters to Nature* **420***,* 395–398 (2002).

[99] Fullerton, E.; Jiang, J. S.; Badet, S. D. Hard/soft heterostructures: model exchange-spring magnets. *Journal of magnetism and magnetic materials* **200**, 392–404 (1999).

[100] Sellmyer, D. J. Strong magnets by self-assebmly. *Applied physics* **420**, 374–375 (2002).

[101] Hadjipanayis, C. G. Nanophase hard magnets. *Journal of magnetism and magnetic materials* **200**, 373–391 (1999).

[102] Patel, V.; El-Hilot, M.; O'Grady, K.; Chantrell, R. W. Nucleation fields in an exchange-spring hard magnet. *Journal of physics D: Applied Physics* **26**, 1453–1458 (1993).

[103] Kneller, E. F. The exchange-spring magnets: A new material principle for permanent magnets. *IEEE Transaction on magnetics* **27**, 3588–3600 (1991).

Index of Figures

Figure 1: *The response of diamagnetic (a) and paramagnetic (b) materials when exposed to the external magnetic field [3].* 18
Figure 2: *Schematic illustration of the ferromagnetic (a) and antiferromagnetic ordering (b) [2].* 18
Figure 3: *Schematic illustration of the ferrimagnetic spin orientation [1].* 19
Figure 4: *Schematic illustration of the hysteresis loop for the magnetic materials with multi-domain structure [5].* 20
Figure 5: *Schematic illustration of the hysteresis loop typical of hard and soft magnetic materials [3].* 21
Figure 6: *Magnetic behaviour derived from the scale reduction of the magnetic nanoparticles [6].* 22
Figure 7: *Axis system defined for uniaxial nanoparticles [1].* 23
Figure 8: *The MH curve of superparamagnetic nanoparticles.* 24
Figure 9: *The coercivity in dependence of the particles size [1].* 25
Figure 10: *Crystal structure of Ba hexaferrite* 26
Figure 11: *Cross section view of Ba hexaferrite structure [7].* 27
Figure 12: *Structure of cubic ferrite [1].* 28
Figure 13: *Concentration of soluble precursors of solid phase during precipitation [18].* 31
Figure 14: *Schematic illustration of the structure of the electric double layer [25].* 34
Figure 15: *Interaction energy V_T as a function of distance between particles [25].* 35
Figure 16: *ATR-IR spectra of urea (a) and Fe^{3+}-urea complex (b).* 47
Figure 17: *UV-Vis In-situ measurements of Fe^{3-}-urea complex at increasing temperatures.* 48
Figure 18: *pH vs. time curves for samples M60-0 and M60-U.* 50
Figure 19: *TEM image of M60-U.* 51
Figure 20: *TEM image of iron-oxide particles M60-Mg, synthesized with the additions of $Mg(OH)_2$ into the Fe precursors solution at temperature of 60 °C.* 51
Figure 21: *pH vs. time curve for samples M60-Mg_0 and M60-Mg.* 53
Figure 22: *XRD pattern for sample M60-Mg, M60-Mg_0 and M60-Mg_{60}.* 53
Figure 23: *pH vs. time curve for samples M70-Mg_0 and M70-Mg_{10}.* 54
Figure 24: *pH vs. time curve for samples M50-Mg_0 and M50-Mg_{10}.* 55
Figure 25: *XRD pattern for sample M50-Mg_0 and M50-Mg_{10}.* 55
Figure 26: *(a) TEM image of dried suspension of SiO_2 nanoparticles revealing bimodal size distribution, and (b) ζ-potential measurements of the stable silica core nanoparticles' suspension (SiO_2) and the silica nanoparticles functionalized with hydrolyzed aminopropyl silane (APS-SiO_2).* 57

Figure 27: *TEM images of the Ba-hexaferrite core nanoparticles, with different size and morphology: (a) mixture of small discoid and larger platelet crystals with average size between 10-70 nm (BaM_{10-70}), (b) the platelet crystals of the size between 30-70 nm, (c) the Ba-hexaferrite discoid nanoparticles with diameter of 10 nm and thickness of approximately 3 nm (BaM_{10}), (d) HREM pattern of the discoid Ba-hexaferrite nanoparticle BaM_{10} oriented edge-on, (e) hexagonal platelet crystals with average diameter of ~ 100 nm and thickness of 5 nm (BaM_{100}) and (f) TEM image of Ba hexaferrite platelet crystal oriented edge-on with its large surfaces parallel to the electron beam.*.....59

Figure 29: *pH vs. time curve measured during the synthesis of S@SiO_2-10.* 61

Figure 30: *Representative TEM image of the product S@SiO2-10 (a), the HREM pattern of the spinel particles on the surfaces of the core silica nanoparticle (b), and the electron diffraction pattern recorded from a large area of the material (c).* 62

Figure 31: *Representative TEM image corresponding to Stage 1 of S@SiO_2-10 (a), TEM image the sample at higher magnification (b), the electron diffraction pattern recorded from the larger area of the material (left) is compared to the calculated patterns for 3 (right down) and 5 nm (right top) nanoparticles with structure of γ-FeOOH (c).*.....63

Figure 32: *Representative TEM image corresponding to Stage 2 of sample S@SiO_2-10 (a) TEM image of selected area revealing the increased particles size and improved crystalline order (b) and electron diffraction recorded over large area of material (left) and simulated electron diffraction for 5 nm orthorhombic γ-FeOOH phase (top) and cubic spinel phase (down).*.....64

Figure 33: *Representative TEM image of the sample S@APS-SiO_2 with corresponding electron diffraction (inset).*.....65

Figure 34: *pH vs. time curve for the sample S@SiO_2-0, S@SiO_2-10 and S@SiO_2-60 monitored during the course of reaction.* 67

Figure 35: *Representative TEM image corresponding to stage 2 of sample S@SiO_2-0 with the corresponding electron diffraction pattern.*.....68

Figure 36: *Representative TEM image of product corresponding to Stage 1 of sample S@SiO_2-60 (a) and corresponding electron diffraction pattern recorded over large area of the material (b).*.....69

Figure 37: *Representative TEM image of second intermediate product of sample S@SiO_2-60 (a), TEM image revealing heterogeneously nucleated spinel nanoparticles on the silica core surfaces (b) and corresponding electron diffraction recorded over large area of the material (c).* 70

Figure 38: *Representative TEM image of final product of sample S@SiO_2-60 (a), TEM image revealing heterogeneously nucleated spinel nanoparticles on the silica core surfaces (b) and corresponding electron diffraction pattern recorded over limited area of rood-like particles shown in (25a) (c).* 71

Figure 39: *Representative TEM image of S@BaM_{10-70} nanocomposite particles (a) and TEM image at increased magnification revealing edge-shaped nanocomposite particles (b).*.....73

Figure 40: *Nanocomposite particles of sample S@BaM, oriented edge-on; HF denotes hexaferrite and S denotes spinel.*.....74

Figure 41: *EDXS spectra of S@BaM_{10-70} nanocomposite particles (a) and BaM_{10-70} core nanoparticles (b).*.....75

Figure 42: *HREM pattern of one nanocomposite particle oriented with its large surface parallel to the electron beam.* 75
Figure 43: *Representative TEM image of the sample S@BaM$_{30-70}$ (a), TEM image revealing the S@BaM$_{30-70}$ nanocomposite particles of different thickness (b), and HREM image of the S@BaM$_{30-70}$ nanocomposite particle revealing the epitaxial growth of spinel phase on the hexaferrite core (c).* 77
Figure 44: *TEM image of large hexagonal platelet crystal laying flat on specimen support, revealing the formation of layer of additional material on its surface.* 78
Figure 45: *TEM image of large hexagonal platelet crystal oriented with is large surface parallel with the electron beam.* 79
Figure 46: *HREM pattern of nanocomposite particles of sample S@BaM$_{100}$, oriented with is large surface parallel with the electron beam (a) and corresponding electron diffraction revealing the superimpositions of reflection cubic spinel and hexagonal structure (b).* 80
Figure 47: *TEM image of sample S@BaM$_{100}$, revealing hexaferrite platelet crystal lying with its large surface perpendicular to the electron beam.* 81
Figure 48: *Representative TEM image of S@BaM$_{10}$ nanocomposite particles.* 82
Figure 49: *HREM image of the S@BaM$_{10}$ particles (inset Fast Furrier Transform).* 82
Figure 50: *Magnetic hysteresis of S@BaM$_{10-70}$ nanocomposite particle in comparison to BaM$_{10-70}$ core nanoparticles.* 83
Figure 51: *Magnetic hysteresis of S@BaM$_{10}$ nanocomposite particle in comparison to BaM$_{10}$ core nanoparticles.* 84
Figure 52: *Magnetic hysteresis of S@BaM$_{100}$ nanocomposite particle in comparison to BaM$_{100}$ core nanoparticles.* 85
Figure 53: *Magnetic hysteresis of BaM$_{100}$ core nanoparticle, superparamagnetic spinel nanoparticles and their homogeneous mixture BaM-S$_{MIX}$.* 85
Figure 54: *Magnetic hysteresis of magnetically-oriented BaM$_{100}$ core nanoparticles (a), and magnetically-oriented S@BaM$_{100}$ nanocomposite particles (b).* 86
Figure 55: *In-plane magnetic hysteresis of oriented BaM$_{100}$ core nanoparticles compared to in-plane oriented S@BaM$_{100}$ nanocomposite particles.* 86
Figure 56: *B(H) loop for the sample BaM$_{100}$. The shaded area indicates the corresponding energy product $|BH|_{MAX}$.* 87
Figure 57: *B(H) loop for the sample S@BaM$_{100}$. The shaded area indicates the corresponding energy product $|BH|_{MAX}$.* 87
Figure 58: *The schematic of the spinel coating formation.* 95
Figure 59: *Schematic of spinel in <111> zone and hexaferrite in <0001> zone.* 97
Figure 60: *Schematic of spinel in <110> zone and hexaferrite in <11-20> zone.* 97

Index of Tables

Table 1: *List of products synthesized using different precipitating agent.* 49
Table 2: *List of products synthesized at different temperatures.* 52
Table 3: *List of SiO_2 and BaM core nanoparticles with their properties.* 58
Table 4: *List of reaction conditions used for synthesis of spinel in the suspension of silica core nanoparticles (SiO_2 or APS-SiO_2) and the results of product analyses.* 66
Table 5: *List of S@BaM products and the results of products analysis.* 77

Appendix

Original scientific article

1. MAKOVEC, D.; PRIMC, D.; ŠTURM, S.; KODRE, A.; HANŽEL, D.; DROFENIK, M. Structural properties of ultrafine Ba-hexaferrite nanoparticles. *Journal of solid state chemistry* **196**, 63–71 (2012).

2. PRIMC, D.; DROFENIK, M.; MAKOVEC, D. Low-temperature hydrothermal synthesis of ultrafine strontium hexaferrite nanoparticles. *European Journal of Inorganic Chemistry* **2011**, 3802–3809 (2011).

3. PRIMC, D.; MAKOVEC, D.; LISJAK, D.; DROFENIK, M. Hydrothermal synthesis of ultrafine barium hexaferrite nanoparticles and the preparation of their stable suspensions. *Nanotechnology (Bristol)* **20,** 315605 (2009).

4. MRAKOVIČ, A.; BLAGUŠA, J.; PRIMC, D.; JAGLIČIĆ, Z.; KUSIGERSKI, V.; SPASOJEVIĆ, V.; Modified-self propagating high-temperature synthesis of nanosized $La_{0.7}Ca_{0.3}MnO_3$. *Ceramics International*, DOI:doi.org/10.1016/j.ceramint.2012.10.21

Published scientific conference contributions

5. MAKOVEC, D.; PRIMC, D.; ŠTURM, S.; KODRE, A.; DROFENIK, M. Synthesis and structural properties of ultrafine barium-hexaferrite nanoparticles. V: *First Euro-Mediterranean Meeting on Functionalized Materials. Program and abstracts*. 51 (EMMFM, Sousse, Tunisia, 2011).

6. PRIMC, D.; DROFENIK, M.; LISJAK, D.; MAKOVEC, D. Magnetne lastnosti nanodelcev Ba heksaferita ($BaFe_{12}O_{19}$) sintetiziranih s hidrotermalno sintezo. V: PETELIN, D. (ur.); TAVČAR, A. (ur.); ROŽIČ, B. (ur.); POGORELC, B. (ur.). *3. študentska konferenca Mednarodne podiplomske šole Jožefa Stefana. Zbornik prispevkov*. 190–195 (MPŠ, Ljubljana, 2011).

7. PRIMC, D.; MAKOVEC, D.; LISJAK, D.; DROFENIK, M. Priprava magnetnih tekočin iz superparamagnetnih delcev barijevega heksaferita. V: GLAVIČ, P. (ur.); BRODNJAK - VONČINA, D. (ur.). *Slovenski kemijski dnevi 2008. Zbornik referatov.* 9 (Univerza v Mariboru, Fakulteta za kemijo in kemijsko tehnologijo, Maribor, 2008).

Published scientific conference contribution abstract

8. PRIMC, D.; DROFENIK, M.; MAKOVEC, D. Synthesis and properties of hexaferrite-spinel nanocomposite particles. V: ŽAGAR, K. (ur.); LENART, A. (ur.); PEČKO, D. (ur.); 6th Young Researchers' Day 2012. *Program and abstract book*. 5 (Jožef Stefan Institute, Department of Nanostructured Materials, Ljubljana, 2012).

9. PRIMC, D.; DROFENIK, M.; MAKOVEC, D. Multifunctional nanocomposites of spinel (γ-Fe_2O_3) and hexagonal (SrFe12O19) ferrites. V: International Symposium on Advanced Complex Inorganic Nanomaterials. *ACIN 2011 - evolution and revolution : book of abstracts.* 150 (Namur: Presses Universitaires de Namur, Namur, 2011).

10. PRIMC, D.; DROFENIK, M.; MAKOVEC, D. Structural analysis of nanocomposite hexaferrite-spinel particles using high resolution electron microscopy (HREM). V: SLONANO 2011. *Book of abstracts*. 69 (SLONANO 2011, Ljubljana, 2011).

11. PRIMC, D.; DROFENIK, M.; MAKOVEC, D. Nanocomposite of spinel (γ-Fe_2O_3) and hexagonal

($SrFe_{12}O_{19}$) ferrites. V: GODEC, M. (ur.); 19. konferenca o materialih in tehnologijah. *Program in knjiga povzetkov*. 77 (Inštitut za kovinske materiale in tehnologije, Portorož, 2011).

12. PRIMC, D.; DROFENIK, M.; MAKOVEC, D. Priprava nanokompozitov na osnovi heksagonalnih ($SrFe_{12}O_{19}$) in spinelnih (γ-Fe_2O_3) feritov. V: PRIBOŠIČ, I. (ur.); KRNEL, K. (ur.); 5. dan mladih raziskovalcev. *Program in povzetki*. (Institut "Jožef Stefan", Ljubljana 2011).

13. MAKOVEC, D.; PRIMC, D.; ŠTURM, S.; KODRE, A.; DROFENIK, M. Strukturne lastnosti zelo majhnih nanodelcev barijevega heksaferita V: KRAVANJA, Z (ur.); BRODNJAK-VONČINA, D. (ur.); BOGATAJ, M. (ur.); Slovenski kemijski dnevi 2011. *Zbornik povzetkov referatov s posvetovanja.* 8 (FKKT Maribor, Portorož, 2011).

14. PRIMC, D.; DROFENIK, M.; MAKOVEC, D. Synthesis and characterization of $SrFe_{12}O_{19}$/ γ-Fe_2O_3. V: NANO 2010, Xth International Conference on Nanostructured Materials. *Abstract book.* 191 (NANO 2010, Rim, Italija, 2010).

15. PRIMC, D.; DROFENIK, M.; MAKOVEC, D. Core-shell nanocomposites of hexagonal ($SrFe_{12}O_{19}$) and spinel (γ-Fe_2O_3) ferrite nanoparticles. V: MIHAILOVIĆ, D. (ur.); HOČEVAR, S. (ur.); ARČON, D. (ur.); KUNEJ, Š (ur.); UMEK, P. (ur.); KNAVS, M. (ur.). SLONANO 2010. *Book of abstracts.* 38 (National Institute of Chemistry, Ljubljana, 2010).

16. PRIMC, D.; MAKOVEC, D.; DROFENIK, M. Hidrotermalna sinteza nanodelcev kompleksnih heksagonalnih feritov ($BaFe_{12}O_{19}$, $SrFe_{12}O_{19}$) in priprava njihovih stabilnih suspenzij. V: KUŠČER, D. (ur.); PERC, B. (ur.). 4. Dan Mladih Raziskovalcev KMBO, *Program in povzetki* 49 (Institut "Jožef Stefan", Ljubljana, 2010).

17. PRIMC, D.; MAKOVEC, D.; DROFENIK, M. Hydrothermal synthesis of ultrafine particles of hexagonal ferrites ($BaFe_{12}O_{19}$, $SrFe_{12}O_{19}$) and the preparation of theirs stable suspensions. V: BENČAN, A. (ur.); KUŠČER, D. (ur.); MALIČ, B. (ur.); KOSEC, M. (ur.). Workshop on structural characterisation. *Program and abstract book.* 24 (Institut »Jožef Stefan«, Electronic Ceramic Department, Ljubljana, 2010).

18. PRIMC, D.; MAKOVEC, D.; DROFENIK, M. Priprava stabilnih suspenzij nanodelcev Sr-heksaferita sintetiziranih s hidrotermalno sintezo. V: GLAVIČ, P. (ur.); BRODNJAK - VONČINA, D. (ur.). Slovenski kemijski dnevi 2010. *Zbornik povzetkov referatov s posvetovanja*, 44 (Maribor: FKKT, Maribor, 2010).

19. PRIMC, D.; MAKOVEC, D.; DROFENIK, M. Hydrothermal synthesis of ultrafine particles of hexagonal ferrites ($BaFe_{12}O_{19}$, $SrFe_{12}O_{19}$) and the preparation of their stable suspensions. V: ECIS 2009, 23rd Conference of the European Colloidal and Interface Society. *Abstracts* (European Colloid and Interface Society, Antalya, Turkey, 2009).

20. PRIMC, D.; LISJAK, D.; MAKOVEC, D.; DROFENIK, M. Priprava magnetnih tekočin iz superparamagnetnih delcev barijevega heksaferita. V: ISKRA, J. (ur.); MILOŠEV, I. (ur.); *Dan mladih raziskovalcev 2009*. (Institut "Jožef Stefan", Ljubljana, 2009).

21. PRIMC, D.; SAJKO, M.; VERHOVŠEK, D.; DROFENIK, M.; MAKOVEC, D. Hidrotermalna sinteza anatasnih fotokatalitskih nanodelcev. V: VALANT, M. (ur.); PIRNAT, U. (ur.); Slovenska konferenca o materialih in tehnologijah za trajnostni razvoj. *Knjiga povzetkov. Zbornik*. (Založba Univerze, Nova Gorica, 2009).

22. PRIMC, D. Hydrothermal synthesis of photocatalytic anatase nanoparticles. V: ŠETINA, B. (ur.); JUNKAR, I. (ur.); KALUŽA, B. (ur.); ELERŠIČ, K. (ur.). 1. študentska konferenca Mednarodne podiplomske šole Jožefa Stefana. *Zbornik prispevkov*. 40 (Mednarodna podiplomska šola Jožefa Stefana, Ljubljana, 2009).

Work report

23. MAKOVEC, D.; GYERGYEK, S.; PRIMC, D.; ANŽELAK, B.; PUŠNIK, K. *Vpliv sinteznih parametrov na velikost nanodelcev : sinteza večjih količin nanodelcev* (IJS delovno poročilo 10914, Ljubljana, 2012).

24. MAKOVEC, D.; GYERGYEK, S.; PRIMC, D.; ANŽELAK, B. *Vpliv sinteznih parametrov na velikost nanodelcev.* (IJS delovno poročilo 10913, Ljubljana, 2012).

25. MAKOVEC, D.; KRALJ, S.; PRIMC, D.; ANŽELAK, B. *Analize suspenzij nanodelcev* (IJS delovno poročilo 10863, Ljubljana, 2011).

26. ŽIGON, S.; MAKOVEC, D.; GYERGYEK, S.; ANŽELAK, B.; PRIMC, D.; ČAMPELJ, S.; SELINŠEK, A.; VERHOVŠEK, D. *Razvoj fotokatalitskih superparamagnetnih nanokompozitov za postopke zmanjševanja emisij škodljivih snovi v okolje* (IJS delovno poročilo 10672, zaupno, Ljubljana, 2011).

27. MAKOVEC, D.; PRIMC, D.; ČAMPELJ, S.; VERHOVŠEK, D.. *Analiza nanodelcev TiO_2 tujih proizvajalcev : 2. fazno poročilo* (IJS delovno poročilo 10033, Ljubljana, 2008).

28. MAKOVEC, D.; PRIMC, D.; ČAMPELJ, S.; VERHOVŠEK, D.; SAJKO, M. *Hidrotermalna sinteza fotokatalitskih nanodelcev : 2. fazno poročilo* (IJS delovno poročilo 10034, Ljubljana, 2008).

29. MAKOVEC, D.; DROFENIK, M.; LISJAK, D.; PRIMC, D.; GYERGYEK, S. *Hidrotermalni razkroj barijevega heksaferita* (IJS delovno poročilo 9853, Ljubljana, 2008).

30. LISJAK, D.; PRIMC, D. *IMICIMO WP1 report* (IJS delovno poročilo 9897, Ljubljana, 2008).